Unique spatiotemporal synchronization solutions of heterogeneous local Ca^{2+} dynamics underlie the formation of each impulse that emerges from the cardiac sinoatrial node

Syevda Tagirova, Alexander V. Maltsev, Georgiana L. Baca, Rostislav Bychkov, Victor A. Maltsev, Edward G. Lakatta.

Laboratory of Cardiovascular Science, Intramural Research Program, National Institute on Aging, National Institute of Health, Baltimore, MD.

**Correspondence: Edward G. Lakatta (lakattae@grc.nia.nih.gov)*

Abstract

Spontaneous, stochastic, local Ca^{2+} oscillations (LCOs) that are heterogeneous in phase, frequency, and amplitude incessantly occur throughout the neuronal-like cytoarchitecture of the heart's pacemaker, the sinoatrial node (SAN). How information encoded within ensembles of these heterogeneous LCOs is linked to the incessant emergence of the formation of rhythmic SAN impulses, however, is an unsolved problem. We applied a wide range of analytical techniques adapted from dynamical systems and neuroscience to map fine details of spatiotemporal distributions of local Ca^{2+} dynamics in time-series of high-speed acquisition panoramic images of mouse SANs *ex vivo.* Phase analysis delineated a network of functional pacemaker cell clusters, in which Ca^{2+} dynamic amplitudes, kinetics, and phases were similar, but still differed from each other, and differed from those of other clusters. Local Ca^{2+} dynamics within the network of clusters formed rhythmic global Ca^{2+} impulses, with a mean rate identical to that recorded by the reference sharp electrode in the right atria. Initial conditions of each impulse initiation differed from each other, due mostly to stochastic nature of Ca^{2+} dynamics within a small cluster located near the crista terminalis, having the highest intrinsic power, earliest rotor-like energy transfer, most frequent point-to-point instability, earliest acrophase, and greatest impulse-to-impulse variability within the network of functional clusters. A spontaneous, slowly increasing ensemble Ca^{2+} signal within this cluster forms a foot of each CaT. Following this foot, the amplitude of the global CaT increased rapidly, due to rapid increases in the kinetics and amplitudes of Ca^{2+} dynamics in some adjacent clusters. In other clusters near to the inter-atrial septum, a delayed, but rapid increase in the Ca^{2+} dynamic occurred when the relaxation phase of the CaT had already begun.

Orbit plots and Lyapunov exponent analyses detected both deterministic and stochastic features within the SAN Ca2+ dynamics. Correlation analyses detected cross-talk among the Ca^{2+} dynamics within *different clusters* that varied, not only throughout an impulse, but also from one impulse to the next, forming unique dynamic small-world networks, assessed as ratios of the highest correlation coefficients and shortest path lengths, ultimately creating *a unique* spatiotemporal Ca^{2+} dynamic synchronization solution for each CaT. Thus, the emergence of each CaT from individual LCOs during each cycle is unique underlies cycle length variability in SAN, recapitulating the emergence of spontaneous CaTs in isolated, single, SAN pacemaker cells.

Keywords: calcium dynamics; calcium transient; calcium kinetics; cross-talk; local calcium oscillations; Lyapunov exponent; network of functional clusters; pacemaker function; small world signaling; sinoatrial node.

1. Introduction

Incessant, stochastic, oscillatory calcium (Ca^{2+}) signals underlie important biologic processes throughout nature, and it has been argued that oscillatory frequency-dependent amplitude control provides a precise, noise-resistant control strategy that allows functional Ca^{2+} biologic signals that are of graded amplitude to be stable [1, 2]. For example, self-organization of local Ca2+ dynamics in the brainstem are implicated in initiation of signals that regulate rhythmic automatic breathing [3], and in melanocytes initiation of skin protective signals [4]. Rhythmic Ca^{2+} dynamics initiate the first heartbeat [5]. Emergence of spiking regimes in the early heartbeat are driven by a noisy phase transition in which gradual and largely asynchronous development of Ca2+-dependent single-cell bioelectrical properties produce a stereotyped and robust tissue-scale transition from quiescence to coordinated beating [6]. In cells isolated from the adult heart's pacemaker, the sinoatrial node (SAN), frequency-dependent amplitude control of spontaneous ensemble Ca^{2+} signals formed by spontaneous local Ca^{2+} releases (oscillations) allows for rapid, graded control of the action potential (AP) firing rate [7-14]. Pacemaker cells embedded in SAN tissue, incessantly generate spontaneous, partially stochastic, [15] local Ca^{2+} oscillations (LCO) that are heterogeneous in phase, frequency and amplitude throughout the SAN (see Movie S1) [16]. A novel approach (chronopix analysis) to detect phase heterogeneity of Ca^{2+} signaling within image pixels demonstrated that, in antithesis to a concentric, continuous spread of impulse formation, [17-19] the spread of Ca^{2+} signals is discontinuous throughout the SAN.

The quintessential research frontier in SAN impulse formation is to understand how information encoded within local Ca^{2+} oscillations (LCOs) that are heterogeneous within and among pacemaker cells across SAN tissue is translated into formation of rhythmic SAN impulses that initiate rhythmic impulses that emerge within the SAN to initiate heartbeats [7, 16, 20]. Studies using confocal 3D tile imaging coupled to intracellular Ca^{2+} measurements have detailed novel cytoarchitecture of the network of nerves, glial and interstitial cells and pacemaker cells within the SAN [16, 20]. It has been suggested that SAN cytoarchitecture harboring Ca^{2+} oscillations resembles neuronal tissue [7, 16, 20]. In neuronal tissue the LCO information sharing underpins neural communication and plasticity, from modulation of neurotransmitter release to the activation of gene transcription essential for long-

term potentiation and memory formation [1]. It is known that the role of microdomains within neurons, where Ca^{2+} concentrations can rapidly oscillate, underscore the precision with which Ca^{2+} signaling must be regulated to affect neuronal function accurately [1, 21-23].

The discovery of small-world network topology in the brain provided insights into neural organization. These networks are characterized by high local clustering coefficients (similar to regular lattices) while maintaining short average path lengths (similar to random networks) through the presence of select long-range connections. This architecture allows for both segregated and integrated information processing [24, 25].

Inspired by previous studies of how spontaneous local Ca^{2+} dynamics participate in the formation of APs in single SAN cells [7-14], and the idea that synchronization of incessant heterogeneous Ca^{2+} oscillations is a universal signaling mechanism at multiple scales [2, 26], we applied, for the first time in ex vivo SAN tissue, a wide range of analyses adapted from dynamical systems and neurosciences, aiming to elucidate the mechanisms of emergence of rhythmic global SAN tissue Ca^{2+} impulses from incessant stochastic, heterogenous LCOs in pacemaker cells.

2. Materials and Methods

2.1. Sinoatrial node tissue (SAN) preparation

Our experiments conformed to the Guide for the Care and Use of Laboratory Animals, published by the US National Institutes of Health. The experimental protocols were approved by the Animal Care and Use Committee of the National Institutes of Health (protocol # 457-LCS-2027). See details in supplementary materials.

2.2. Data acquisition of local Ca2+ signals/oscillations (LCO) during impulse formation in SAN ex vivo

The SAN preparation (n=4) was incubated with Calbryte 520 AM (25 μM) a fluorescent calcium indicator, for 1.5 hours at room temperature. See detailed methods in supplementary materials.

2.3. Atrial cell action potential recording

Because action potential (AP) characteristics differ in the SAN pacemaker cells among regions of the SAN [16], to deduce the timing of SAN action potential (AP), we placed the reference electrode in the atria near the crista terminalis (CT). See detailed methods in supplementary materials.

2.4. Data analysis

In the present study, we used multiple software programs to apply a diverse set of linear and non-linear analytical analyses of local Ca^{2+} (LCO) dynamics. Additional details can be found in the supplementary materials.

3. Results

3.1. Regional clusters of pacemaker cells that differ in Ca^{2+} dynamics form integrated (global) SAN Ca^{2+} impulses (Ca^{2+} Transients, CaT)

Previous high-resolution SAN Ca^{2+} imaging studies have revealed incessant, stochastic, and heterogeneous local Ca^{2+} oscillations (LCOs) within pacemaker cells (see Movie S1). To investigate how information encoded in these LCOs integrates into global SAN Ca^{2+} transients (CaTs), we performed high-speed time-series imaging of Ca^{2+} signals in ex vivo mouse SAN tissue (n=4). Using a high-speed acquisition camera, we mapped the spatiotemporal distribution of LCOs across the entire SAN. Despite variability in fine details of Ca^{2+} dynamics across individual SANs, all tissues exhibited a consistent overarching pattern, as exemplified in Fig. 1A. Spontaneous, rhythmic, and repetitive global SAN Ca^{2+} impulses, or CaTs, emerged during these recordings (Fig. 1A, black trace). The mean peak to peak interval of the global CaT (200.36±21.75ms, n=4) was identical to the mean peak to peak AP interval (200.37±21.79ms, n=4), recorded by a sharp intracellular microelectrode in the right atrium, indicating that the frequency of the global CaTs was the same as frequency of electrical impulses that emerged from the SAN to activate the atrium.

We assessed Ca2+ information flow during and between the formation of these SAN global impulses. Characteristic functions (amplitude and phase) of LCOs were extracted every 1.7ms from 50 regions of interest (ROIs) that encompassed the entire SAN area during time-series recordings (see Fig. 1B). Figure 1, Panel C illustrates the spatial distribution of acrophases, which indicate the times when the maximum amplitudes of the Ca2+ dynamics within each ROI from Panel B were reached during impulses. Note that spatial distributions of ROIs within the SAN formed distinct clusters that exhibited similar Ca2+ dynamics. Acrophases of *individual* ROI LCOs (Fig. 1B), color-coded in Fig.1C throughout the SAN, differed by up to 34 ms. Note that the variability of ROIs acrophases varied among different clusters. The red color-coded cluster near the crista terminalis (CT), shown in panel C, exhibited the highest variability in ROI acrophases. In contrast, the adjacent yellow color-coded cluster showed the least variability (see panel D). Panel E and Movie 2 illustrate the 3D relationships between normalized LCO amplitudes and time within each ROI cluster at every 1.7 ms during the initial 180 ms of the time-series recording. In addition,

clearly illustrating differences in acrophases of the peak amplitudes of the ROIs comprising each color-codded cluster, panel E also shows that even prior to noticeable acceleration of the kinetics of Ca2+ dynamics within a cluster, Ca2+ oscillations that achieve about 20 % of maximum amplitude are visible in the red and blue clusters but not in yellow and/or green clusters.

Because previous studies in single isolated SAN pacemaker cells demonstrated that self-ordering of local Ca2+ oscillations (LCO) forms the foot of the AP-induced CaT [27, 28], we searched for the presence of a foot in the global CaTs within SAN tissue. Figure 2A illustrates a detailed kinetic analysis of the integrated (global) SAN CaTs, generated by the integral of all LCOs in all ROIs over a time span of 350ms for two global CaTs.

The amplitude of the two successive integrated (global) CaT and each of its first three derivatives are shown in panel Ai-iv respectively. The global Ca2+ signal began to *steadily increase* from baseline levels (background noise) at ~50ms (panel B) and continued to increase slowly until the time at which 3d derivative of CaT reached its peak (at ~65ms) that was marked by an inflection point in the global CaT trace illustrated in panel C. Beyond this inflection point, the global CaT rapidly increased, reaching a peak about 20ms later. Thus, in the SAN tissue, the global CaT exhibits a clear slow foot that lasts about 15 ms and contributes approximately 4.02% to the CaT peak amplitude.

Next, we related the kinetics of the global CaT to the kinetics of the average LCO Ca^{2+} dynamics of each color-coded cluster, which were determined by averaging the Ca2+ dynamics of ROIs within each color-coded cluster. Figure 3A shows an example of the global CaT and its derivatives (a black trace in both the upper and lower panels) overlaid on the average LCO Ca^{2+} dynamics from the four distinct color-coded clusters, including their respective derivatives.

Panel B shows the normalized amplitudes of the average LCO Ca^{2+} dynamics depicted in panel A (top), along with their derivatives. The ensemble Ca2+ signal of the red cluster was the first to increase not only in this impulse but across all 19 impulses that emerged within the time-series. The time at which the Ca^{2+} signal of the red cluster began to accelerate (as indicated by the initiation of its second derivatives in the lower panel) at ~45-50 ms following the onset of the recording and corresponding approximately to the time of initiation of the foot of the global CaT (Fig. 2B-C). The maximum velocity of this signal occurs at about 63 ms, which aligns with the foot of the global CaT, as depicted in Figure 2B, C.

Although the contribution of the red cluster dominated the foot of the global SAN CaT, it is important to note that the Ca^{2+} dynamic in other clusters also began to increase during the foot, but at a later time than the Ca^{2+} dynamic of the red cluster (panel B).

The maximum velocity of the normalized amplitude of the Ca^{2+} signal of the red (4.6 a.u. at 63ms) cluster was slower compared to that of the yellow (6.6 a.u. at 72ms), green (6.5 a.u. at 77ms) and blue (5.7 a.u. at 91ms) clusters respectively (panel B).

The growth of the instantaneous rate of change (IROC) in the red color-coded cluster occurred earlier and was greater compared to the three other clusters and the global CaT during the impulse initiation phase (from approximately 15 to 65 ms, covering the pre-foot and foot stages) (Panel C). During this period, the other clusters either exhibited minimal changes or remained unchanged (see Panel C, highlighted red areas above zero). At the time of maximum velocity in the red cluster, the Ca^{2+} dynamic and its IROC in the yellow cluster began to rise rapidly, closely followed by a similar increase in the Ca^{2+} dynamic in the green cluster (panel A-B-C). Simultaneously, there was a gradual increase in the Ca^{2+} dynamics within the blue clustered ROIs (between ~61-71 ms of impulse formation) followed by a plateau of about 5 milliseconds, following which the blue cluster accelerated rapidly. The average peak amplitude of the Ca2+ signal in the blue color-coded cluster was intermediate between those of the red, yellow, and green color-coded clusters (panel A).

The analyses in Figs. 1C-D and 3A-B focused on relationships of the Ca^{2+} dynamics of the four color-coded clusters during a single impulse. To determine the contributions of the Ca2+ dynamics of the regional clusters to the Ca2+ dynamics of the global CaT that emerged within the entire time-series Fig. 1A, we performed principal component analysis (PCA) of the entire 19 impulses. An example of PCA analyses during the first impulse is shown in Fig. 4A-D, and PCA of all 19 impulses of four color-coded areas are shown in Fig. S1. The first two principal components (PC) accounted for ~ 85-93% of the total variance within the time-series of 19 impulses during the impulse initiation (ignition), ~81-90% during the fast phase, and ~52-73% during the decay phase (Fig. S1).

During an impulse initiation (ignition, marked as 1 in panels A and D), PC1 of the red cluster accounted for over 90% of the variations observed in the Ca2+ dynamics, and during this time, PC2 contributed approximately 8% to these changes, predominantly attributed to the yellow cluster. In the subsequent rapid phase (designated as 2 in panels B and D), PC1 of both the red and yellow clusters collectively contributed around 84% to the alterations in Ca2+ dynamics, while the

green cluster was responsible for the majority of changes observed in PC2 (13%). During the decay phase (at ~85-150 ms marked as 3 in panels C and D) of the impulse, PC1 of the blue clusters contributed approximately 64% of the changes in Ca2+ dynamics, with PC2 contributing 32%, where the green cluster exhibited the largest contribution to this component. It is important to note, however, that during any given time window, Ca^{2+} dynamics across all functional clusters collectively influence the overall dynamics of the global SAN CaT (Figs. 4, S1).

We then analyzed the divergence of Ca^{2+} dynamic kinetics in each color-coded cluster around fixed points (as described in the methods) to determine the stability behavior of the network of functional color-coded clusters within the SAN during impulse initiation. Figure 5 illustrates the normalized amplitudes of SAN Ca^{2+} impulses (panel A) and 1st derivatives (velocities, panel B) of four color-coded SAN clusters superimposed on SAN global CaT during the first 300 ms of time-series recordings (during which two global CaT emerged). Panels B and C show that the Ca^{2+} dynamic within each color-coded spatial domain consistently transitioned between stable (closed circles) and unstable states (open circles). Following a prior impulse, the Ca^{2+} dynamic of all four clusters reached the stable fixed points (within approximately 40 ms), before the Ca^{2+} dynamic of the red cluster diverged (after 5 ms toward an unstable point, as its velocity steadily increased during impulse formation~45-63 milliseconds of the recording.

The timing of this unstable fixed point in the red cluster aligned with the onset point of the foot of the 1st global CaT, which occurred at 50 ms (arrow in panel A, see also global CaT foot in Figs. 2, 3). The yellow, green, and blue curves transitioned toward the unstable fixed points at ~55, 60, and 58 ms, respectively. Following the transition, the four SAN Ca^{2+} spatial domains (red, yellow, green, and blue) all reached the next 'quasi-stable fixed point'(at the time of a maximum of 1st derivative, and not discussed in this study), returning to the stable state at ~77, 83, 87ms red, yellow and green clusters, respectively, but much later in the blue cluster at 101 ms (panel C closed circles).

Note, that the times to achieve equilibrium for the yellow and green clusters approximately coincided with the time to achieve the peak of the global Ca^{2+} signal (~85ms). In contrast, the red cluster reached its fixed point before and the blue cluster after the peak of the global Ca^{2+} signal had already occurred (panel A, black curve). However, Ca^{2+} dynamics in all spatial domains eventually regained stability with their Ca^{2+} peak values occurring at different times. Importantly, following the completion of the first global CaT, and before the onset of the next CaT, oscillations in the stability of the Ca^{2+} dynamic *only* observed in the red cluster, following which the Ca^{2+} dynamic of the red cluster, eventually

moved to the vicinity of an unstable fixed point (~180ms) to initiate the foot of the global CaT in the next cycle. The Ca^{2+} dynamic of the three other clusters reached their unstable points recapitulating the events during the initiation of the prior global CaT.

3.2. Instantaneous frequency components of the SAN Ca^{2+} dynamics within SAN spatial domains

Because Ca^{2+} dynamic characteristics within SAN regional clusters are ultimately derived from the frequency characteristics of biologic noise [29, 30] underlying LCOs , the frequency components of the total power (energy) expended in each cluster must differ. We quantified frequency domain characteristics of Ca^{2+} dynamics in each color-coded cluster throughout the entire 2.7-sec time-series recording by Hilbert-Huang Transforms (HHT) [31] (Fig. 6A). The series of Ca^{2+} impulses of four color-coded clusters (panel A top tracing) are decomposed into several empirical mode functions (IMF, panel A lower traces) from which *instantaneous* frequency ranges were extracted. Examples of IMFs 2-3 that contain the highest power (energy) within Ca^{2+} dynamics are shown in Panel A (lower panels), panel B shows the power of that energy distribution across *instantaneous* frequencies within the four color-coded clusters (the entire range of frequencies is shown in Fig. S2).

Note that a large range of frequencies from low (2Hz) to high (15 Hz) are embedded within the Ca^{2+} dynamic of four color-coded clusters (panel B). The dominant frequency of highest power (energy) within the Ca^{2+} dynamic of each color-coded cluster emerged at 6.6Hz in the red cluster, 5.9Hz in the yellow, and about 5.1Hz in the green cluster. Although the dominant frequency of the blue cluster was similar to that of the red cluster (around 6.6Hz, Fig. 6B), the blue cluster exhibited much lower energy (power) at this frequency.

In order to determine frequency-time-power relationships of the Ca^{2+} dynamic of each of the four color-coded regions, we applied a modified Short-Time Fourier Transform (with window size fixed in the frequency domain, STFT-FD)[32] to convert regional signals to the time-frequency and amplitude domains. Figure 7 shows transformed regional Ca^{2+} signals between 0.3-0.75 sec during the time series recording in which three SAN global CaT emerged. A range of frequencies from low (indicated by oval 1) to high (indicated by oval 2) was observed in transformed Ca^{2+} signals in all four color-coded regions (Panels A-D, red, yellow, green, and blue, respectively). Note, however, that in the red cluster (Panel A) high and low frequency components and the frequency power (see the bar code) were larger, and the abrupt transition from lower to higher frequencies in this

cluster began earlier during the foot of each CaT (Panel A) compared to other clusters (Panels B-D).

3.3. Energy transitions within the Ca^{2+} dynamics *among SAN clusters*

We next examined the dynamic of energy transitions within the Ca^{2+} dynamics in each color-coded cluster throughout the time-series. Functional data analysis (FDA**) [33]** of acceleration in relation to velocity examines nonlinear dynamics and details of acceleration versus velocity transitions within the phase plane that drive time-dependent changes in the amplitude of the Ca^{2+} dynamics. The functional heterogeneity could be clearly observed in the FDA trajectories. When *both* velocity and acceleration are *zero*, a system is in the equilibrium and no energy is being transferred. When *either* acceleration or velocity are *non-zero*, the system is in motion and energy is being transferred from potential to kinetic energy for a given purpose. When either acceleration or velocity is *negative*, kinetic energy is being transferred back to potential energy and vs versa. If the potential and kinetic energies within the FDA function form a perfect circle (acceleration and velocity simultaneously crossing at 0:0) the system would achieve their equilibrium, potential and kinetic energies are equal, and no energy would be transferred. The color-coded map depicted the SAN functional clusters in Fig 1C is shown again in Fig. 8A, and panel B illustrates the averaged amplitudes and derivatives of the Ca^{2+} dynamic in each of the four color-coded areas in panel A during a 500 ms segment of the 2.7-sec time-series of Ca^{2+} recording.

Panel C illustrates the phase-plane diagrams of the acceleration vs velocity during the 500ms in panel B, and panel D encompasses the time of the first impulse in panels B and C. Panel E shows a zoomed low energy state in panel D (0-46ms during impulse formation), that includes events near zero crossing. Phase-plane plots of Ca2+ dynamic derivatives of the four color-coded SAN functional clusters (Panels C and D) showed a nonuniform pattern. Panel F provides a detailed illustration of the foot formation state depicted in panel D, covering time intervals from approximately 46.1 ms to 65 ms during impulse formation.

Note that the plots of derivatives of the Ca^{2+} signal in panels C and D form two circular-like trajectories of *unequal* size, *neither* of which forms a perfect circle. The absence of *0:0* crossings indicates that the SAN Ca^{2+} dynamics never achieve a true equilibrium. Phase-plane analysis (Fig. 8C, 8D, and 8E) indicates that the kinetic transitions of Ca^{2+} signals within regional Ca^{2+} clusters near the termination of one impulse and initiation of a subsequent impulse hovered around 0 velocities, meaning

that little or no energy is being transferred at that time, (as the system approaches equilibrium at the zero crossing).

A rotor-like oscillatory behavior ('knot') around the zero crossing is followed by trajectories that project throughout the entire velocity-phase plane. Panel D clearly shows differences in the kinetic variation among four color-coded functional clusters (see black arrows) during impulse formation, particularly between red and the other three clusters. It is important to emphasize that the red cluster's Ca^{2+} dynamics were captured only within the specific region observed in this video, which represents 8% (4 ROIs) of the selected SAN area. The yellow cluster occupied 24% (12 ROIs), while the green and blue clusters each accounted for 34% (17 ROIs each) of the observed area (panel A).

Although the spatial extent of the red cluster was the smallest, and its Ca^{2+} dynamics near the CT had the lowest potential and kinetic energy, the acceleration-velocity trajectory of this cluster showed an early increase (entering the upper right quadrant in panels C-E), preceding significant kinetic changes in the other clusters. The timing of the energy transition observed in the red cluster aligns with the initiation of the global calcium transient (CaT) (Fig. 3), and is likely implicated in the ignition of the global SAN CaT. The kinetic trajectory of the blue cluster (near the inter-atrial septum, Fig. 8A) emerged following a delay after the trajectory initiation of the other clusters, although the magnitude of its energy transition was comparable to that of the yellow and green areas (see Fig. 8C, D).

3.4. Ca^{2+} information sharing among SAN functional clusters

Next, we employed Pearson correlation analysis to determine trans-spatial relationships of LCO dynamic (Fig. 9B) among the 50 ROIs forming four color-coded SAN functional clusters (Fig. 9A) as a function of rolling window (~15ms) throughout the first 350 ms of the time-series Ca^{2+} recordings. The normalized amplitudes of Ca^{2+} signals within each of the 50 ROIs overlaid by the global SAN Ca^{2+} impulse are shown in Fig. 9B. The color-coded map of the 50 ROIs clustering is displayed in panel A. Amplitude correlation patterns among ROIs (panels C-K) differentially emerged and decayed with time during the 350 ms time-period, during which two complete integrated (global) SAN CaT emerged (black trace in panel B). Correlation patterns prior to and during the two impulses are shown side by side in panels C-K. Blue and green numbers at the top of each time segment indicate the 1st and 2d impulses.

Prior to the initiation of each impulse (see vertical lines marked as 1(0) and 2(0) in panel B for time reference), ROI LCO amplitudes were completely *unclustered* (panel C), suggesting stochastic behavior among LCO comprising 50 ROI. During the next time segment (see vertical marked as 1(1) and 2(1) in panel B) two small clusters formed in 1(1), one of which included only 2 ROIs and the other included 3 ROIs; and in 2(1) only one cluster formed (Fig. 9D). These clusters in both 1(1) and 2(1) formed near the crista terminals (red color in the ROI map in 9A). In the following time segment (1(2) and 2(2)), Ca^{2+} signal amplitudes within a large number of ROIs formed one large homogeneous cluster, a few small clusters (Fig. 9E), and only 28% remained *unclustered* in 1(2) (Figs. S3-S4). Note, that during this specific time segment (see vertical lines in panel B for time reference), the amplitude of the integrated (global) SAN CaT slowly increased (panel B).

During the next segments (panel B marked as 1(3) and 2(3) for time reference), the clustering patterns again changed: two major clusters and a few small clusters were formed, with ~ 20% ROIs remaining *unclustered* (Fig. 9F, Figs. S3-S4). During this segment, the amplitude of the integrated (global) SAN CaT rapidly increased near its peak (Fig. 9B). During the next time segments 1(4), 2(4), one large cluster encompassing a large number of ROIs, and a few small clusters were observed, and 20% and 6% of total ROIs were *unclustered* (Fig. 9G, Figs. S3-S4). During this segment, the integrated (global) SAN CaT began to decay (panel B, black trace). In the following segments, 1(5), 2(5), large clusters of ROIs in the prior segment reorganized into two medium-sized correlation clusters a few very small clusters, and ~20% remained uncorrelated (Fig. 9H, Figs. S3-S4). At this time, the integrated (global) SAN CaT had decayed rapidly to ~50 % of its peak amplitude (Fig. 9B). In the following time segments 1(6), and 2(6), ROI Ca^{2+} signals became largely unsynchronized, and only one medium-sized cluster and three small clusters remaining, and ~28% of ROIs were uncorrelated (Fig. S4); during this time, the integrated (global) SAN CaT decayed rapidly to ~18% of its peak amplitude. The next time segments, 1(7) and 2(7) showed only a few small correlation clusters, and in 3(0) ROIs were completely uncorrelated again (Fig. 9K). Thus, during the 350 ms recording, there was an indication of memory-like behavior indicated by similar, but not exact, clustering patterns of ROIs in 1(0)-1(7) 2(0)-2(7): initially ROIs were uncorrelated, and with time a gradual shift to a higher level of correlation among ROIs occurred, followed by loss of correlation, eventually, again, with ROIs becoming completely uncorrelated.

Figure 10 shows the correlations among the kinetics of the average Ca2+ dynamics of the four color-coded SAN functional clusters and between them with the global SAN CaT during the entire

2.7-second time-series recording. The correlation between the yellow and green functional clusters was higher (r=0.90) than between the red and yellow (r=0.78) or red and green (r=0.53) functional clusters. The red and blue functional clusters negatively correlated (-0.091) with each other. There was some small positive correlation between the yellow, green, and blue functional clusters (Fig. 10). The global CaT more strongly correlated with yellow (r=0.89) and green (r=0.98) functional clusters than with red (r=0.57) and blue (r=0.53) functional clusters (Fig. 10).

Next, we aligned energy transitions during the 1st global CaT in the time-series (Fig. 9B) and the ROI correlations during time segments of the same impulse (Fig. 11). Prior to the initiation of the global CaT (foot) and at the time when there was no (Fig. 9E) or small (Fig. 9E) correlation among Ca^{2+} dynamic of any ROIs, energy transition was very low (Fig. 11B).

In contrast, during the foot of the global SAN CaT (~50-65ms) when a large number of correlations among ROI Ca^{2+} dynamics emerged (panel G), the energy expenditure was high (panels D at above 0:0, C). Phase-plane diagrams of acceleration vs velocity of the integrated (global) CaT of all 19 impulses are shown in Fig. S5.

3.5. Small-world properties and functional connectivity in SAN pacemaker activity

Previous studies have shown that SAN cytoarchitecture and function resemble neuronal tissue [7, 20], in which remarkably weak ties among neuronal cells are precisely organized to maximize information transfer with minimum wiring cost (small-world signaling). To test whether the SAN Ca2+ network exhibits small-world organization, we calculated the clustering coefficient (C) and average path length (L) of the network, comparing these against randomized networks that preserved the degree distribution of the original network. The small-world index $\sigma = (C/C_{rand})/(L/L_{rand})$ where C_{rand} and L_{rand} represent the corresponding metrics from a random network, was calculated for the Ca2+ signaling interactions between SAN tissue pixels (see methods, Fig. S1, Movie S2). Figure 12A shows that $\sigma > 1$ throughout the 2.7-second recordings.

The highest sigma (σ) peak occurred around the foot of the integrated (global) Ca^{2+} impulse, formed mostly by Ca^{2+} dynamic of the red cluster, and the lowest sigma (σ) peak occurred at about the time when the global Ca^{2+} impulse achieved its peak (panel A). Interestingly, the power of the peak σ values varied from cycle to cycle, ranging from 2.9 to 5.8 (panel A). These characteristics indicate the existence of a small-world network structure that balances efficient local information processing with rapid long-range communication (unique examples shown in panel B). The dynamics of small-

worldness closely align with the coordinated behavior of color-coded clusters: sigma is low at the peak of a given global Ca^{2+} impulse, begins to progressively grow during relaxation phase of that global Ca^{2+} impulse, and reaches its highest value around the time of the 1st derivative of the *next* global Ca^{2+} impulse. In another terms, there is no systole or diastole in the SAN signaling network (the Ca^{2+} signaling fire *never* goes out). Animation visualizes the evolving functional connections between different regions of the SAN over time and emergence of the global CaTs (Movie 4).

To visualize characteristics of Ca^{2+} signals within four color-coded clusters of the SAN Ca^{2+} network, we examined the interactions between the original signals and the reconstructed M-dimensional manifold signals in a three-dimensional phase-space, using a time dependence, nearest neighbors, and mutual information to evaluate and embed the original data in an M-dimensional manifold where all possible states could be determined from a set of initial conditions (see methods) [34]. Figure 13A shows the actual *original* red, green, and blue signals plotted against each other in a three-dimensional phase-space. Panels B-D show *reconstructed* phase-spaces of these signals (the manifold of the yellow cluster was similar to that of green and is not shown in this figure).

Although all reconstructed manifolds (panels B-D) exhibited similar rotary trajectories, suggesting some contribution of all clusters in the Ca^{2+} information within the SAN network, the *shapes* of the red and blue manifolds more closely reflected the shapes of the trajectories of the original signals in space (in pane A). Therefore, the changes in Ca^{2+} within the entire signaling network are embodied within the Ca^{2+} dynamic of red and blue clusters within manifolds.

3.6. Is the emergence of the next SAN impulse predetermined or stochastic?

Figures 1-13 indicate that global CaT is initiated within the red cluster. To examine whether global SAN CaT emergence is deterministic or stochastic in nature, we assessed the peak-to-peak variability of the Ca^{2+} dynamic within the four color-coded clusters during a 2.7-second time-series recording (Fig. 14A). The mean peak-to-peak interval of the global CaT (broken line in panel B) and all four color-codded clusters during the 2.7-second time-series recording was ~145.2-145.3ms (panel B solid line). The standard deviation (SD) of the peak-to-peak intervals of the global CaT and three other colors was ~ 0.71 ms (panel B). In the red cluster, however, the SD of the peak-to-peak interval of the Ca^{2+} dynamic exceeded that of both the global and each of the other clusters by about >30%, indicating that the timing of the Ca^{2+} dynamic that initiates each global CaT manifests substantial variability from one impulse to the next (panel A, red color-coded cluster).

Orbit plot analysis of microelectrode recordings of SAN impulses, a powerful visualization tool to analyze and decompose the dynamics behavior within complex systems over time, had been interpreted to indicate that SAN impulse formation is deterministic in nature (chaotic) [35, 36]. We constructed orbit plots, which embed additional dimension of time-shifting segments (7ms) throughout 2.7 sec of Ca^{2+} dynamics [35, 37]. Fig. 15 shows orbit plots constructed from the spatially averaged Ca^{2+} dynamics within the four color-coded clusters (three cycles, panel A) as the unlagged and lagged (7ms) versions of itself during 500 ms (panel B, three impulses), 180 ms (panel C, one impulse) and 65 ms (panel D, 'pre-foot' and 'foot' formation) of impulse generation.

Note however, that each of the color-coded Ca^{2+} dynamic trajectories begins with a small oscillation, as clearly seen in panel D, at that a clockwise elliptical-like trajectory ended near to its starting point, but not exactly at always at the same starting point (Panels B-C). This difference in the initial condition creates variability of orbits within a given cluster, suggesting that SAN Ca^{2+} dynamic is not purely deterministic but partially stochastic. Example of orbit plots of individual ROIs from each of the four color-coded cluster during entire time-series showed some degree of impulse-to-impulse variability observed within each cluster (Fig S6). However, it seems that variability within the red cluster was higher relative to that of other clusters.

The difference in the interpretation of orbit plots of Ca^{2+} dynamics of present study and microelectrode study [35] maybe due to different mechanisms that underlie Ca^{2+} and Vm dynamics: spontaneous calcium releases driven by a self-organizing critical state underlie SAN calcium dynamics, while membrane potential signals follow limit cycle behavior [26].

Ca^{2+} dynamic analyses indicate that the SAN Ca^{2+} dynamic is a self-sustained regenerative impulse formation, with the status of Ca^{2+} signals at the end of one impulse becoming the initial conditions for the next impulse (Fig. 12A arrows in the nadir). To quantify the degrees of stochastic and deterministic behavior embedded within the 2.7 sec time-series recording, we calculated the Lyapunov exponent (λ), a measure of how quickly nearby Ca^{2+} dynamic trajectories in the phase-space diverge over time. To estimate λ, we employed a two-dimensional phase space reconstruction technique optimized for capturing system dynamics, while maintaining statistical robustness with two-dimensional embedding (Fig. 16) which affords visualization of the system's trajectory in phase space, effectively capturing the essential dynamics of the Ca^{2+} signaling network (see Methods).

Figure 16, panel A illustrates an example of the strongly deterministic (chaotic) behavior of a Lorenz attractor ($\lambda = 0.146$), panel C illustrates the behavior of a stochastic sinusoidal wave ($\lambda \approx 0.0001$,

panel C), and panel B illustrates the behavior of the SAN global CaT ($\lambda = 0.082$). The positive Lyapunov λ of the SAN Ca^{2+} signaling network confirms its sensitivity to initial conditions, consistent with the nonlinear patterns and memory observed in the orbit plots (Figs. 15, S6).

The SAN Ca2+ signaling network exhibits a Lyapunov exponent ($\lambda = 0.082$) intermediate between the strongly chaotic Lorenz attractor ($\lambda = 0.146$) and a noisy sinusoidal wave ($\lambda \approx 0.0001$). This indicates moderate chaotic dynamics with sensitivity to initial conditions, but more structured than the Lorenz attractor and not purely random, complementing the results of the complex dynamics in stability and orbit plots (Figs. 5, 15, S6). Analyses of the Lyapunov exponent (λ) for each of the four color-coded clusters outputted equal to $\lambda = 0.0570$, $\lambda = 0.0531$, $\lambda = 0.0566$, and $\lambda = 0.040$, for red, yellow, green, and blue clusters respectively. This suggests that the Ca^{2+} dynamic of the red but not the blue cluster was closer to the Lorenz attractor. This means that small changes in the initial condition of the red cluster can influence the subsequent trajectory of the Ca^{2+} signal in time-series, infusing a variability signature into impulses in the time-series. It is important to note that the Lyapunov exponent for integrated SAN Ca^{2+} dynamic ($\lambda = 0.082$) is greater than that of any given cluster, indicating that deterministic behavior, in addition to stochastic behavior, is embedded within the SAN Ca^{2+} dynamic.

3.7. Deduction of the SAN action potentials from the kinetic transitions within the global Ca^{2+} transient

To examine the relationships of Ca^{2+} dynamics of the regional clusters and electrical impulse (AP), generated by the SAN and conducted to the atria, we inserted a sharp microelectrode into the right atrium adjacent to the crista terminalis (CT). Figure 17A shows that the peak of the AP recorded in the atria occurred approximately before the peak of the Ca2+ impulse of the yellow cluster, well before the completion of the Ca2+ dynamic of the entire SAN (panel A). We used the timing of the atrial AP during the impulse formation to deduce the *SAN AP* (panel B). The SAN AP must have occurred prior to the time at which the AP was recorded in the atrium. The dotted trace in panel B is the deduced (putative) SAN electrical field potential. It is evident that the Ca^{2+} signal of the red cluster gradually increases at between 45-64ms, i.e., prior to the initiation of the rapid upstroke of the putative SAN AP. We refer to this time period as the ignition phase of the putative SAN AP, following which AP rapidly increases to its peak amplitude in about 4-5 ms (panel B). The rapid upstroke of the SAN putative AP triggers rapid increases in the Ca^{2+} signal in the yellow cluster, closely followed by a rapid increase in the green clusters. The Ca^{2+} signal within the blue cluster initially slowly increased

to the plateau at ~77 ms and then, following substantial delay, manifested a fairly rapid increase to a peak amplitude at ~100 ms (panel B). Relationships of the deduced SAN AP to the global CaT and to the atrial AP are shown in Fig. S7.

4. **Discussion**

We applied novel analytical paradigms to the time-series of Ca^{2+} images to extract information about how heterogeneous (stochastic) local Ca^{2+} oscillations (LCO) *of SAN* pacemaker cells (see Movie S1) become synchronized to form rhythmic SAN impulses.

4.1. Synchronization of Different Ca^{2+} dynamics within different SAN regions create global SAN impulses

We discovered that LCO dynamics within SAN pacemaker cells incessantly became synchronized differently in the different SAN regions, creating regional spatial clusters, in which the global CaT dynamics differed from other clusters (Figs. 1-17). Repetitive time-dependent synchronization of LCO dynamics within and among these spatial clusters created discrete rhythmic global SAN CaT, and the Ca^{2+} dynamics within regional clusters imparted different features to the global CaT (Fig. 8). Variable signatures of synchronization of patterns of Ca^{2+} dynamics of clusters during an impulse was linked to inter-impulse interval variability within time-series of impulses (c.f. Figs. 1, 14). The synchronization of the Ca^{2+} signal in one small cluster (color-coded red) was the first to increase, making the major contribution to the foot of the global CaT (c.f. Figs. 1, 3-4, 6, 16), followed by increase LCO synchronization in two adjacent large clusters (color-coded yellow and green) made the major contribution to the upstroke of the global CaT (c.f. Figs. 1, 3-4, 6, 16). This rapid phase was very brief, achieving a peak in ~5ms from its onset, and occurred prior to the time at which the peak of the global CaT was achieved (Fig. 3) and approximately coincided with the time at which the peak of AP was recorded in the right atrium (Fig. 16). This is in agreement with observation that electrical impulses, measured via voltage-sensitive fluorescent indicators in mouse SAN, activate the atria prior to the time at which the SAN AP is completed [38, 39] .

Confocal SAN immunolabeled images also indicate that within some SAN regions, pacemaker cells expressing HCN4 *intertwine* with other cells that express Cx-43, and that the density of Cx43 expression increases as the distance beyond the intertwining area increases ([16]. It is reasonable to speculate that an electrical impulse, presumably generated during the foot of the global CaT, is transmitted to adjacent clusters (color-coded yellow and green) via a network of intertwining HCN4+ , Cx- 43+ cells [16]. The SAN electrical impulse is then *rapidly* conducted in the direction in which density of

517 Cx43 expression increases, generating an action potential (AP) in adjacent clusters (e.g. color-coded
518 yellow and green, Fig. 1C). The similarities of the initial slow and rapid kinetic phases of the global
519 SAN CaT to the initial slow and rapid kinetic phases of the Ca^{2+} transient in single pacemaker cells,
520 suggests that, although not directly measured in the present study, the integrated low-amplitude ini-
521 tial signaling (both Vm and Ca^{2+}) in SAN, analogous the slow diastolic depolarization in individual
522 cells, emerges from self-organization and synchronization of heterogeneous LCOs within regional
523 clusters that formed the foot of the global Ca^{2+} impulse (c.f. Fig. 1, color-coded red). The subsequent
524 rapid phase of the SAN global CaT is triggered by the rapid upstroke of the SAN electrical impulse
525 (AP) (Fig. 17B).
526 Interestingly, the timing and kinetics of the Ca^{2+} dynamic within the SAN functional cluster, ap-
527 proximately located in the mid-SAN, and extending toward the septum (c.f. Fig.1C, color-coded
528 blue), differed from those of each of the other clusters. Specifically, the Ca^{2+} dynamic of this blue
529 cluster began, as in the red cluster (clearly seen in Fig. 1D, blue), to slowly increase during the 'pre-
530 foot 'of the global SAN CaT and then began to increase, as in yellow and green clusters during this
531 time, but then plateaued (stalled), as if the conduction of an electrical impulse were "blocked" from
532 entering into this cluster (Fig. 3). Indeed, the location of this cluster within the SAN approximated
533 that, which in prior studies, has been referred to as a 'block zone', into which the SAN electrical im-
534 pulse fails to be conducted [39-41]. One potential cause of impulse block into this area might be an
535 absence of a zone in which HCN4 expressing pacemaker cells intertwining with those expressing
536 Cx43 [16, 20]. Other often-cited causes of impulse block are bands of fibrous tissue, or branches of
537 the SAN arterial system [39]. After a substantial delay, however, the Ca^{2+} dynamic of this cluster be-
538 gan to increased rapidly (as in the yellow and green clusters), reaching its peak amplitude at a time
539 that was well beyond the time at which the peak of the AP reference electrode in the atrium was rec-
540 orded. The peak of the Ca^{2+} dynamic of this cluster also occurred beyond the peak of the global
541 SAN CaT (Figs. 3, 8, 17), making a major contribution to the relaxation phase of the global CaT
542 (Figs. 1,3-4). An increase in Ca^{2+} during this time may contribute to the repolarization of the SAN
543 AP, via impacting on Ca^{2+}-dependent K+ channels [42-44].
544 It has been noted previously that it is not possible to define the exact anatomic medial border of
545 the SAN [39-41, 45] and it is possible that the blue cluster is actually part of the right atrium, and
546 not part of the SAN. The rate at which the delayed Ca^{2+} increase occurred in this cluster was rapid
547 (Figs. 3, 16), suggesting that it was triggered by an electrical impulse, possibly by a *delayed reentry*

548 *of an electrical signal into this SAN cluster. Because the excitation of the left atrium is delayed com-*
549 *pared to that of the right atrium* [46-49] the source of this delayed excitation may have been from
550 within the interventricular septum or from the left atrium, reentering the blue cluster, possibly via
551 Bachmann's or precaval bundles [45, 46]. Sinus node reentry in the rabbit heart has been previously
552 directly demonstrated in response to an ectopic beat [50, 51]. Numerous studies have indicated
553 that electrical impulses originating in the left atrium enter the right atrium during reentrant arrhyth-
554 mia, e.g. atrial fibrillation [48, 49, 52, 53]. To our knowledge, our results are the first to demon-
555 strate a reentrant-like phenomena into the SAN on a beat-to-beat basis.
556 If a conduction block of the impulse into this (blue) cluster were to be bi-directional, a delayed elec-
557 trical impulse into the block cluster would not be expected to be conducted back to the adjacent (red)
558 cluster, in which the earliest increase in Ca^{2+} was observed, and would not be expected to have an
559 effect to dictate the ignition process of the global CaT occurring in this (red) cluster (Fig.1C). In other
560 terms, failure of a delayed reentry of an electrical signal into the red cluster would prevent a com-
561 plete reentrant circuit that would prevent variability in the ignition process of SAN global CaTs
562 manifest as variability in the initiation phase of orbit plots (Figs. 15, S6) and energy transfer in
563 FDA (Figs. 7, 10, S5), and point instability of Ca^{2+} dynamic in the red cluster, initiating the next
564 global CaT.
565 Thus, our results demonstrate that regional clusters of SAN pacemaker cells display different types
566 of Ca^{2+} dynamics, in part, resulting from different spatiotemporal synchronization of LCOs, and that
567 incessant, spontaneous, spatiotemporal synchronization of LCOs within a small cluster, forming the
568 foot of a global SAN CaT, that creates initial triggered synchronization of some adjacent SAN clus-
569 ters (Figs. 1, 3-15, 17), forming a rapid upstroke of the global SAN CaT. A delayed, apparently trig-
570 gered increase in Ca^{2+} (blue cluster) in an initially "blocked" cluster completes the SAN global CaT.
571 The phases of the SAN AP can be deduced from the kinetic Ca^{2+} dynamics of the SAN cluster net-
572 work (Figs. 1, 3-15). We may speculate that a small local electrical field potential (LFP) generated by
573 Ca^{2+} dynamics of a small cluster of SAN pacemaker cells, initiates diastolic depolarization (DD) of
574 SAN AP. Indeed, a slowly rising small foot of SAN AP (coinciding with the formation of the slow
575 foot of the SAN global CAT in the present study) has been demonstrated directly in studies that
576 have employed voltage-sensitive fluorescent indicators [52, 53]. As the Ca^{2+} dynamic of this cluster
577 continues to increase exponentially, LFP, generated by this cluster continues to increase, leading to
578 an exponential increase in DD that brings the membrane potential to the threshold of Ca^{2+}/Vm

activated L-type Ca^{2+} channels, creating the rapid upstroke of the SAN AP, which triggers a rapid increase in the global CaT. The time at which this occurs is slightly delayed from the time at which the peak of the SAN/right atrial AP occurs in voltage-sensitive fluorescent recordings in mouse SAN [54]. Delayed electrical impulse into a cluster near the inter-atrial septum (blue cluster) triggers a delayed increase in Ca^{2+}, which in conjunction with the desynchronization of LCO throughout the SAN, contributes to the repolarization of the SAN AP (Fig. 17).

4.2. The energy and frequency distributions within SAN CA dynamic

The energy and frequency distributions of structured 'biologic noise' of Ca^{2+} dynamics (2Hz to 15Hz), of each regional cluster could easily be discriminated from that of non-biologic noise (15-50Hz, (Fig. 6, Fig. S2). The LCO within the regional cluster that formed the initial component of an impulse (foot of the global CaT typically located near the CT, Fig. 1C, color-coded red) had the *highest* power and oscillated around a slightly higher dominant frequency than other regional clusters (Figs. 6B, S2). The Ca^{2+} dynamic within this cluster had a slower rate of rise, and, due to its small spatial area (Fig. 1C, red), achieved a lower amplitude (c.f. Fig 3A) compared to that of other regional clusters within the SAN network.

Confocal SAN Ca^{2+} images in prior studies indicate that the area, in which the earliest Ca^{2+} impulse could be detected, was near CT, as in the present study, expressed HCN4, but not Cx43 [16]. The slower rate of rise of the Ca^{2+} dynamic of this cluster (red) (Figs. 3, 8), forming the foot of the global CaT (Fig. 2), in the context of having the highest power may be explained by a lower coupling of pacemaker cells to each other in this cluster compared to that in other clusters. In single isolated SAN pacemaker cells self-ordering of local Ca^{2+} oscillations initiates a global, cell-wide, CaT. Simultaneous measurements of both Ca^{2+} and membrane potential (Vm) demonstrate that Ca^{2+} kinetics during the foot of an AP is a major determinant of the kinetics of diastolic depolarization that initiates the rapid upstroke of the AP ([28, 55]. Thus, the initial slow phase (foot) of the global SAN CaT in the present study that is generated within a regional SAN cluster (Fig. 1C color-coded red), in which HCN4 (If) is highly expressed, is strikingly similar to the ignition phase of an AP in single pacemaker cells [28] .

The small gradual increase in Ca^{2+} accompanied by a foot of deduced SAN AP is strikingly similar to the DD phase observed in single pacemaker cells studied in isolation, in which an ensemble Ca^{2+} signal, coupled to cell surface membrane electrogenic proteins, initiates small, rhythmic, spontaneous oscillations (ignition) of the cell surface membrane potential i.e. the diastolic depolarization (DD),

aka, the "pacemaker potential" [27]. This is followed by the rapid upstroke of the AP in single cells, which triggers a rapid increase in Ca^{2+} [28, 55]. Similarly, the deduced SAN AP triggers a rapid increase in Ca^{2+} in SAN tissue (Fig. 17B).

4.3. Energy and stability transitions within nonlinear Ca^{2+} dynamic

Energy expenditure, which was of low amplitude, began as a rotor-like trajectory of acceleration and velocity within the Ca^{2+} dynamic in each cluster and was reflected as a state of low energy transfer, which then progressively increased during the impulse formation (Figs. 8, 11, S5). The cluster in which the rotor appeared first was a cluster that initiated the ignition phase (foot) of impulse, followed by the appearance of the rotor in other clusters (Fig. 8E). The rotor-like trajectory initiations and expansions in each cluster varied within different impulses during time-series (Figs. 8). Importantly, energy transfer within the SAN Ca2+ dynamic n*ever* achieved true equilibrium in any cluster during a time-series of impulses. Although the *total* energy expenditure in the red cluster, in which spontaneous LCO *self-ordered*, was substantially less compared to that in other clusters (Fig. 8C-D), it was sufficient to drive the rate and rhythm of other clusters in which energy expenditure during impulses was much greater. The greatest energy expenditure occurred during the rapid increase of the global CaT (Figs. 8, 11, S5) and was reflected in a greater expansion of the rotor-like trajectory acceleration and velocity in all clusters. Mechanisms that underlie a rotor-like energy transfer within the SAN Ca^{2+} dynamic are likely related to the impact of nanoscale mechanical-electro-chemical-thermal factors [56] on molecules of the coupled-clock system within SAN pacemaker cells [8].

Transitions in stability and energy of Ca2+ dynamics mirrored each other within each cluster (Figs. 5, 8, 11, S5). Throughout the time-series of impulses, initial conditions of the Ca^{2+} dynamic initiation within clusters were not strictly identical to each other. Variability in initial conditions is likely a cause of peak-to-peak variability of the SAN Ca^{2+} global impulses during a time-series, and therefore would be expected to be a mechanism of cycle-to-cycle variability observed previously in SAN Aps [16]. Importantly, stability oscillations and energy transitions within the red cluster that were initiated by a subsequent impulse occur even before such transitions in other clusters had fully stabilized within a prior impulse (Figs. 5C, 8E).

Different solutions within and among four color-coded clusters at the end of a previous cycle and the beginning of the next cycle, i.e. variable initial conditions, result in the different interactions between

640 components of the same system and could contribute to the range of frequencies and beat-to-beat var-
641 iability of the global CaT. Some potential factors that could contribute to these variable interactions
642 include:

643 • Heterogeneity of cells within a given cluster: there may be cells with different functional and
644 metabolic properties In a single color-coded clusters. This heterogeneity can lead to varia-
645 tions in the baseline Ca^{2+} levels and response to stimulation, resulting in different trajectories
646 and patterns of response during impulse formation.
647 • Differential expression of Ca^{2+} signaling proteins: Different cells may express different lev-
648 els of Ca^{2+} signaling proteins, such as ion channels and pumps, which can affect the response
649 to stimulation and the dynamics of Ca^{2+} signaling.
650 • Uneven distribution of inputs: Even within the same cluster, there may be variations in the
651 distribution of inputs from neighboring cells or regions. This can lead to differences in the
652 spread and strength of the Ca^{2+} signal, resulting in different trajectories.
653 • Feedback and cross-talk between pathways: Ca^{2+} signaling pathways can interact and influ-
654 ence each other, leading to crosstalk and feedback mechanisms. This can result in variations
655 in the response of different cells within the same cluster.
656 • Environmental factors such as local differences, e.g. changes in temperature, pH, or oxygen
657 levels can also affect the dynamics of Ca^{2+} signaling. Differences in these factors within and
658 between four color-coded clusters can contribute to differences in the trajectories of Ca^{2+} sig-
659 nals.

660 Further studies are needed to fully understand the contributions of these factors and how they may
661 impact the overall coordination and variability of Ca^{2+} signaling in complex cellular networks.
662 Our results showed that local heterogeneous Ca^{2+} signals and synchronized Ca^{2+} signals create dis-
663 creet global CaT that manifest both stochastic and deterministic characteristics and that these differ
664 from one impulse to the next. Cycle-to-cycle variability (Fig. 14) can be linked to stochasticity at-
665 tributable to the variable alternation between stable and unstable states (Fig. 5) within the time-series
666 of impulses, causing the initial conditions of each impulse to be not exactly the same. But following
667 the initial phases of each impulse, similar but not exactly the same phase-plane FDA trajectories
668 (Figs. 8, 11, S5) or orbit plots (Figs. 15, S6) of Ca^{2+} dynamic show similar shape, suggesting the de-
669 gree of deterministic (chaotic behavior) ensures successive impulse. Earlier studies using simpler

analytical methods concluded SAN impulses were purely deterministic [35, 36]., but our multi-dimensional analysis reveals a more complex picture.

4.4. Networking of Ca^{2+} dynamics within the SAN

PCA indicated that all clusters within SAN network contributed to the SAN impulse, but the magnitude of each contribution varied during the time of the impulse formation (Figs. 4, S1), with a small cluster (color-coded as red) contributing to the majority of the energy during the foot (Figs. 4A, 8C, D) of the global CaT prior to the rapid upstroke.

Pearson correlation analysis showed that time-dependent synchronization/desynchronization of the Ca^{2+} dynamics within each cluster throughout time-series formed global Ca^{2+} impulses within the time-series (Figs. 9-10); and within a given temporal epoch during an impulse, the kinetics and amplitudes of functional Ca^{2+} dynamics in *different* regional pacemaker cells clusters, became correlated with each other, pointing to the creation of a time-dependent, correlated *network function among the clusters*. The magnitude of correlations also differed between clusters, e.g. the yellow and green strongly correlated to each other than to other clusters; the red and blue clusters negatively correlated, which is consistent with the above different functional properties of regional clusters (Fig. 10).

Small-world network analyses detected the presence of small-world signaling throughout 2.7. sec time-series (Fig. 12), indicating a network architecture capable of balancing local connectivity with global integration (Fig. 12B), ultimately forming *a unique* spatiotemporal LCO synchronization solution to create each impulse.

Beyond correlation analyses, PCA analyses, and small world analyses, manifold analyses confirmed that the information contained in the time-series of Ca^{2+} dynamic specific to one cluster informs on Ca^{2+} dynamics of the entire *cluster network* (Fig. 13).

4.5. The SAN network nonlinear Ca^{2+} dynamic features both deterministic and stochastic behavior

Orbit plots, in which segments of the Ca^{2+} dynamic, informed on an additional embedded dimension, demonstrated that the limit cycle behavior during a given impulse varied within and among clusters, and moreover that the clusters variability varied from one impulse to the next during the time-series (Figs.15, S6). Variations of regional Ca^{2+} signals during each cycle could explain, at least in part, why

each orbit is unique, i.e. represents a unique solution of a complex signaling network to generate a given pacemaker cycle. But because orbits do not return to the exact initial points cross time-series provides the hint that SAN Ca^{2+} dynamics are not strictly deterministic as suggested earlier (Jallife 1999) but that some degree of stochasticity is embedded within spontaneous SAN Ca^{2+} dynamics. The stochasticity of SAN Ca^{2+} dynamic within time-series likely stems from the stochastic nature of LCOs and their interactions with surface membrane proteins that initiate DD in SAN pacemaker cells [7-9, 11]. Although information sharing varies from cycle-to-cycle, similar shapes of FDA and orbit plots all exhibit similar trajectories, indicating the presence of memory within a network of ROI clusters. This memory in SAN tissue recapitulates in single pacemaker cells that manifest cycle-to-cycle variability [55] in a given quasi-steady state. Beat-to-beat variability in LCR periodicity and the ion channel currents reflects beat-to-beat variability of the memory within the coupled-clock system. SR Ca^{2+} content is one facet of the coupled-clock memory because it is determined by Ca^{2+} released from the SR. Ca^{2+} is pumped into SR and spontaneously leaks from the SR or it release is triggered by CICR at each cycle, some Ca^{2+} is extruded from the cell, and other Ca^{2+} ions enter the cell during each cycle. However, the Ca^{2+} content in the SR in a given quasi-steady state is not exactly the same from one cycle to the next. The impact of Ca^{2+} on target molecules within the membrane clock is another facet of memory within the coupled-clock system. These molecules vary with their phosphorylation state as does Ca^{2+} pumping into SR and Ca^{2+} release from SR via RyR.

The Lyapunov exponent ($\lambda = 0.082$) indicates the SAN Ca2+ signaling network exhibits chaotic dynamics, though less sensitive to initial conditions than the Lorenz attractor ($\lambda = 0.146$), suggesting structured rather than purely random behavior.

Therefore, despite the sensitivity to initial conditions (a chaotic feature) and the presence of random events (a stochastic feature), the SAN maintains an overall stable rhythm. This stability in the face of both chaotic dynamics and stochastic processes is achieved through the bounded nature of the system, while individual cycles may vary due to both deterministic chaos and random fluctuations, the overall behavior remains within certain physiological limits. This delicate balance between chaos, stochasticity, and stability allows the heart to respond flexibly to physiological demands while maintaining overall reliability, a perfect arrangement for the critical task of regulating the heartbeat.

Thus, Ca^{2+} dynamics within and among different SAN regions incessantly change over time to create rhythmic SAN global CaT. The earliest regional changes in the Ca^{2+} dynamics reflect the synchronization of LCOs, likely producing the slow 'foot' of the SAN AP. This is followed by a rapid

acceleration of Ca^{2+} in other functional clusters, impacting a rapid increase in acceleration and velocity of the global Ca^{2+} impulse.

Variations of regional Ca^{2+} signals explain why each cycle is unique, i.e. represents a unique solution of a complex signaling network to generate a given pacemaker cycle. Although a unique solution implies a degree of stochasticity within Ca^{2+} system dynamics during impulse formation, orbit plots maintain similar shapes across multiple impulses, demonstrating stable long-term behavior. Continuous energy transfers between states (shown in velocity-acceleration plots) maintain rhythmic impulse generation during both active and recovery phases. Thus, a moderate level of deterministic chaos allows the heart to maintain a generally stable rhythm, while still being adaptable to changing physiological needs.

4.6. Limitations and segue to future research

A limitation of the present study, as in prior studies with microelectrodes and voltage-sensitive fluorescence probes, is that Ca^{2+} dynamics were assessed in 2D. Presently however no techniques to measure Ca^{2+} in 3D with appropriate time sampling commensurate with Ca2+ kinetics. Nonetheless, our 2D measurements of SAN Ca^{2+} dynamics provide novel perspectives on a network of functional clusters within the SAN in which Ca^{2+} dynamics differ from each other and differentially contribute to the formation of SAN global impulses. Because SAN structure and function in mice are similar to those of other species, including humans [39], perspectives gleaned from mouse SAN Ca^{2+} dynamics create a vista of segues into discovering the impact of SAN local Ca^{2+} dynamics on: initiation and maintenance of SAN arrhythmias; changes in the rate and rhythm of SAN impulse generation in response to stimulation or inhibition of autonomic receptors, and other neurotransmitters; pathophysiology of SAN aging, and sick SAN syndrome. The present results also inform on required design features of novel numerical models of SAN impulse formation.

4.7. Summary

Spontaneous, stochastic, local Ca^{2+} oscillations (LCOs) that are heterogeneous in phase, frequency, and amplitude incessantly occur throughout the SAN cytoarchitecture. Phase analysis delineated a network of functional pacemaker cell clusters, in which Ca^{2+} dynamic amplitudes, kinetics, and phases were similar, but still differed from each other, and differed from those of other clusters.

Local Ca^{2+} dynamics within the network of clusters formed rhythmic global Ca^{2+} impulses, with a mean rate identical to that recorded by the reference sharp electrode in the right atrium. The mean peak to peak interval of the global CaT was identical to the mean peak to peak AP interval, recorded by a sharp intracellular microelectrode in the right atrium, indicating that the frequency of the global CaTs was the same as the frequency of electrical impulses that emerged from the SAN to activate the atrium.

Cross-talk among Ca^{2+} dynamics among different clusters that varied, not only throughout an impulse, but also from one impulse to the next. The functional clusters formed unique dynamic small-world networks, assessed as Ca^{2+} dynamic cross-talk throughout time-series recordings, manifested small-world signaling characteristics, assessed as ratios of clustering coefficients to shortest path lengths, ultimately forming *a unique* spatiotemporal Ca^{2+} dynamic synchronization solution for each global CaT. Orbit plots and Lyapunov exponent analyses detected both deterministic and stochastic features within the SAN Ca^{2+} dynamics. Initial conditions of each impulse initiation differed from each other, due mostly to the stochastic nature of Ca^{2+} dynamics within a small cluster located near the crista terminalis, which formed the foot of each global CaT. This cluster had the highest intrinsic power, earliest rotor-like energy transfer, most frequent point-to-point instability, earliest acrophase, and greatest impulse-to-impulse variability within the network of functional clusters. Ca^{2+} dynamics within this cluster formed the foot of each global CaT, following which the amplitude of the CaT increased rapidly, due to rapid increases in the kinetics and amplitudes of Ca^{2+} dynamics in some adjacent clusters. Thus, the unique emergence of each CaT from individual LCOs during each cycle underlies cycle length variability in SAN impulses, and recapitulates the emergence of spontaneous CaTs in isolated, single, SAN pacemaker cells.

Funding: This research was supported by the Intramural Research Program of the National Institutes of Health, National Institute on Aging.

Institutional Review Board Statement: The animal study was reviewed and approved by the Animal Care and Use Committee of the National Institutes of Health (protocol #457-LCS-2027).

Conflicts of Interest: The authors declare no conflict of interest. The funders had no role in the design of the study; in the collection, analyses, or interpretation of data; in the writing of the manuscript, or in the decision to publish the results.

Abbreviations

AP - action potential

Acrophase - period to the peak's max value

Acceleration – 2d derivative

CaT - action protentional-induced Ca2+ transients

Chronopix -chrono-pixel

phases were similar

CT – crista terminalis

CX43 - Connexin 43 (Gap junction alpha-1 protein)

dCaT/dt – 1st derivative of CaT (1st Deriv)

d2CaT/dt2 – 2d derivative of CaT (2d Deriv)

d3CaT/dt3 – 3d derivative of CaT (3d Deriv)

IROC - instantaneous rate of change

F/F0 – normalized Ca2+ fluorescence (max/min)

FDA - functional data analysis

Foot - ignition phase of each impulse

Functional clusters – regions of interest with similar Ca^{2+} dynamics

HCN4 - hyperpolarization-activated cyclic nucleotide-gated channel

LCO - spontaneous, stochastic, local Ca^{2+} oscillation

IVC - inferior vena cava

IMF - empirical mode function

Lyapunov exponent λ - defines the rate of separation of two initially close trajectories

NCX - Na+/Ca2+ exchanger

PCA - principal component analysis

PC1 - principal component one

PC2 - principal component two

ROI - region of interest

SAN - sinoatrial node

sigma (σ) – small-world metric of the clustering coefficient to the shortest path length

Small-world network - quantifies efficient information seclusion and integration

SVC - superior vena cava

Velocity – 1st derivative

References

1. Berridge MJ, Bootman MD, Roderick HL. Calcium signalling: Dynamics, homeostasis and remodelling. Nat Rev Mol Cell Bio. 2003;4(7):517-29. doi: 10.1038/nrm1155. PubMed PMID: WOS:000183892000011.
2. Berridge MJ, Lipp P, Bootman MD. The versatility and universality of calcium signalling. Nat Rev Mol Cell Bio. 2000;1(1):11-21. doi: Doi 10.1038/35036035. PubMed PMID: WOS:000165765100012.
3. Borrus DS, Stettler MK, Grover CJ, Kalajian EJ, Gu J, Smith GDC, Del Negro CA. Inspiratory and sigh breathing rhythms depend on distinct cellular signalling mechanisms in the preBotzinger complex. J Physiol-London. 2024;602(5):809-34. doi: 10.1113/Jp285582. PubMed PMID: WOS:001161691600001.
4. Belote RL, Simon SM. Ca2+ transients in melanocyte dendrites and dendritic spine-like structures evoked by cell-to-cell signaling. J Cell Biol. 2020;219(1). doi: 10.1083/jcb.201902014. PubMed PMID: 31821412; PubMed Central PMCID: PMCPMC7039208.
5. Tyser RCV, Miranda AMA, Chen CM, Davidson SM, Srinivas S, Riley PR. Calcium handling precedes cardiac differentiation to initiate the first heartbeat. Elife. 2016;5. doi: ARTN e17113 10.7554/eLife.17113. PubMed PMID: WOS:000386050500001.
6. Jia BZ, Qi Y, Wong-Campos JD, Megason SG, Cohen AE. A bioelectrical phase transition patterns the first vertebrate heartbeats. Nature. 2023;622(7981):149-55. Epub 20230927. doi: 10.1038/s41586-023-06561-z. PubMed PMID: 37758945.
7. Donald L, Lakatta EG. What makes the sinoatrial node tick? A question not for the faint of heart. Philos Trans R Soc Lond B Biol Sci. 2023;378(1879):20220180. Epub 20230501. doi: 10.1098/rstb.2022.0180. PubMed PMID: 37122227; PubMed Central PMCID: PMCPMC10150214.

8. Lakatta EG, Maltsev VA, Vinogradova TM. A coupled SYSTEM of intracellular Ca2+ clocks and surface membrane voltage clocks controls the timekeeping mechanism of the heart's pacemaker. Circ Res. 2010;106(4):659-73. doi: 10.1161/CIRCRESAHA.109.206078. PubMed PMID: 20203315; PubMed Central PMCID: PMCPMC2837285.
9. Maltsev VA, Vinogradova TM, Stern MD, Lakatta EG. Letter to the editor: "Validating the requirement for beat-to-beat coupling of the Ca2+ clock and M clock in pacemaker cell normal automaticity". Am J Physiol Heart Circ Physiol. 2011;300(6):H2323-4; author reply H5-6. doi: 10.1152/ajpheart.00110.2011. PubMed PMID: 21632980; PubMed Central PMCID: PMCPMC3119099.
10. Vinogradova TM, Kobrinsky E, Lakatta EG. Dual Activation of Phosphodiesterases 3 and 4 Regulates Basal Spontaneous Beating Rate of Cardiac Pacemaker Cells: Role of Compartmentalization? Front Physiol. 2018;9:1301. Epub 20181009. doi: 10.3389/fphys.2018.01301. PubMed PMID: 30356755; PubMed Central PMCID: PMCPMC6189467.
11. Vinogradova TM, Lakatta EG. Regulation of basal and reserve cardiac pacemaker function by interactions of cAMP-mediated PKA-dependent Ca2+ cycling with surface membrane channels. J Mol Cell Cardiol. 2009;47(4):456-74. Epub 20090630. doi: 10.1016/j.yjmcc.2009.06.014. PubMed PMID: 19573534; PubMed Central PMCID: PMCPMC2757791.
12. Vinogradova TM, Lakatta EG. Dual Activation of Phosphodiesterase 3 and 4 Regulates Basal Cardiac Pacemaker Function and Beyond. Int J Mol Sci. 2021;22(16). Epub 20210805. doi: 10.3390/ijms22168414. PubMed PMID: 34445119; PubMed Central PMCID: PMCPMC8395138.
13. Vinogradova TM, Maltsev VA, Bogdanov KY, Lyashkov AE, Lakatta EG. Rhythmic Ca oscillations drive sinoatrial nodal cell pacemaker function to make the heart tick. Ann Ny Acad Sci. 2005;1047:138-56. doi: 10.1196/annals.1341.013. PubMed PMID: WOS:000231874400013.
14. Vinogradova TM, Tagirova Sirenko S, Lakatta EG. Unique Ca(2+)-Cycling Protein Abundance and Regulation Sustains Local Ca(2+) Releases and Spontaneous Firing of Rabbit Sinoatrial Node Cells. Int J Mol Sci. 2018;19(8). Epub 2018/07/26. doi: 10.3390/ijms19082173. PubMed PMID: 30044420; PubMed Central PMCID: PMCPMC6121616.
15. Maltsev AV, Maltsev VA, Mikheev M, Maltseva LA, Sirenko SG, Lakatta EG, Stern MD. Synchronization of stochastic Ca(2)(+) release units creates a rhythmic Ca(2)(+) clock in cardiac pacemaker cells. Biophys J. 2011;100(2):271-83. Epub 2011/01/20. doi: 10.1016/j.bpj.2010.11.081. PubMed PMID: 21244823; PubMed Central PMCID: PMCPMC3021664.
16. Bychkov R, Juhaszova M, Tsutsui K, Coletta C, Stern MD, Maltsev VA, Lakatta EG. Synchronized Cardiac Impulses Emerge From Heterogeneous Local Calcium Signals Within and Among Cells of Pacemaker Tissue. Jacc-Clin Electrophy. 2020;6(8):907-31. doi: 10.1016/j.jacep.2020.06.022. PubMed PMID: WOS:000602739500001.
17. Efimov IR, Nikolski VP, Salama G. Optical imaging of the heart. Circ Res. 2004;95(1):21-33. doi: 10.1161/01.RES.0000130529.18016.35. PubMed PMID: 15242982.
18. Lang D, Petrov V, Lou Q, Osipov G, Efimov IR. Spatiotemporal control of heart rate in a rabbit heart. Journal of electrocardiology. 2011;44(6):626-34. PubMed PMID: 21937057.

19. Li N, Hansen BJ, Csepe TA, Zhao J, Ignozzi AJ, Sul LV, Zakharkin SO, Kalyanasundaram A, Davis JP, Biesiadecki BJ, Kilic A, Janssen PML, Mohler PJ, Weiss R, Hummel JD, Fedorov VV. Redundant and diverse intranodal pacemakers and conduction pathways protect the human sinoatrial node from failure. Sci Transl Med. 2017;9(400). doi: 10.1126/scitranslmed.aam5607. PubMed PMID: 28747516; PubMed Central PMCID: PMCPMC5775890.
20. Bychkov R, Juhaszova M, Calvo-Rubio Barrera M, Donald LAH, Coletta C, Shumaker C, Moorman K, Sirenko ST, Maltsev AV, Sollott SJ, Lakatta EG. The Heart's Pacemaker Mimics Brain Cytoarchitecture and Function: Novel Interstitial Cells Expose Complexity of the SAN. JACC Clin Electrophysiol. 2022;8(10):1191-215. Epub 2022/10/02. doi: 10.1016/j.jacep.2022.07.003. PubMed PMID: 36182566; PubMed Central PMCID: PMCPMC9665104.
21. Faisal AA, Selen LP, Wolpert DM. Noise in the nervous system. Nat Rev Neurosci. 2008;9(4):292-303. doi: 10.1038/nrn2258. PubMed PMID: 18319728; PubMed Central PMCID: PMCPMC2631351.
22. Guo DQ, Perc M, Liu TJ, Yao DZ. Functional importance of noise in neuronal information processing. Epl-Europhys Lett. 2018;124(5). doi: Artn 50001 10.1209/0295-5075/124/50001. PubMed PMID: WOS:000454552700001.
23. Liu HX, Lu LL, Zhu Y, Wei ZC, Yi M. Stochastic resonance: The response to envelope modulation signal for neural networks with different topologies. Physica A. 2022;607. doi: ARTN 128177 10.1016/j.physa.2022.128177. PubMed PMID: WOS:000876411900009.
24. Sporns O, Zwi JD. The small world of the cerebral cortex. Neuroinformatics. 2004;2(2):145-62. doi: Doi 10.1385/Ni:2:2:145. PubMed PMID: WOS:000223582200003.
25. Watts DJ, Strogatz SH. Collective dynamics of 'small-world' networks. Nature. 1998;393(6684):440-2. doi: Doi 10.1038/30918. PubMed PMID: WOS:000074020000035.
26. Qu ZL, Garfinkel A, Weiss JN, Nivala M. Multi-scale modeling in biology: How to bridge the gaps between scales? Prog Biophys Mol Bio. 2011;107(1):21-31. doi: 10.1016/j.pbiomolbio.2011.06.004. PubMed PMID: WOS:000296544000004.
27. Bogdanov KY, Maltsev VA, Vinogradova TM, Lyashkov AE, Spurgeon HA, Stern MD, Lakatta EG. Membrane potential fluctuations resulting from submembrane Ca^{2+} releases in rabbit sinoatrial nodal cells impart an exponential phase to the late diastolic depolarization that controls their chronotropic state. Circ Res. 2006;99(9):979-87. PubMed PMID: 17008599.
28. Lyashkov AE, Behar J, Lakatta EG, Yaniv Y, Maltsev VA. Positive Feedback Mechanisms among Local Ca Releases, NCX, and I Ignite Pacemaker Action Potentials (vol 114, pg 1176, 2018). Biophysical Journal. 2018;114(8):2024-. doi: 10.1016/j.bpj.2018.03.024. PubMed PMID: WOS:000432692800025.
29. Guarina L, Moghbel AN, Pourhosseinzadeh MS, Cudmore RH, Sato D, Clancy CE, Santana LF. Biological noise is a key determinant of the reproducibility and adaptability of cardiac pacemaking and EC coupling. J Gen Physiol. 2022;154(9). doi: ARTN e202012613 10.1085/jgp.202012613. PubMed PMID: WOS:000860454700001.
30. Xiong LI, Garfinkel A. Are physiological oscillations physiological? J Physiol. 2023. Epub 20230825. doi: 10.1113/JP285015. PubMed PMID: 37622389.
31. Abreu T, Silva PA, Sancho F, Temperville A. Analytical approximate wave form for asymmetric waves. Coast Eng. 2010;57(7):656-67. doi: 10.1016/j.coastaleng.2010.02.005. PubMed PMID: WOS:000278342200003.

32. Mateo C, Talavera JA. Short-time Fourier transform with the window size fixed in the frequency domain. Digital Signal Processing. 2018;77:13-21.
33. Ramsay JO, Silverman BW. Functional data analysis. New York: Springer; 1997. xiv, 310 p. p.
34. Lee SH, Lim JS, Kim JK, Yang J, Lee Y. Classification of normal and epileptic seizure EEG signals using wavelet transform, phase-space reconstruction, and Euclidean distance. Comput Methods Programs Biomed. 2014;116(1):10-25. Epub 20140430. doi: 10.1016/j.cmpb.2014.04.012. PubMed PMID: 24837641.
35. Jalife J. Mutual Entrainment and Electrical Coupling as Mechanisms for Synchronous Firing of Rabbit Sino-Atrial Pace-Maker Cells. J Physiol-London. 1984;356(Nov):221-43. doi: DOI 10.1113/jphysiol.1984.sp015461. PubMed PMID: WOS:A1984TT18900014.
36. Michaels DC, Chialvo DR, Matyas EP, Jalife J. Chaotic activity in a mathematical model of the vagally driven sinoatrial node. Circ Res. 1989;65(5):1350-60. doi: 10.1161/01.res.65.5.1350. PubMed PMID: 2805248.
37. Packard NH, Crutchfield JP, Farmer JD, Shaw RS. Geometry from a Time-Series. Phys Rev Lett. 1980;45(9):712-6. doi: DOI 10.1103/PhysRevLett.45.712. PubMed PMID: WOS:A1980KE58800012.
38. Efimov IR, Fedorov VV, Joung B, Lin SF. Mapping cardiac pacemaker circuits: methodological puzzles of the sinoatrial node optical mapping. Circ Res. 2010;106(2):255-71. doi: 10.1161/CIRCRESAHA.109.209841. PubMed PMID: 20133911; PubMed Central PMCID: PMCPMC2818830.
39. Fedorov VV, Glukhov AV, Chang R. Conduction barriers and pathways of the sinoatrial pacemaker complex: their role in normal rhythm and atrial arrhythmias. Am J Physiol Heart Circ Physiol. 2012;302(9):H1773-83. Epub 20120120. doi: 10.1152/ajpheart.00892.2011. PubMed PMID: 22268110.
40. Bouman LN, Jongsma HJ. Structure and function of the sino-atrial node: a review. Eur Heart J. 1986;7(2):94-104. doi: 10.1093/oxfordjournals.eurheartj.a062047. PubMed PMID: 2422036.
41. Verheijck EE, van Kempen MJA, Veereschild M, Lurvink J, Jongsma HJ, Bouman LN. Electrophysiological features of the mouse sinoatrial node in relation to connexin distribution. Cardiovasc Res. 2001;52(1):40-50. doi: Doi 10.1016/S0008-6363(01)00364-9. PubMed PMID: WOS:000171953400006.
42. Chen WT, Chen YC, Lu YY, Kao YH, Huang JH, Lin YK, Chen SA, Chen YJ. Apamin modulates electrophysiological characteristics of the pulmonary vein and the Sinoatrial Node. Eur J Clin Invest. 2013;43(9):957-63. doi: 10.1111/eci.12125. PubMed PMID: WOS:000323152800008.
43. Huang JH. Apamin modulates electrophysiological characteristics of the pulmonary vein and the Sinoatrial Node (vol 43, pg 957, 2013). Eur J Clin Invest. 2016;46(7):675-. doi: 10.1111/eci.12645. PubMed PMID: WOS:000379669500008.
44. Torrente AG, Zhang R, Wang HD, Zaini A, Kim B, Yue X, Philipson KD, Goldhaber JI. Contribution of small conductance K channels to sinoatrial node pacemaker activity: insights from atrial-specific Na/Ca exchange knockout mice. J Physiol-London. 2017;595(12):3847-65. doi: 10.1113/Jp274249. PubMed PMID: WOS:000404654500015.
45. Mori S, Shivkumar K. Atlas of Cardiac Anatomy Cardiotext; 2022.
46. Bachmann G. The Inter-Auricular Time Interval. Am J Physiol. 1916;41(3):309-20. doi: DOI 10.1152/ajplegacy.1916.41.3.309. PubMed PMID: WOS:000207509400004.

47. Chhabra L, Devadoss R, Chaubey VK, Spodick DH. Interatrial Block in the Modern Era. Curr Cardiol Rev. 2014;10(3):181-9. doi: 10.2174/1573403x10666140514101748. PubMed PMID: WOS:000212837200003.
48. Nitta T, Ishii Y, Miyagi Y, Ohmori H, Sakamoto S, Tanaka S. Concurrent multiple left atrial focal activations with fibrillatory conduction and right atrial focal or reentrant activation as the mechanism in atrial fibrillation. J Thorac Cardiov Sur. 2004;127(3):770-8. doi: 10.1016/j.jtcvs.2003.05.001. PubMed PMID: WOS:000220115400025.
49. Swartz MF, Fink GW, Lutz CJ, Taffet SM, Berenfeld O, Vikstrom KL, Kasprowicz K, Bhatta L, Puskas F, Kalifa J, Jalife J. Left versus right atrial difference in dominant frequency, K channel transcripts, and fibrosis in patients developing atrial fibrillation after cardiac surgery. Heart Rhythm. 2009;6(10):1415-22. doi: 10.1016/j.hrthm.2009.06.018. PubMed PMID: WOS:000270502700003.
50. Allessie MA, Bonke FI. Direct demonstration of sinus node reentry in the rabbit heart. Circ Res. 1979;44(4):557-68. doi: 10.1161/01.res.44.4.557. PubMed PMID: 428051.
51. Allessie MA, Bonke FIM, Kirchhof CJHJ. Electrotonic Influence of Atrial Myocardium on Sinus Node Function in the Rabbit. J Physiol-London. 1985;366(Sep):P36-P. PubMed PMID: WOS:A1985ARF5900060.
52. Fedorov VV, Chang R, Glukhov AV, Kostecki G, Janks D, Schuessler RB, Efimov IR. Complex Interactions Between the Sinoatrial Node and Atrium During Reentrant Arrhythmias in the Canine Heart. Circulation. 2010;122(8):782-U79. doi: 10.1161/Circulationaha.109.935288. PubMed PMID: WOS:000281193100005.
53. Glukhov AV, Fedorov VV, Kalish PW, Ravikumar VK, Lou Q, Janks D, Schuessler RB, Moazami N, Efimov IR. Conduction Remodeling in Human End-Stage Nonischemic Left Ventricular Cardiomyopathy. Circulation. 2012;125(15):1835-+. doi: 10.1161/Circulationaha.111.047274. PubMed PMID: WOS:000302957800011.
54. Lang D, Glukhov AV. High-resolution Optical Mapping of the Mouse Sino-atrial Node. J Vis Exp. 2016;(118). Epub 20161202. doi: 10.3791/54773. PubMed PMID: 28060289; PubMed Central PMCID: PMCPMC5226351.
55. Yang DM, Morrell CH, Lyashkov AE, Tagirova S, Zahanich I, Yaniv Y, Vinogradova TM, Ziman BD, Maltsev VA, Lakatta EG. Ca
and Membrane Potential Transitions During Action Potentials Are Self-Similar to Each Other and to Variability of AP Firing Intervals Across the Broad Physiologic Range of AP Intervals During Autonomic Receptor Stimulation. Frontiers in Physiology. 2021;12. doi: ARTN 612770 10.3389/fphys.2021.612770. PubMed PMID: WOS:000698451200001.
56. Wilson EO. Consilience : the unity of knowledge. 1st ed. New York: Knopf : Distributed by Random House; 1998. 332 p. p.

Figure Legends:

Figure 1. Integrated time-dependent changes of LCO's dynamics create discrete global Ca2+ impulses. (A) Spontaneous, rhythmic global SAN Ca2+ impulses, i.e. Ca2+ transients (CaT) superimposed on local Ca2+ oscillations (LCOs) of 50 areas of interest (ROIs) during 2.7 seconds recording. (**B)** regional Ca2+ signals initiation time (acrophase) during about 180 ms of a spontaneous impulse formation. (**C) A**crophases of each ROI mapped on SAN virtual space. See also

Movie 1.pptx. **(D)**The average range (mean, median, range with 1.5IQR) of acrophase for each of the four color-coded clusters. **(E)** Ca2+ dynamics of 50 ROIs that form the global SAN Ca2+ impulse at each sampling point during one cycle. See also Movie 2.pptx.

Figure 2. **Kinetic analysis of the dynamic of the integrated (global) Ca2+ impulses, i.e. Ca2+ transients (CaTs) in SAN tissue. (A)** An example of CaTs waveforms (F/F0) during two cycles (upper panel, i) and its first (dCaT/dt, i,), second (d2CaT/dt2, iii), and third derivatives (d3CaT/dt3, iv) are shown in lower panels. **(B)** Normalized waveform of the first CaT impulse in panel A. The peaks of the 1st, 2d and 3d derivatives occurred at 73.5 ms and 68.3 ms and 64.9 ms and at times at which the amplitude of the CaT reached 45%, 11.8% and 4% of the maximum amplitude respectively (panel B). **(C)** The slow phase of normalized CaT in panel B (that occurred between ~50-65ms during impulse formation) was modeled using a tangent line (red line) and a linear fit (black line). The inflection point is also marked by a green dotted line in panel B. The earliest inflection point occurred at 64.9 ms, coinciding with the peak of the third derivative. At this time, the tangent slope was 0.81, and the integrated global Ca2+ signal amplitude had reached 4.02% of its maximum peak. A linear model fitted to the Ca2+ signal during the interval from 50 to 65 ms showed strong local linearity (approximately 12 ms) with a slope of 0.38 (a.u./ms, r = 1.0).

Figure 3. Analyses of dynamics of local Ca^{2+} oscillations and global Ca^{2+} transients (CaT) in SAN tissue. (A) The global SAN CaT (F/Fo), depicted by the solid black line, is overlaid on the average LCO impulse (F/Fo) for each of the four designated color-coded regions, as shown in the top panel. The middle and lower panels illustrate the first and second derivatives, respectively Note that the amplitude of the Ca2+ signal in the red regional cluster was lower than that observed in the other three clusters. **(B)** The normalized amplitudes of the Ca2+ signals from panel A (top), scaled from 0 to 100. The first and second derivatives were derived from these normalized Ca2+ signals, as displayed in the lower panels. (C) The instantaneous rate of change (IROC) of the red cluster in comparison to the other clusters and the global CaT presented in panel B. The relative IROC for the red color-coded cluster was determined by subtracting the first derivatives of the yellow, green, and blue clusters, as well as the global CaT, from the first derivative of the red cluster at each time point. Note that the increase in the IROC for the red color-coded cluster during the initiation of the impulse (pre-foot and foot stages, approximately 15-65 milliseconds during impulse formation) occurred earlier and exhibited a greater magnitude than that of the other clusters, which demonstrated minimal variation during this timeframe.

Figure 5. Stability of LCOs among SAN spatial domains. (A) The normalized amplitude of the sinoatrial node (SAN) calcium (Ca2+) signal across four distinct color-coded clusters over a duration of 300 milliseconds (encompassing two impulse formations). (**B**) Velocity change, represented as the first derivative of the Ca2+ signal for the aforementioned clusters in panel A. The circles indicate fixed points where the velocity is zero; closed circles denote stable fixed points, while open circles represent unstable fixed points. **(C)** Fixed and unstable points of the four color-coded clusters during the initial cycle, as depicted in Panel A, are presented with increased resolution. If a fixed point is stable, the velocity (dCa2+/dt) of the points in its vicinity will be *negative* (dCa2+/dt < 0), i.e. the fixed point is considered to be a 'sink' and the signal is moving *toward* equilibrium. If the velocity of points near the fixed point is positive (dCa2+/dt > 0), this designates it as an unstable fixed point, or a 'source', from which the signal diverges exponentially from equilibrium.

Figure 6. Frequency components of the total energy expended throughout SAN tissue. (A) The upper panel illustrates the superimposed waveforms of the Ca2+ signal from four distinct, color-

coded clusters, normalized on a scale from 0 to 100. The lower panels present the decomposition of the Ca2+ signal into its intrinsic mode functions (IMF). **(B)** The instantaneous frequencies corresponding to the predominant power derived from IMFs 2 and 3 are displayed in panel A. The complete frequency ranges are detailed in Fig. S2.

Figure 7. STFT-FD (Short-Time Fourier Transform with window size fixed in the frequency domain) of four regional color-coded signals. Time-frequency representation of the red **(A),** yellow **(B),** green **(C),** and blue color-coded cluster **(D)** between 0.3-0.75 sec in time series. The bar graph represents the frequency power (Amp). The low-frequency area is illustrated by oval 1 and the high-frequency area by oval 2.

Figure 8. Functional data analysis (FDA) of energy transfer deduced from the time-dependent kinetic changes of Ca^{2+} dynamics of four color-coded clusters (A) The color-coded map illustrates the functional clusters of the SAN. **(B)** The averaged normalized Ca2+ impulses (upper panel) for four distinct color-coded areas depicted in panel A, along with their first (middle panel) and second (lower panel) derivatives, are presented during a 500 ms duration of impulse formation. **(C)** Phase-plane diagrams displaying acceleration (second derivative) and velocity (first derivative) from panel B are provided over a 500 ms period of impulse formation, encompassing three cycles. **(D)** The initial phase-plane diagram of the red, yellow, green, and blue clusters displayed in panel C is presented, with variations indicated by solid and dashed black lines and arrows. **(E)** A magnified view of the low energy state (pre-foot) from panel D between approximately 12 and 46 ms during the impulse formation is shown. **(F)** A detailed depiction of the foot formation state from panel D is presented, covering the time interval from approximately 46.1 ms to 65 ms during impulse formation. See also Movie 3.pptx. When *both* velocity and acceleration are *zero*, a system is in true equilibrium and no energy is being transferred. When *either* acceleration or velocity are *non-zero*, the system is in motion and energy is being transferred from potential to kinetic energy for a given purpose. When either acceleration or velocity is *negative*, kinetic energy is being transferred back to potential energy and vs versa. If the potential and kinetic energies within the FDA function form a perfect circle (acceleration and velocity simultaneously crossing at 0:0) the system would achieve a true equilibrium.

Figure 9. Clustering of spatio-temporal correlations of SAN local Ca2+ oscillation (LCO) dynamic during impulse formation. **(A)** Regions of interest (ROIs) in the SAN that reached peak values first are represented on the SAN space map using colors red, yellow, green, and blue respectively. **(B)** The normalized LCO of 50 ROIs during the initial 350 ms of impulse formation. Each 15 ms segment for impulses 1 and 2 is labeled with numerical values (0-7) on the vertical axis. The global Ca2+ signal waveform (CaT) is shown in black. **(C-K)** Pearson correlation analysis is performed using a continuous window rolling approach (~15 ms). Fruchterman–Reingold force-directed network plots of correlation coefficients ($r \geq 0.99$) for LCO dynamics in each segment from panel A are presented side-by-side in panels C-K. The network for impulse 1 is indicated by blue circles, while the network for impulse 2 is represented by green circles. Lines connecting ROIs in the network reflect the strength of their correlations. Full correlation patterns for both correlated and uncorrelated ROIs are detailed in Figs. S3-S4.

Figure 10. The correlation matrix of the kinetics of average Ca2+ dynamics across four distinct SAN color-coded functional clusters, along with their interactions with the global SAN CaT during the entire 2.7-second time-series recordings. The upper triangular portion of the matrix

highlights statistically significant correlations, while the lower triangular section provides the corresponding correlation coefficients. Positive correlations are denoted by red circles, whereas negative correlations are indicated by a blue circle. The size of each circle is proportional to the strength of the correlation, and the vertical color bar serves as a reference for the correlation coefficients.

Figure 11. Functional data analysis (FDA) of integrated (global) Ca2+ dynamics, examining the relationship between acceleration and velocity in concurrence with LCO cluster formation across two cycles. **(A)** FDA phase-plane diagrams of the global CaT acceleration (the second derivative) plotted against velocity (the first derivative) of the 1st global SAN CaT in Figure 8B. The analysis is segmented into three distinct sections based on the shift along the axes, represented in panels B through D. **(B)** A rotor-like trajectory is observed during the first impulse within the initial 0-63 milliseconds of impulse formation is compared with the corresponding cluster formation occurring over a similar timeframe, delineated in panels E through G. Additionally, phase-plane diagrams depicting the acceleration versus velocity of the integrated (global) CaT for all 19 impulses are presented in Figure S5 and Movie S3.pptx.

Figure 12. Dynamic of small-world properties of the integrated global SAN Ca^{2+} impulse throughout time-series. (A) The top panel shows the normalized integrated (global) Ca^{2+} signal (black color) and small-worldness σ (orange color) over time of 1000ms. Red dots mark peaks of the global Ca^{2+} impulses, while green crosses mark σ peaks. Numbers 1-6 highlight notable σ peaks. **(B)** The bottom panel displays network graphs for six consecutive cycles, with nodes colored according to their functional cluster (red, yellow, green, blue). Each graph represents the network configuration at the time of peak σ for that cycle. The σ values are noted for each cycle in the center of each network graph.

Figure 13. Manifold phase space reconstruction of Ca^{2+} amplitude of four color-codded clusters during entire time-series recording (2.7 sec) in 3D. (A) The original amplitude (F/F0) of the average red, green, and blue LCO signals plotted against each other in 3D through time-series (2.7 sec). **(B-D)** reconstructed phase spaces of panel **A.** The optimal time delay τ (tau) was determined based on the average mutual Information (AMI) and the autocorrelation function (ACF). We used τ of 15,3 ms, 23.9 ms and 15.3 ms for red, green, and blue clusters respectively. The embedding dimension *(d)* was determined by Cao's E1(d) and the E2(d) functions (see methods) to embed the original data (panel A) in an M-dimensional manifold. The first 3 dimensions were chosen from a total of 8 (red), 6 (green), and 8 (blue) to fit the 3D plot. The manifold of the yellow LCO signal (not shown) was similar to that of green.

Figure 14. Peak-to-peak variability within SAN tissue during 2.7 seconds. (A) Peak-to-peak interval variability of the Ca^{2+} dynamic within each of four color-coded clusters during 2.7-second recordings. **(B)** Average intervals variability of four color-coded functional clusters (right axes) and their standard deviation (SD, left axes). Broken lines show a mean interval and SD of the integrated (global) SAN CaT.

Figure 15. Visualization of the direction of rotation and time-delayed trajectories of reginal and global Ca^{2+} signals. (A) It depicts the spatially averaged amplitude of the Ca2+ signal across four color-coded clusters over a period of 500 milliseconds, covering three cycles of impulse formation. **(B)** The orbit plots generated from the Ca2+ signals presented in panel A are displayed in both unlagged and lagged formats (+7ms). **(C)** Orbit plots representing the Ca2+ signals during a shorter duration of 180 milliseconds of impulse formation in panel A. **(D)** A magnified view of the orbit plots from panel C focuses on the interval from 0 to 64.5 milliseconds of impulse formation

(pre-foot and foot). **(E)** The integrated (global) amplitude of the Ca2+ signal (CaT) is recorded over a longer time-series of 2.7 seconds. **(F)** Orbit plots derived from the integrated (global) CaT in panel E are presented in both unlagged and lagged formats (+7ms). Examples of orbit plots for individual Regions of Interest (ROIs) from each of the four color-coded clusters can be found in Fig. S6.

Figure 16. Positive Lyapunov exponent quantifies the intermediate level of chaos in the global SAN Ca^{2+} signal. **(A)** Lorenz attractor, a classic example of deterministic chaos behavior ($\lambda = 0.146$); **(B)** The original integrated SAN Ca^{2+} signal ($\lambda = 0.082$). **(C)** Noisy sinusoidal wave, representing a stochastic system ($\lambda \approx 0.0001$); and **(**The reconstruction parameters included: embedding dimension = 2, lag = 1, minimum time separation = 4, tau = 1, and minimum neighbors = 10.

Figure 17. SAN Ca^{2+} dynamics of the four color-coded regional clusters relative to deduced SAN action potential (AP) and atrial AP. (A) Atrial action potential (AP, black line), measured simultaneously with SAN CaT via a sharp electrode as a time reference point, superimposed on Ca^{2+} dynamic of four color-coded clusters (color lines). (B) Deduced SAN action potential (AP, dotted line) superimposed on Ca^{2+} dynamic of four color-coded clusters (solid color lines).

1176

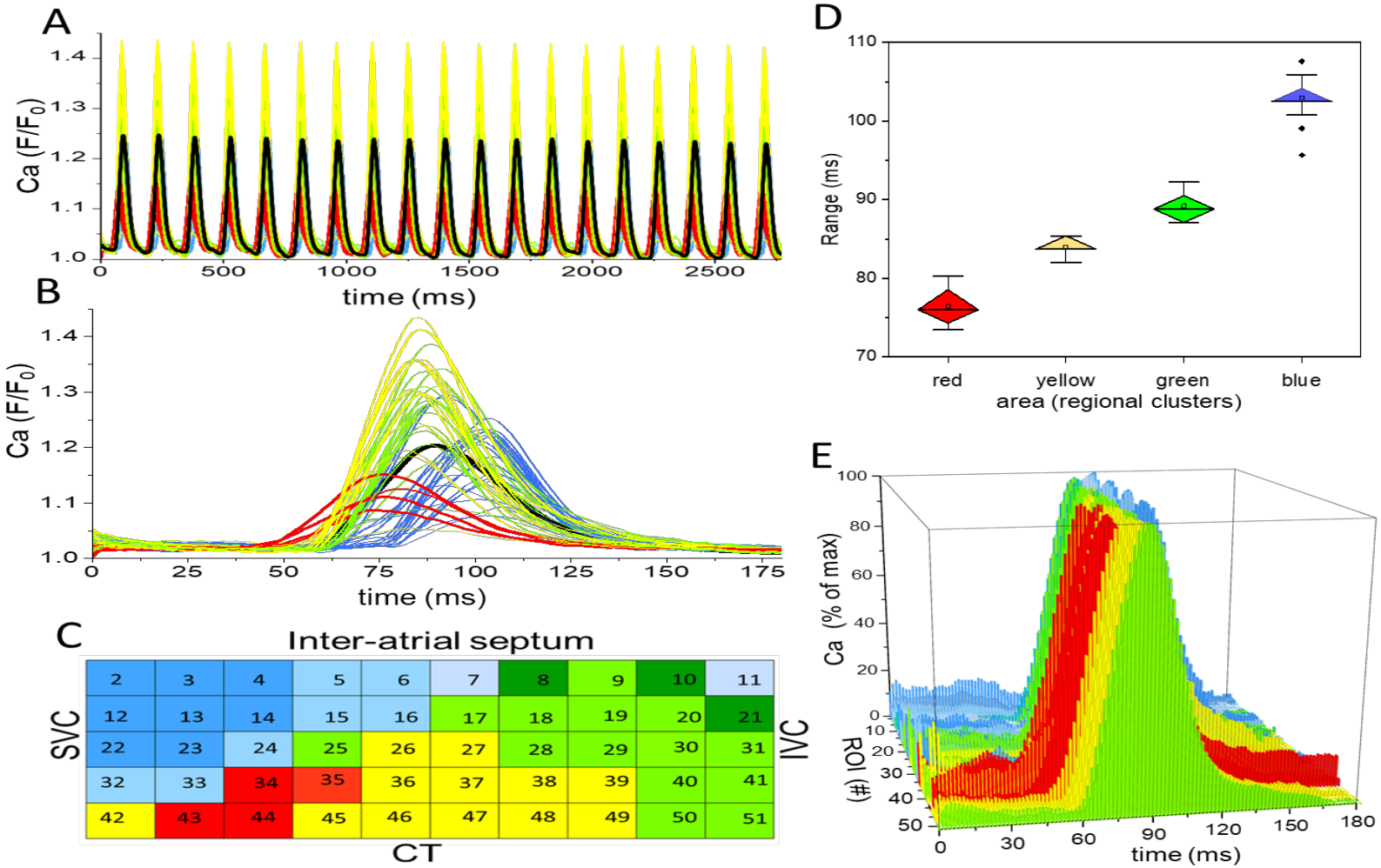

1177

1178 Figure 1.

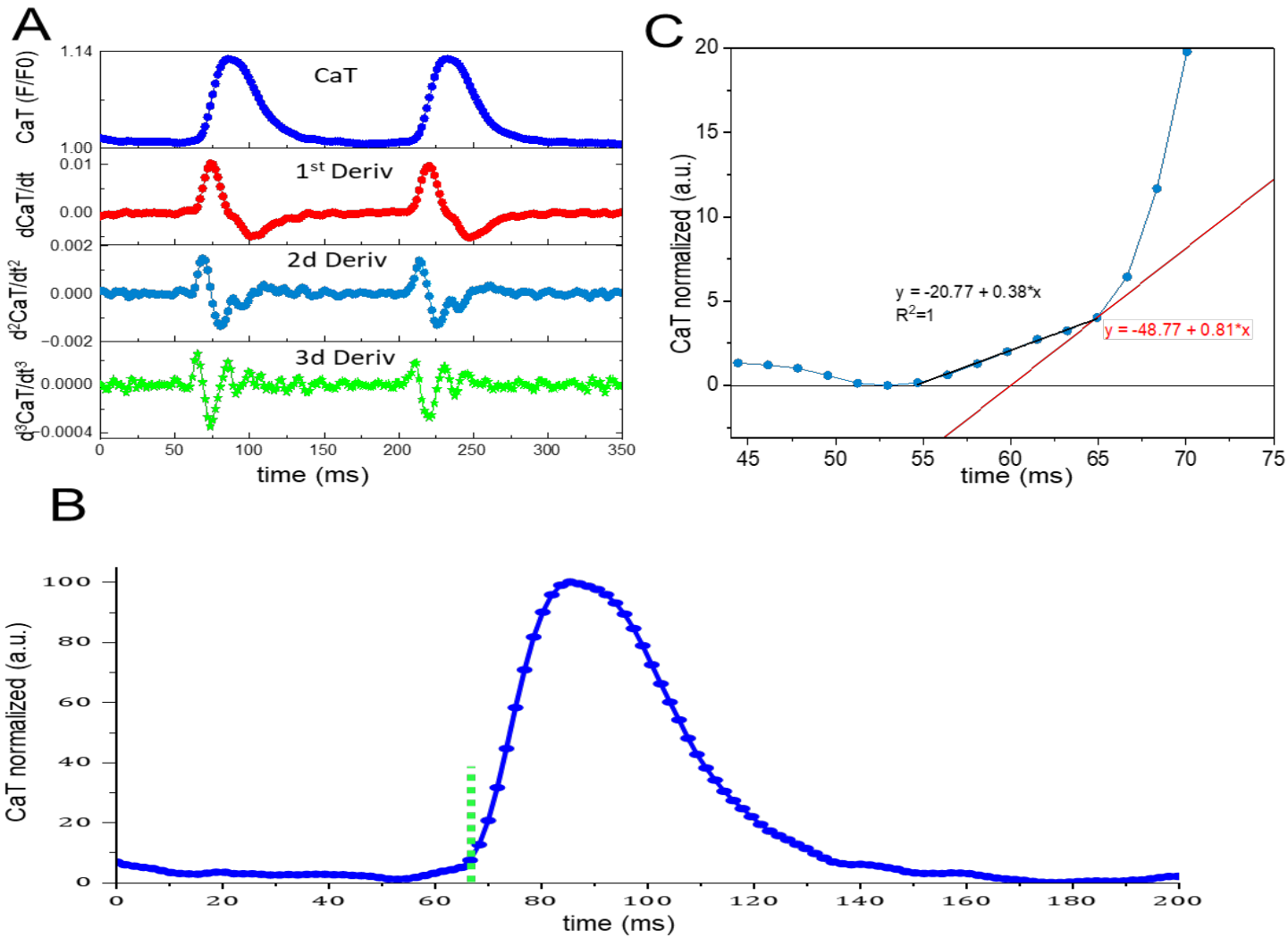
A
CaT (F/F0)
1.14
1.00
CaT
dCaT/dt
0.01
0.00
1st Deriv
d2CaT/dt2
0.002
0.000
−0.002
2d Deriv
d3CaT/dt3
0.0000
−0.0004
3d Deriv
0
50
100
150
200
250
300
350
time (ms)
C
CaT normalized (a.u.)
20
15
10
5
0
y = -20.77 + 0.38*x
R2=1
y = -48.77 + 0.81*x
45
50
55
60
65
70
75
time (ms)
B
CaT normalized (a.u.)
100
80
60
40
20
0
0
20
40
60
80
100
120
140
160
180
200
time (ms)

Figure 2.

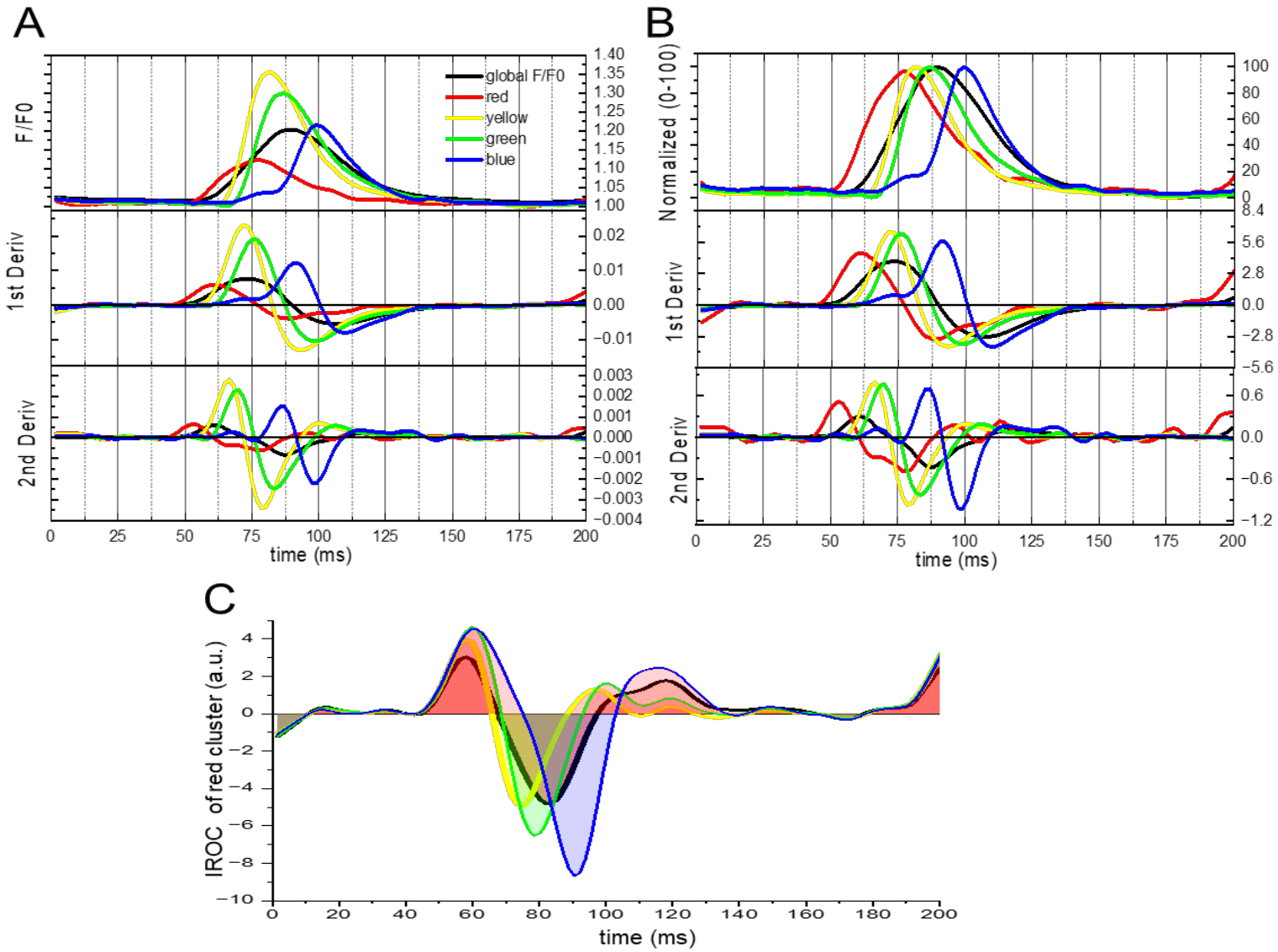
A
B
C
F/F0
1st Deriv
2nd Deriv
Normalized (0-100)
global F/F0
red
yellow
green
blue
time (ms)
IROC of red cluster (a.u.)

Figure 3.

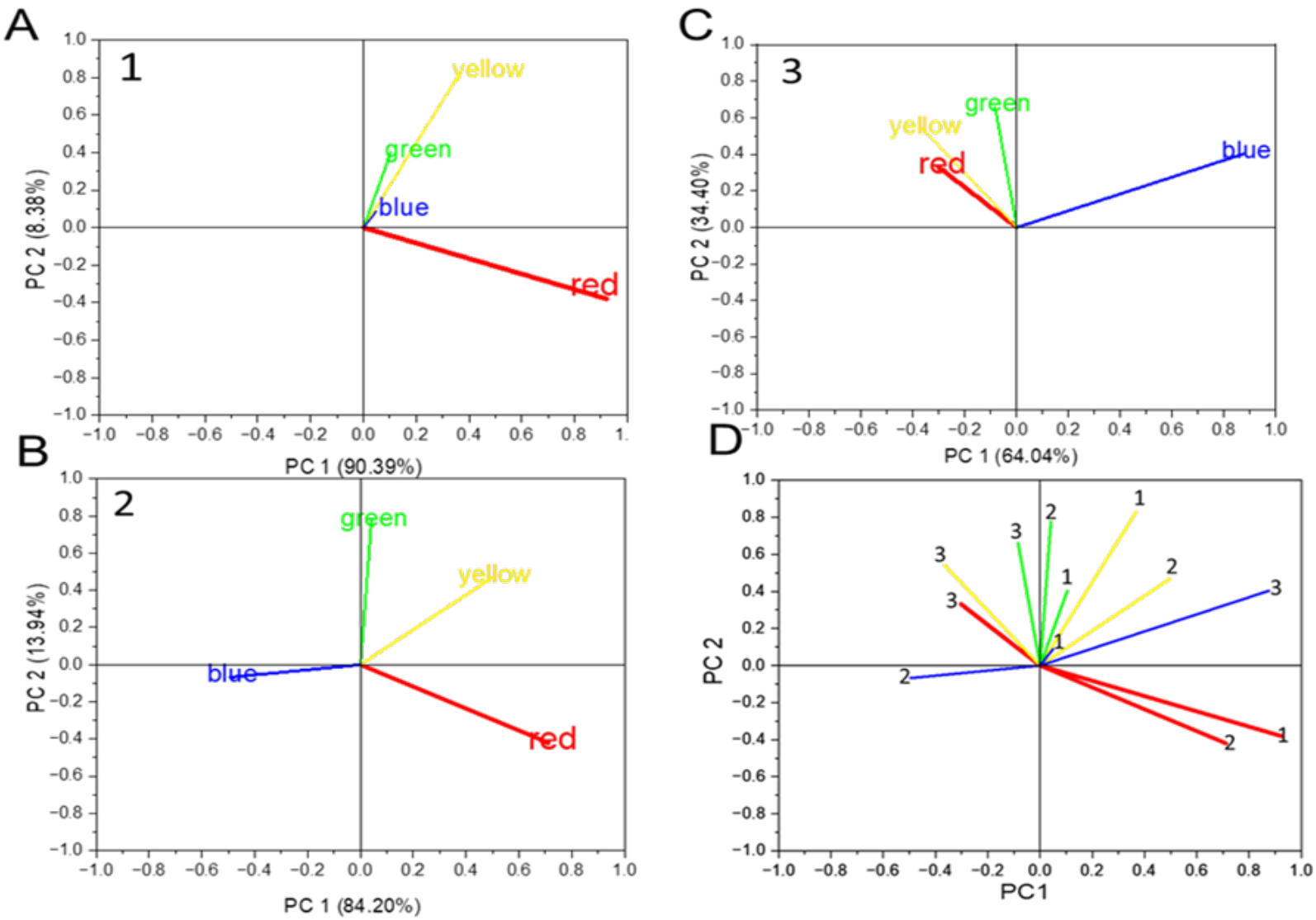
A
1
yellow
green
blue
red
PC 2 (8.38%)
PC 1 (90.39%)
B
2
green
yellow
blue
red
PC 2 (13.94%)
PC 1 (84.20%)
C
3
green
yellow
red
blue
PC 2 (34.40%)
PC 1 (64.04%)
D
PC 2
PC1

Figure 4.

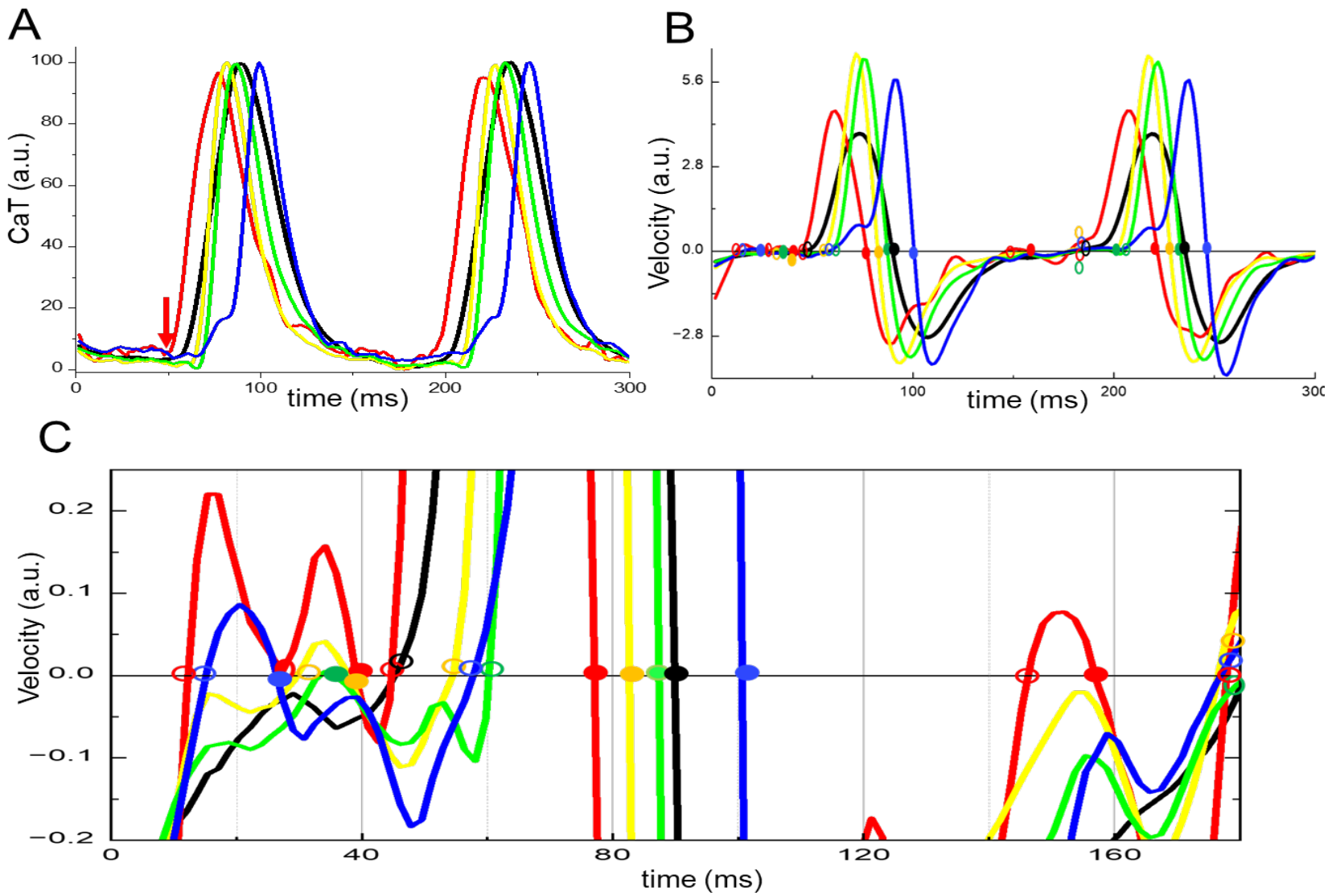
A
CaT (a.u.)
100
80
60
40
20
0
0
100
200
300
time (ms)
B
Velocity (a.u.)
5.6
2.8
0.0
−2.8
0
100
200
300
time (ms)
C
Velocity (a.u.)
0.2
0.1
0.0
−0.1
−0.2
0
40
80
120
160
time (ms)

Figure 5.

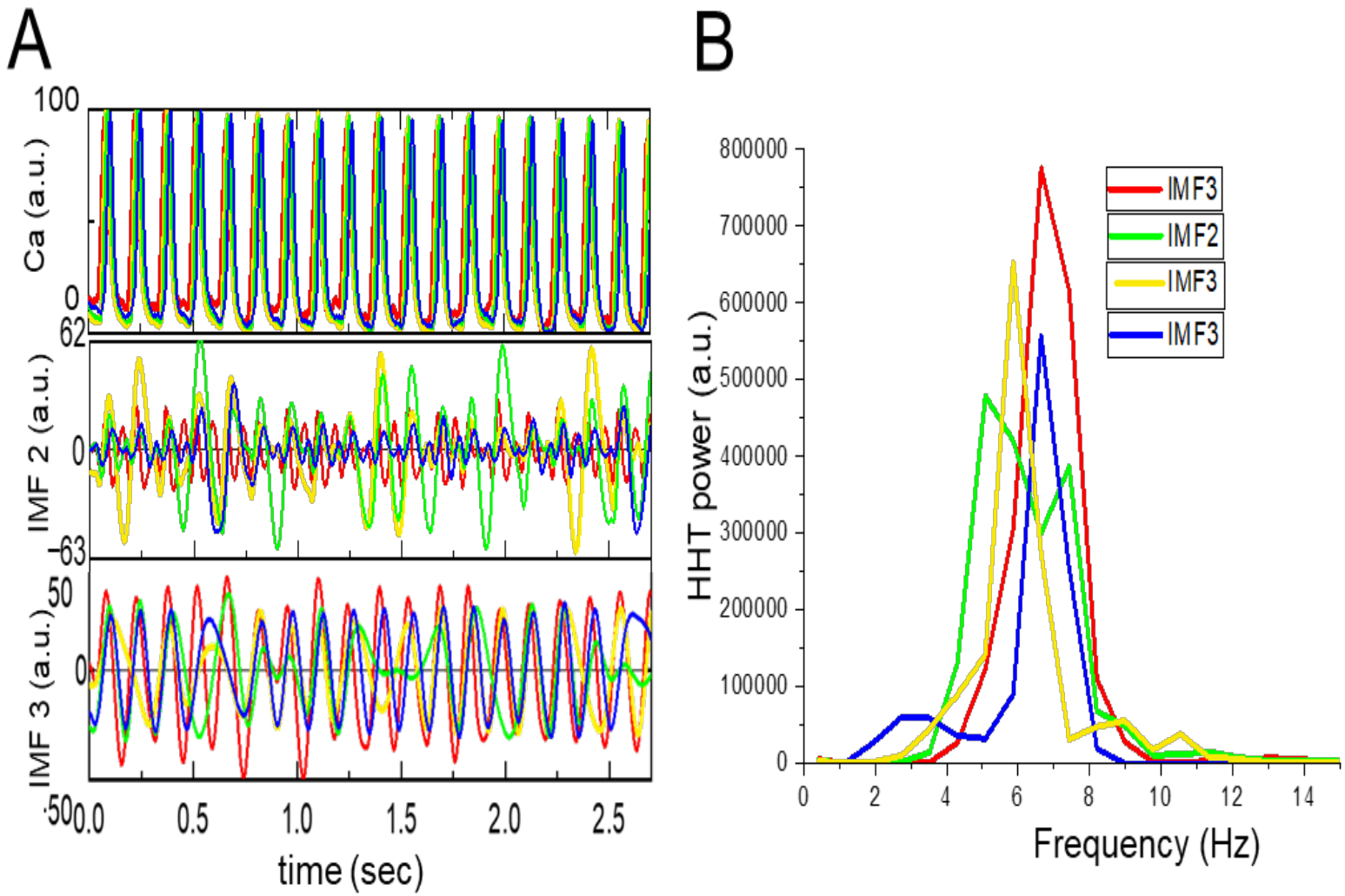
A
B
Ca (a.u.)
IMF 2 (a.u.)
IMF 3 (a.u.)
time (sec)
HHT power (a.u.)
Frequency (Hz)
IMF3
IMF2
IMF3
IMF3

Figure 6.

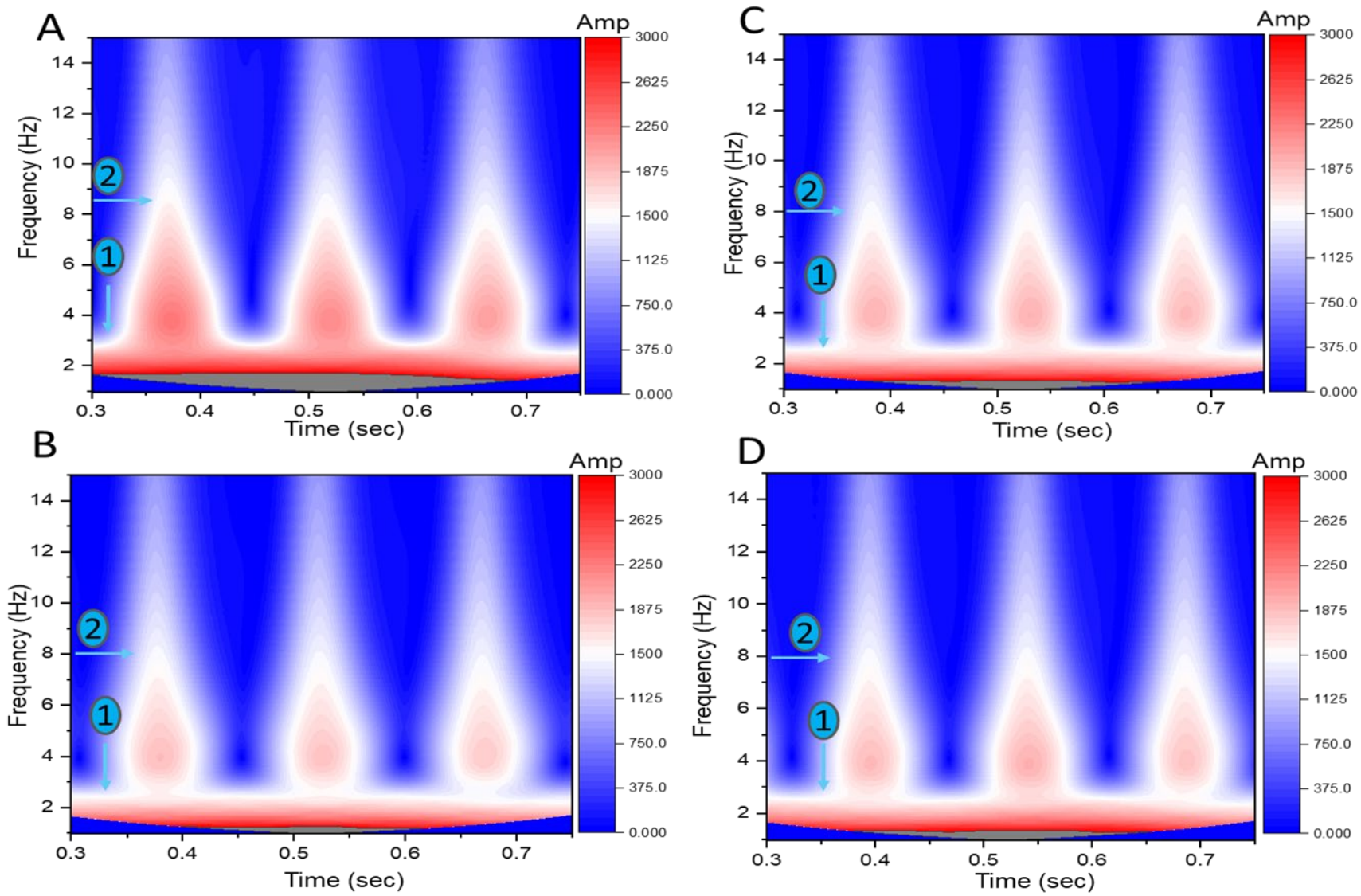
A
B
C
D
Amp
3000
2625
2250
1875
1500
1125
750.0
375.0
0.000
Frequency (Hz)
Time (sec)
0.3
0.4
0.5
0.6
0.7
2
4
6
8
10
12
14
1
2

Figure 7.

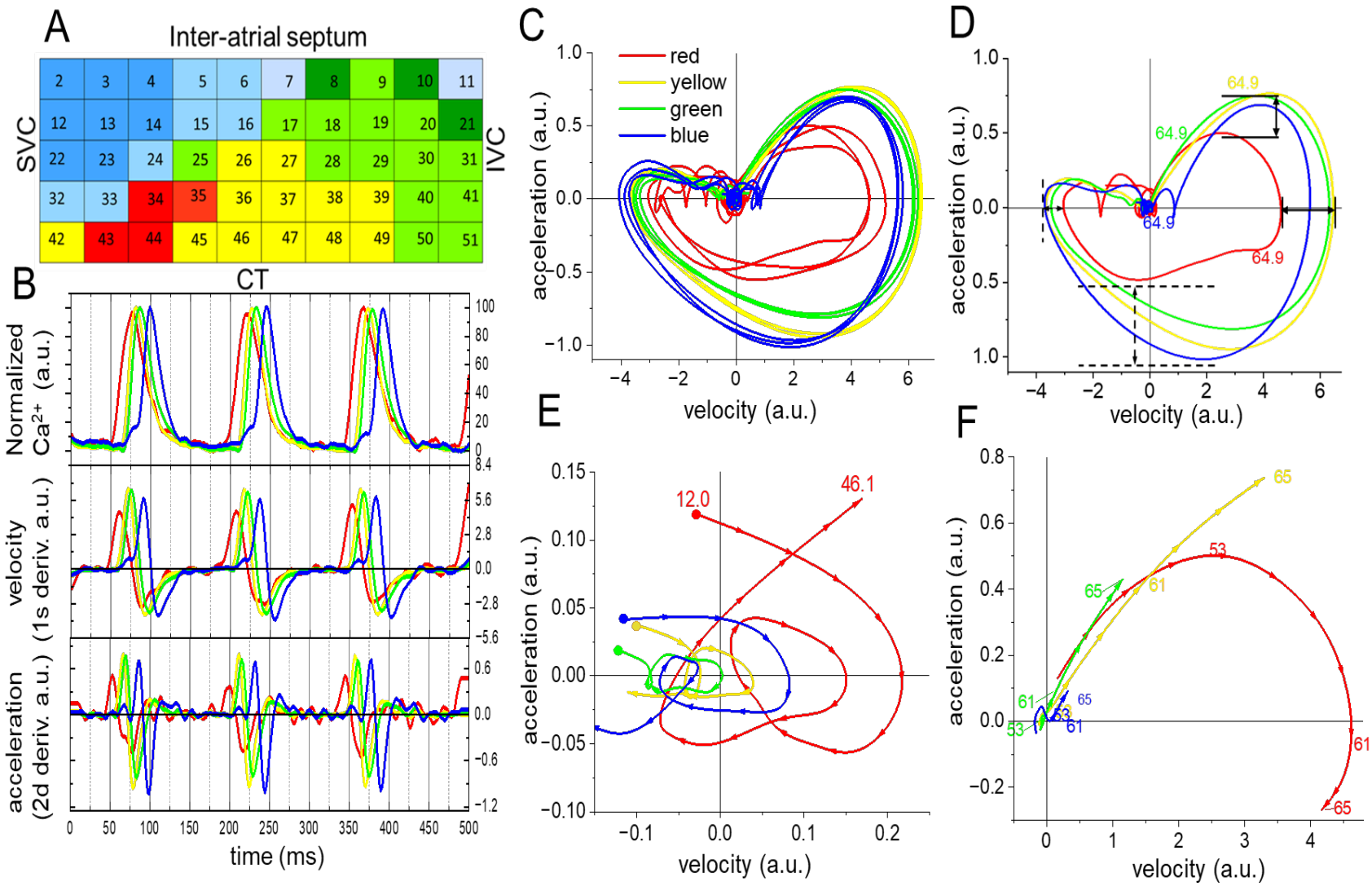
A
Inter-atrial septum
SVC
IVC
B
CT
Normalized Ca2+ (a.u.)
velocity (1s deriv. a.u.)
acceleration (2d deriv. a.u.)
time (ms)
C
red
yellow
green
blue
acceleration (a.u.)
velocity (a.u.)
D
64.9
E
12.0
46.1
F
65
53
61

Figure 8.

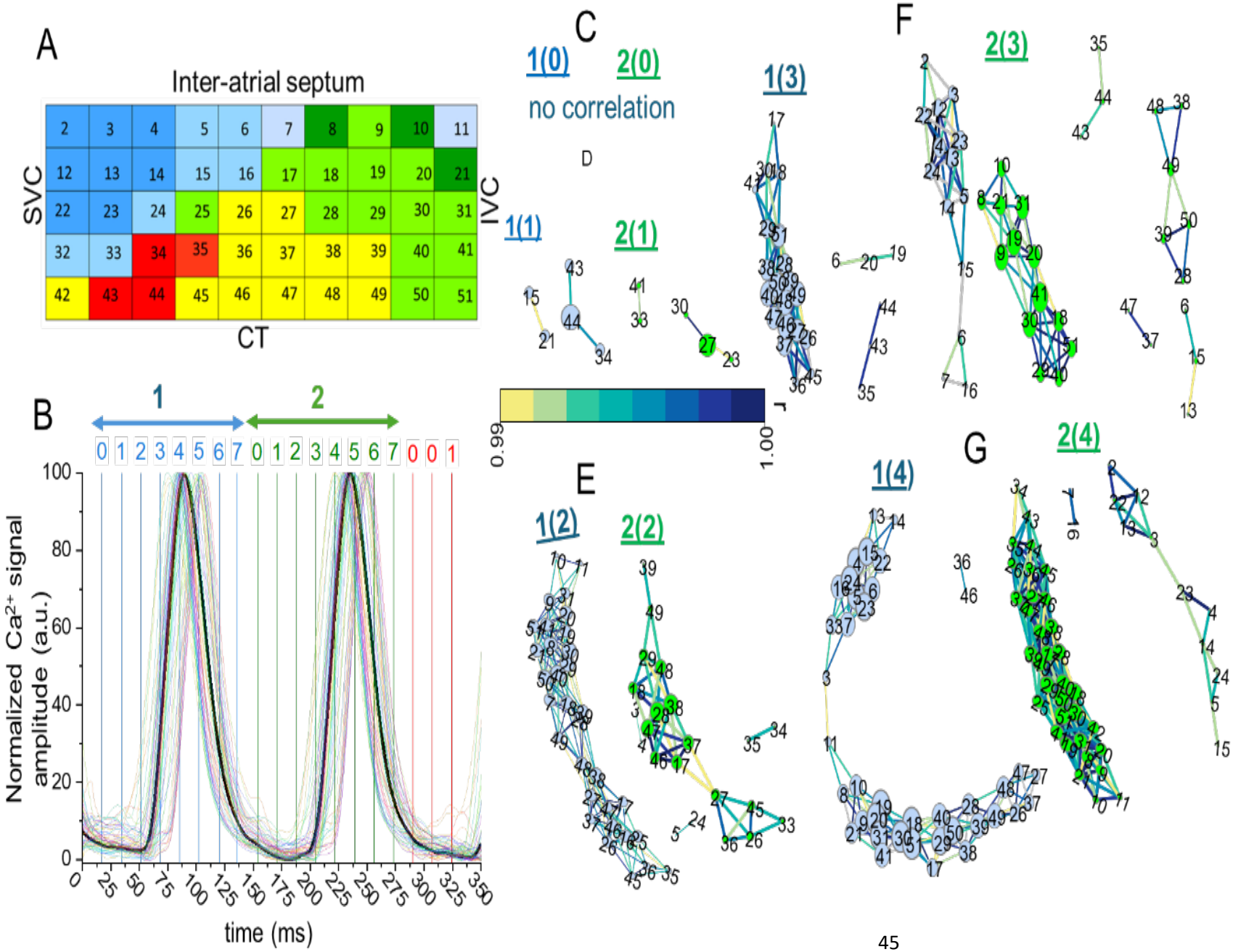
A
Inter-atrial septum
SVC
IVC
CT
B
1
2
Normalized Ca2+ signal amplitude (a.u.)
time (ms)
C
1(0)
2(0)
no correlation
1(1)
2(1)
1(3)
D
0.99
1.00
r
E
1(2)
2(2)
F
2(3)
G
1(4)
2(4)

1193

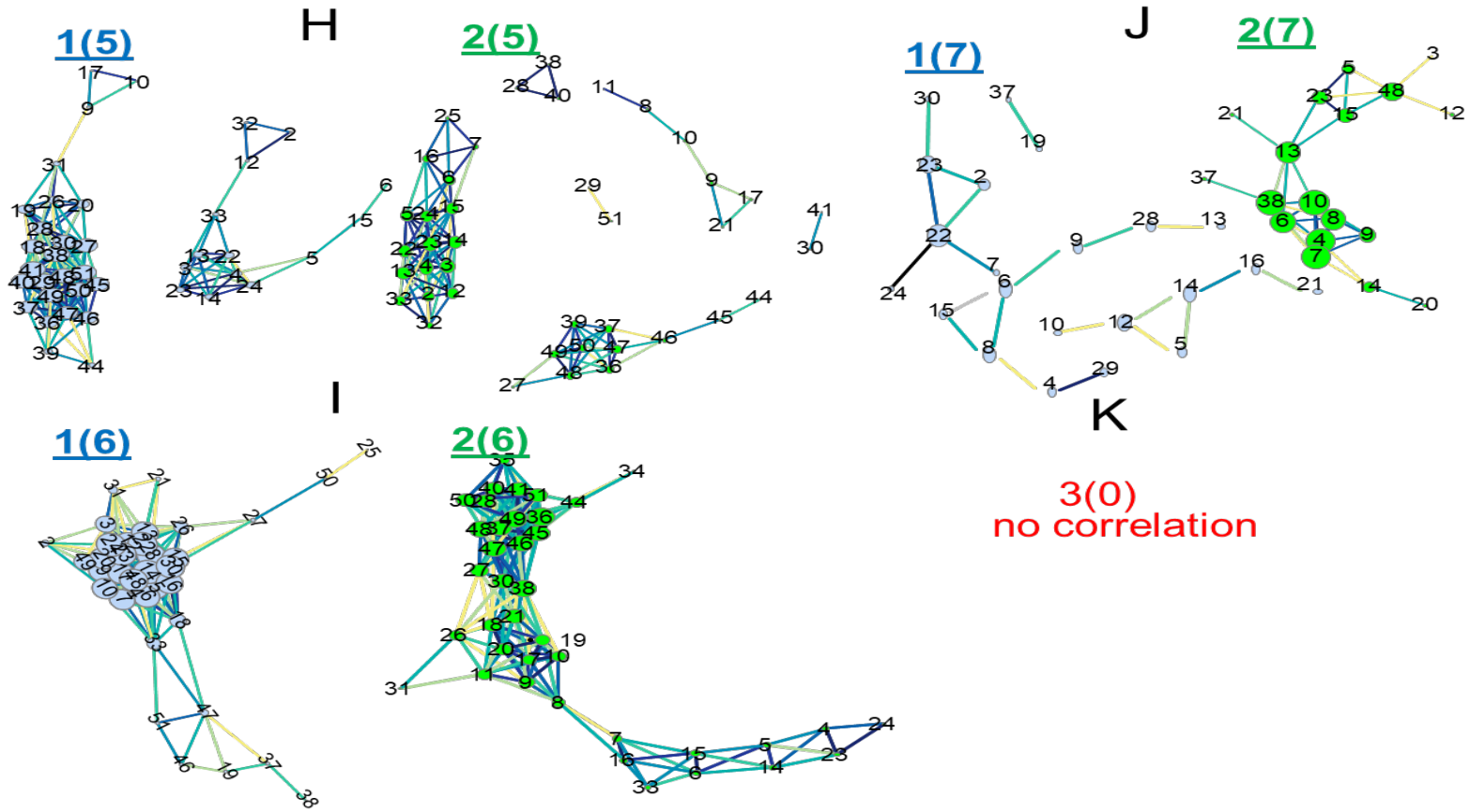

Figure 9.

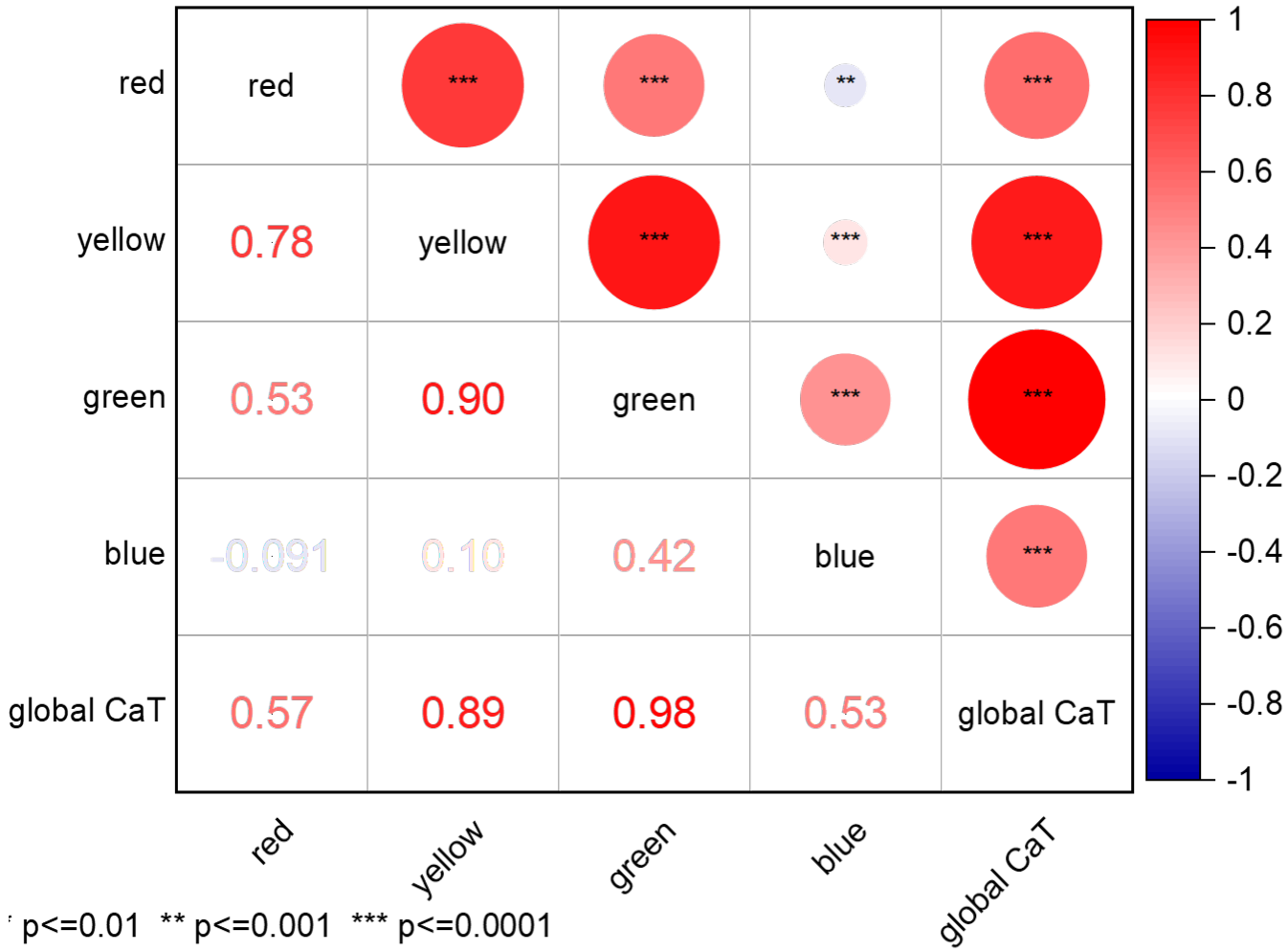
red
yellow
green
blue
global CaT
red
0.78
yellow
0.53
0.90
green
-0.091
0.10
0.42
blue
0.57
0.89
0.98
0.53
global CaT
***
**
1
0.8
0.6
0.4
0.2
0
-0.2
-0.4
-0.6
-0.8
-1
red
yellow
green
blue
global CaT
' p<=0.01 ** p<=0.001 *** p<=0.0001

Figure 10.

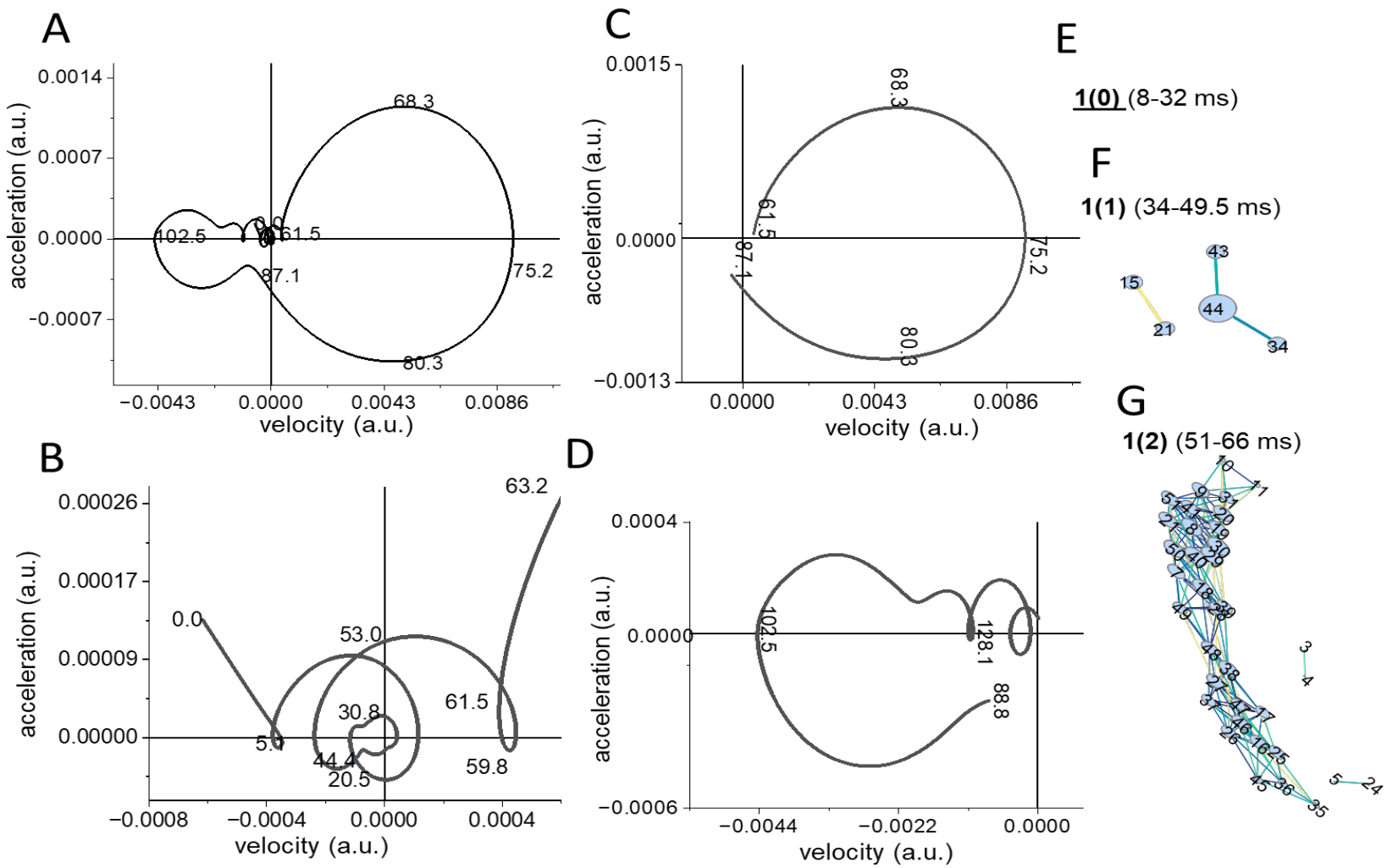
A
B
C
D
E
F
G
acceleration (a.u.)
velocity (a.u.)
1(0) (8-32 ms)
1(1) (34-49.5 ms)
1(2) (51-66 ms)

Figure 11.

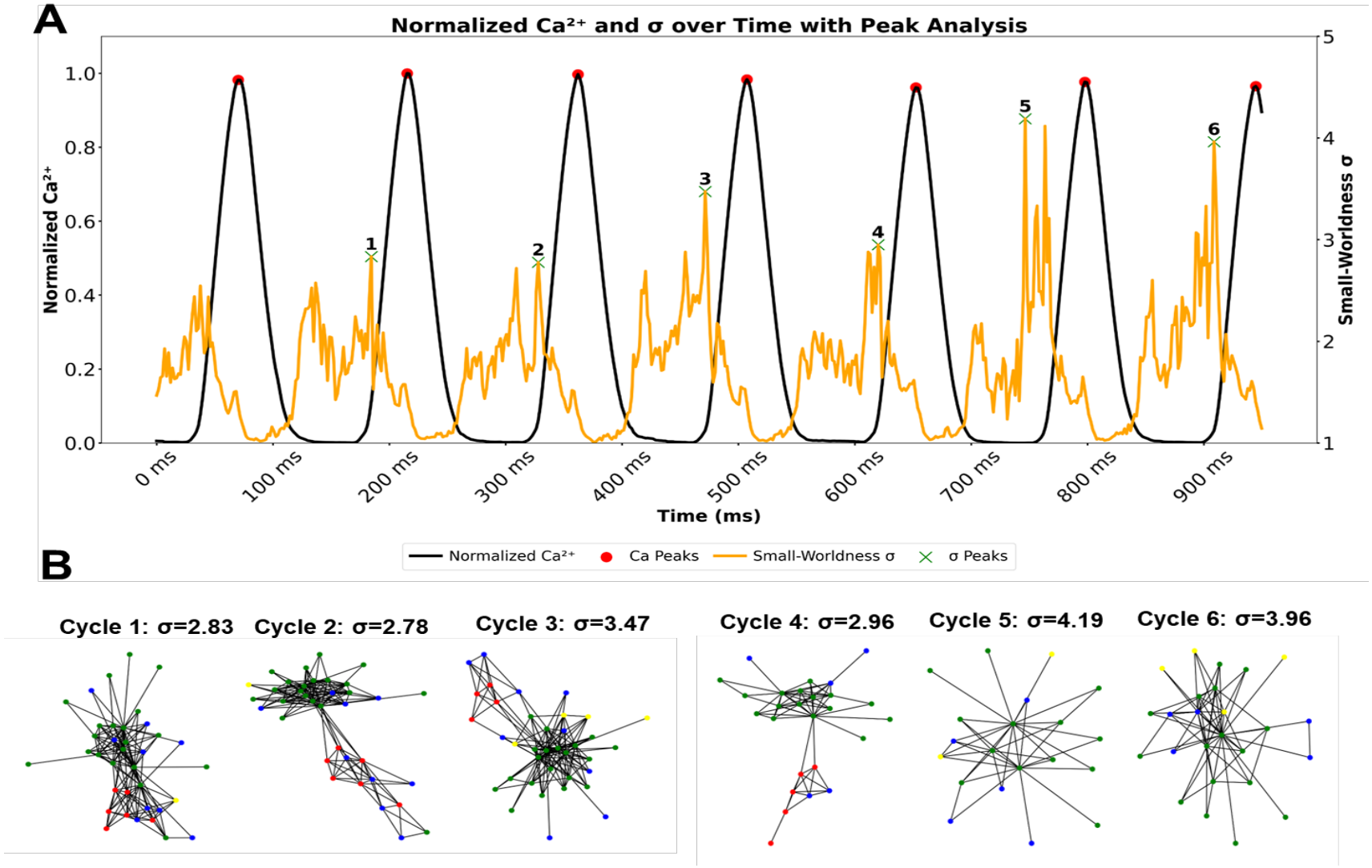
A
Normalized Ca²⁺ and σ over Time with Peak Analysis
Normalized Ca²⁺
Small-Worldness σ
Time (ms)
0 ms
100 ms
200 ms
300 ms
400 ms
500 ms
600 ms
700 ms
800 ms
900 ms
1
2
3
4
5
6
B
Normalized Ca²⁺
Ca Peaks
Small-Worldness σ
σ Peaks
Cycle 1: σ=2.83
Cycle 2: σ=2.78
Cycle 3: σ=3.47
Cycle 4: σ=2.96
Cycle 5: σ=4.19
Cycle 6: σ=3.96

Figure 12.

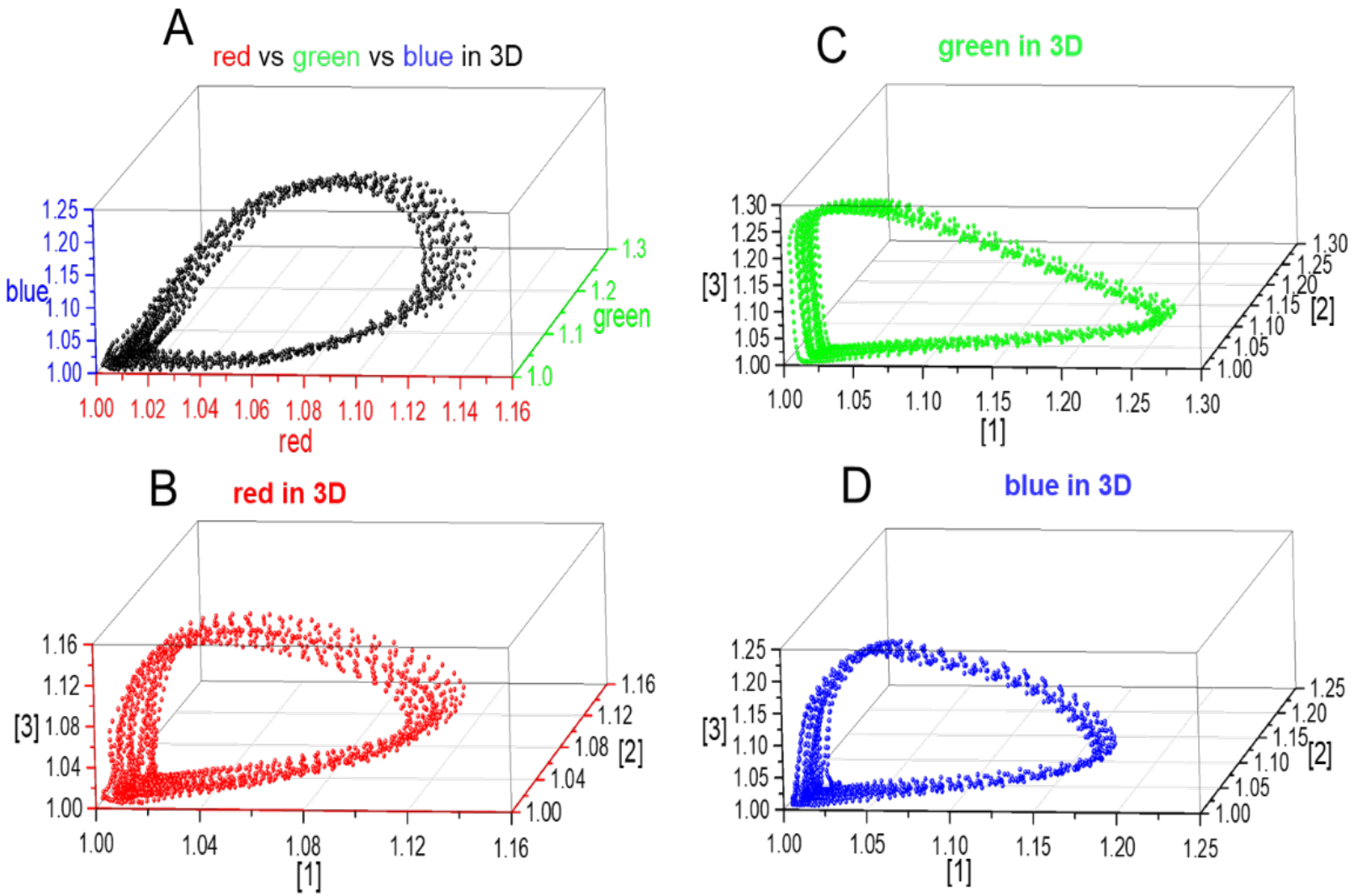
A
red vs green vs blue in 3D
blue
red
green
B
red in 3D
[3]
[1]
[2]
C
green in 3D
[3]
[1]
[2]
D
blue in 3D
[3]
[1]
[2]

Figure 13.

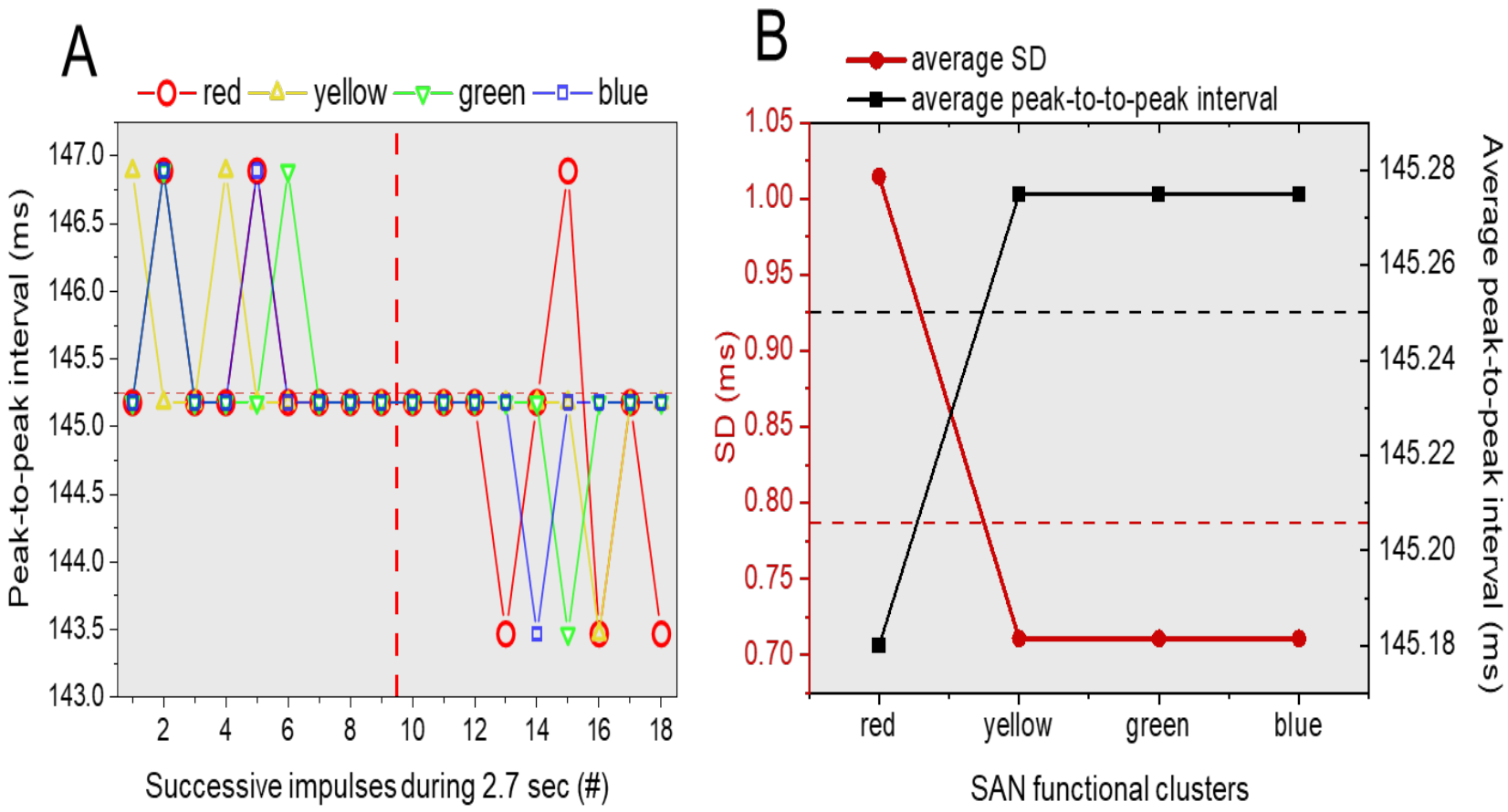
A
red
yellow
green
blue
Peak-to-peak interval (ms)
147.0
146.5
146.0
145.5
145.0
144.5
144.0
143.5
143.0
2
4
6
8
10
12
14
16
18
Successive impulses during 2.7 sec (#)
B
average SD
average peak-to-to-peak interval
SD (ms)
1.05
1.00
0.95
0.90
0.85
0.80
0.75
0.70
Average peak-to-peak interval (ms)
145.28
145.26
145.24
145.22
145.20
145.18
red
yellow
green
blue
SAN functional clusters

Figure 14.

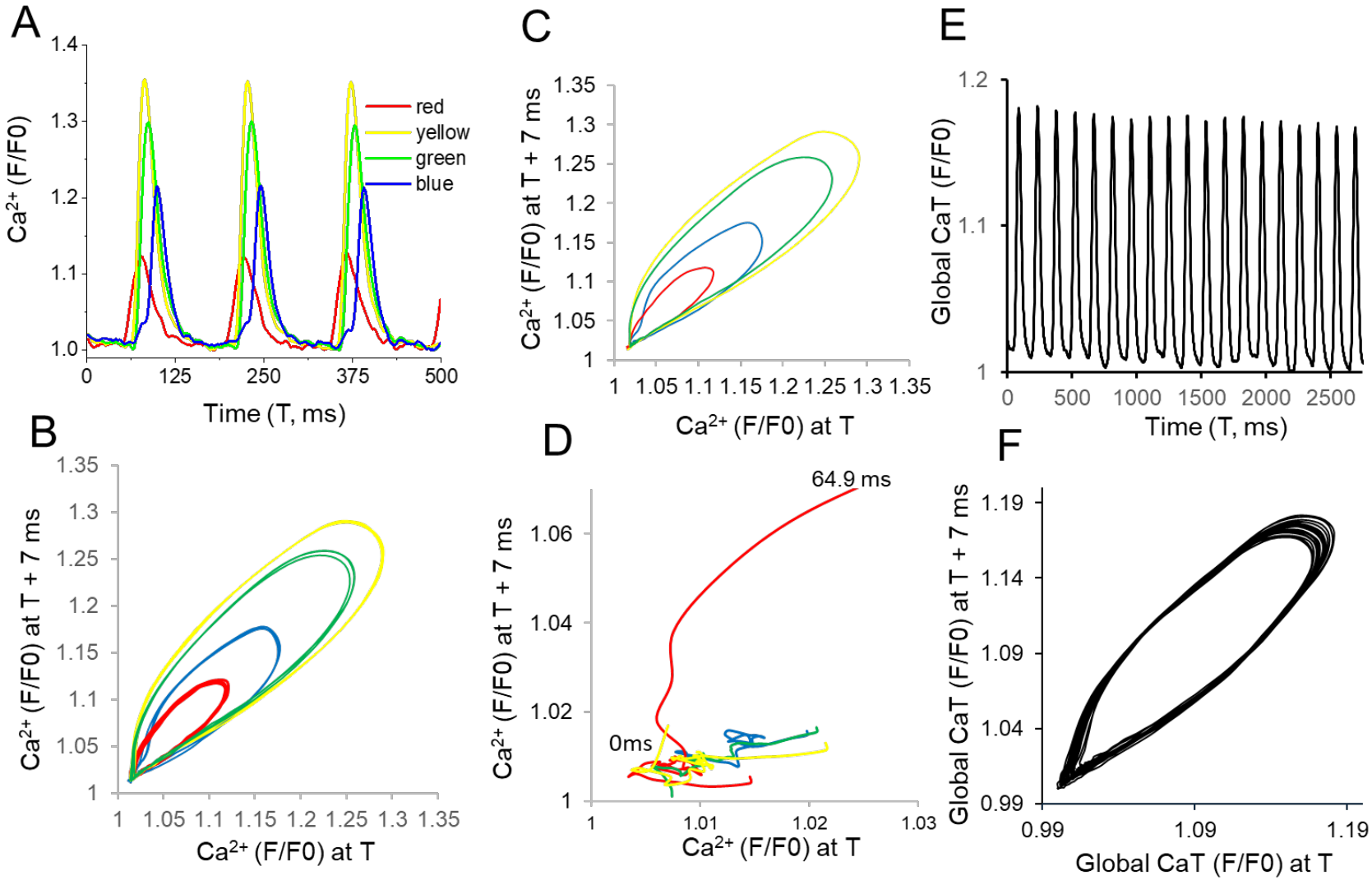
A
Ca2+ (F/F0)
Time (T, ms)
red
yellow
green
blue
B
Ca2+ (F/F0) at T + 7 ms
Ca2+ (F/F0) at T
C
Ca2+ (F/F0) at T + 7 ms
Ca2+ (F/F0) at T
D
64.9 ms
0ms
Ca2+ (F/F0) at T + 7 ms
Ca2+ (F/F0) at T
E
Global CaT (F/F0)
Time (T, ms)
F
Global CaT (F/F0) at T + 7 ms
Global CaT (F/F0) at T

Figure 15.

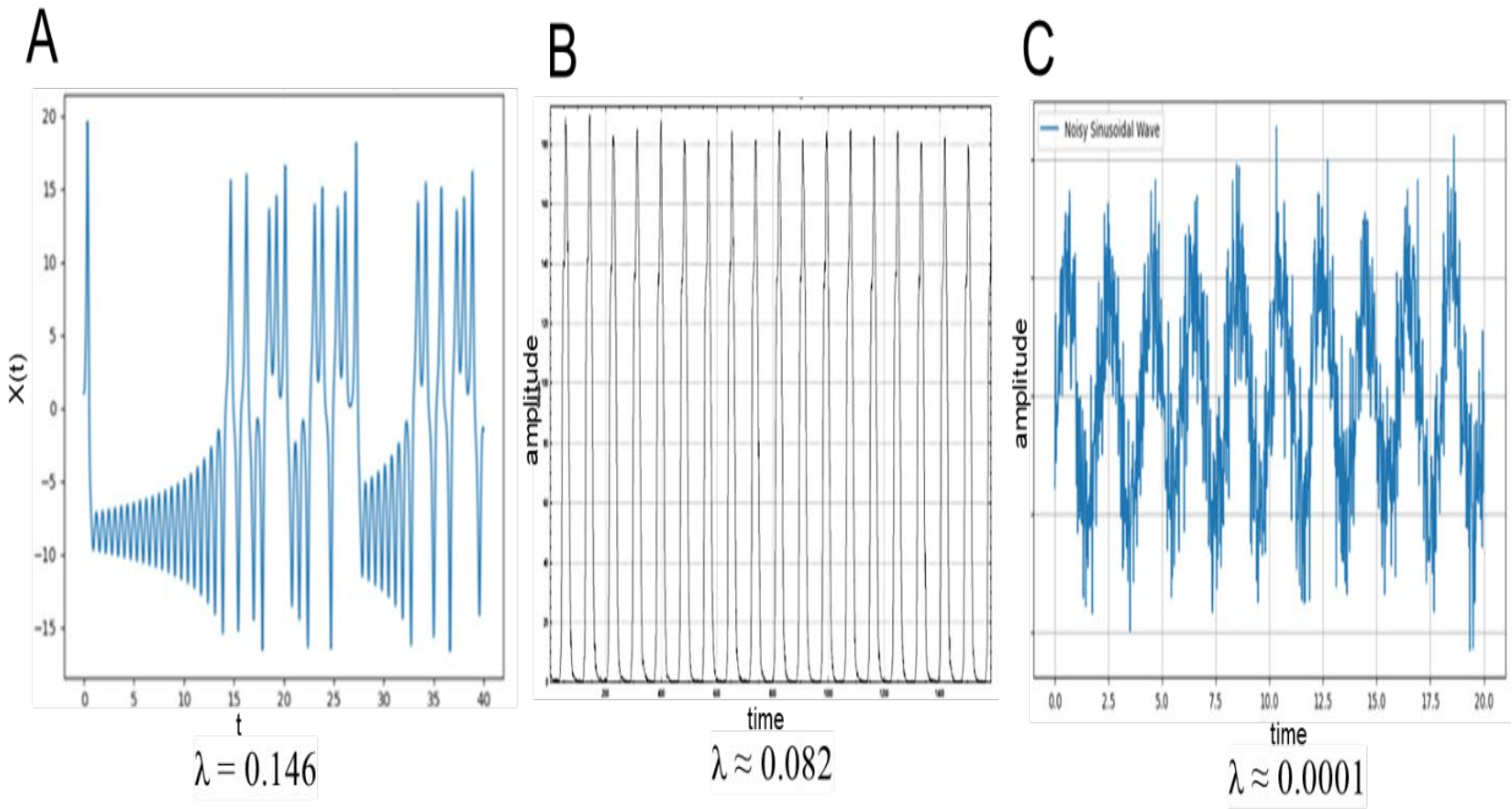
A
B
C
X(t)
t
amplitude
time
Noisy Sinusoidal Wave
amplitude
time
λ = 0.146
λ ≈ 0.082
λ ≈ 0.0001

Figure 16.

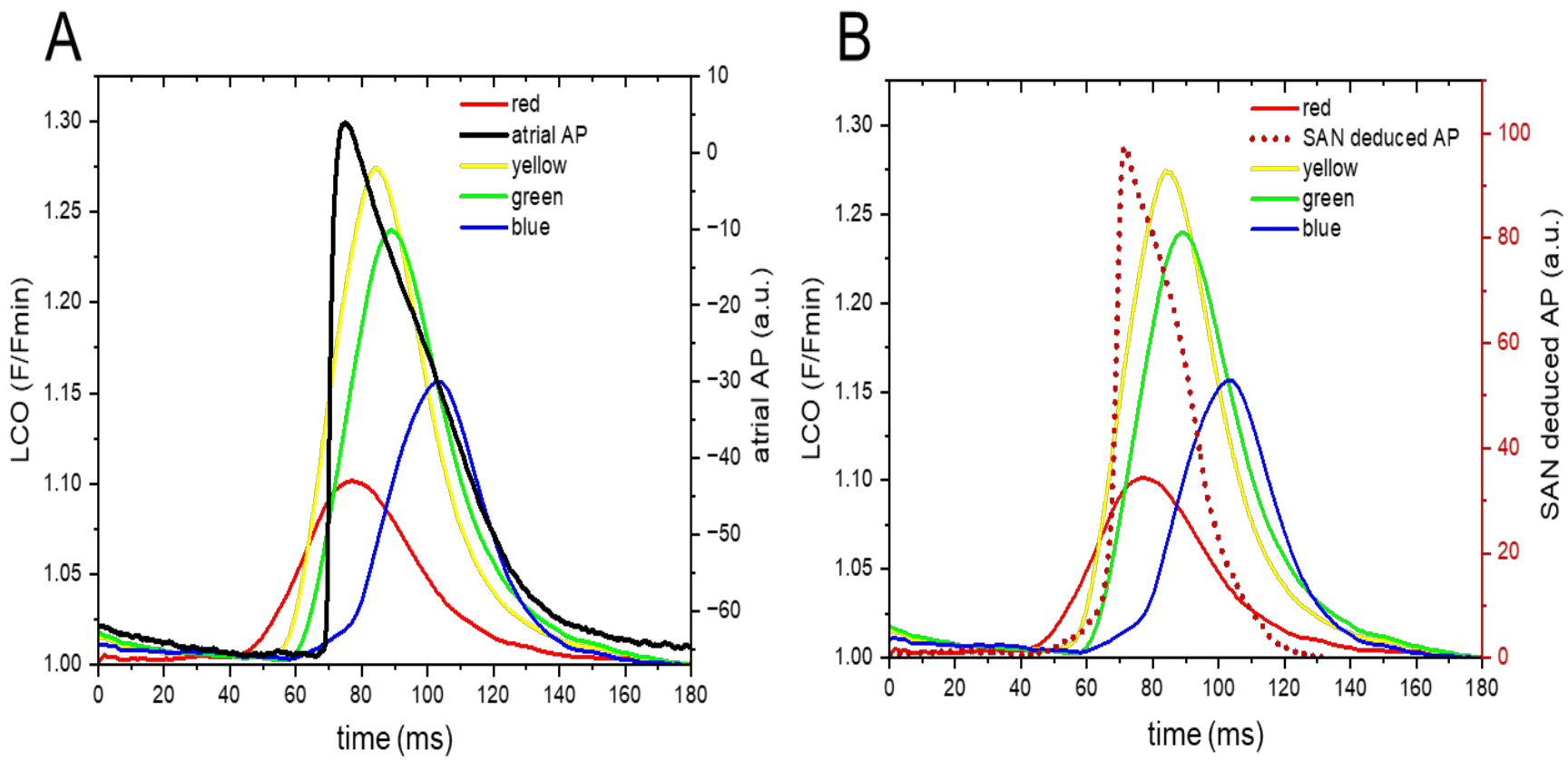
A
red
atrial AP
yellow
green
blue
LCO (F/Fmin)
atrial AP (a.u.)
time (ms)
B
red
SAN deduced AP
yellow
green
blue
LCO (F/Fmin)
SAN deduced AP (a.u.)
time (ms)

Figure 17.

Supplementary Materials

2. Methods

2.1. Sinoatrial node tissue (SAN) preparation

Our experiments conformed to the Guide for the Care and Use of Laboratory Animals, published by the US National Institutes of Health. The experimental protocols were approved by the Animal Care and Use Committee of the National Institutes of Health (protocol # 457-LCS-2027).

The sinoatrial node (SAN) tissue was dissected from the heart of young (3 month-old) C57BL/6J mice (Charles River Laboratories, USA) (n=4) as previously described (1). Mice were anesthetized with Isoflurane (inhalation at 2-3% for induction and 1-1.5% for maintenance) and monitored until the loss of reflexes to tail pinch confirmed the adequacy of anesthesia. The heart was rapidly excised and immediately transferred to a cold (4°C) oxygenated standard Tyrode solution containing (in mM): 130 NaCl, 24 NaHCO3, 1.2 NaH2PO4, 1.0 MgCl2, 1.8 CaCl2, 4.0 KCl, 5.6 glucose, equilibrated with 95% O2 / 5% CO2 (pH 7.4 at 35.5°C). The heart was pinned onto a silicon platform, and the right atrium was carefully opened to expose the SAN region, including the crista terminalis, intercaval area, and interatrial septum, with the superior and inferior vena cava (SVC and IVC) kept intact. The preparation was then pinned to the bottom of a *oxygen*-controlled experimental chamber with the endocardial side facing upward, ensuring minimal stretch to flatten the SAN tissue.

2.2. Data acquisition of local Ca2+ signals/oscillations (LCO) during impulse formation in SAN ex vivo

The SAN preparation (n=4) was incubated with Calbryte 520 AM (25 μM) a fluorescent calcium indicator, for 1.5 hours at room temperature. After washout of dye for 20 min, local Ca2+ signals (LCOs) were recorded in Tyrode solution (as above) with 5x magnification at 35.6C and acquisition rate 1.7ms for 2.7 sec via a stationary fixed stage upright microscope (Axio Examiner D1 equipped with zoom tube (0.5–4x), Carl Zeiss Microscopy LLC) and PCO edge 4.2 camera as previously discussed (1). The epifluorescence microscope with a CoolLED pE-300ultra light source was set to 40% power to optimize signal-to-noise ratio and maintain tissue viability. The excitation light was directed through a 498 nm dichroic mirror, and emitted fluorescence was collected through a 530±20 nm filter. Imaging was conducted at *magnification 5x* to capture detailed cellular Ca2+ dynamics within the SAN.

To minimize motion artifacts during recordings, preparations were treated with 10 μM cytochalasin D to inhibit mechanical contraction (1). Residual motion artifacts were corrected during post-processing using ImageJ. The high temporal (500–700 Hz) and spatial resolution allowed for the construction of spatiotemporal maps of SAN cell network activation. Ca2+ signal intensity remained stable for *the entire experiment.*

2.3. Atrial cell action potential recording

Because action potential (AP) characteristics differ in the SAN pacemaker cells among regions of the SAN (1), to deduce the timing of SAN action potential (AP), we placed reference electrode in atria near the crista terminalis (CT). To record the transmembrane potential (AP), we used sharp microelectrodes (40–100MΩ) fabricated from aluminosilicate glass capillaries (1.5mm OD 0.86mm ID) with a horizontal pipette puller (Sutter Instruments, CA, USA), and back-filled with 3M KCl. Each microelectrode was inserted from the endocardial side of the tissue, and APs were recorded with a high-impedance amplifier (A-M Systems, USA) with a virtual bridge circuit for current injection. The electrical signal was digitized with Digidata 1440 and analyzed with PCLAMP10 software (both from Molecular Dynamics, USA).

2.4. Data analysis

Original Ca2+ signals recorded during 2.7 sec were preprocessed in ImageJ and then a local Ca2+ signal pixels intensity (LCO) within the image was extracted by applying a 50 equaled size grid (68x100 pxl). Next, the smoothing of the extracted LCO data was performed, using Savitzky-Golay method, to remove noise or irregularities in the of the origin LCO signal, followed by normalization of the maximum LCO signal of each of the 50 ROI to its minimum signal (F/Fo) over time. The Ca2+ signals were presented as F/Fo values or as a percent of LCO change in each ROI (F-min(F))/(max(F)-min(F)). Time series were generated from the space-averaged LCO signal within each ROI for each frame in the sequentially recorded stack of images. When necessary, a first-order differencing of time series was applied to transform to transform non-stationary time series into stationary ones.

In the present study, we applied a diverse set of linear and nonlinear analytical analyses of local Ca2+ (LCO) dynamics using multiple software programs: Microsoft Excel, OriginLab, MATLAB 2024a, R, pCLAMP 10.4, our custom-made programs to analyze APs and Ca2+ transients dynamics (Victor Maltsev).

2.4.1. Cosinor-based analysis (Germaine Cornelissen**)** was applied to measure the acrophases in each ROI, the times from a reference point (0) to the time of maximum amplitudes, during the first 200 ms of impulse formation to pinpoint initiation of Ca2+ signal change among ROIs.

2.4.2. Amplitude and derivative analyses were applied to assess heterogeneity in amplitudes and kinetics of LCOs during different phases of impulse formation within and between LCOs.

2.4.3. Tangent analysis was applied to identify the slow phase of the global Ca2+ signal.

2.4.4. Pearson correlation analysis was applied as a function of window rolling (~15ms) to the normalized LCO amplitude of 50 ROIs to identify the strength of a linear correlation between LCOs of ROIs.

2.4.5. Network cross-correlation analysis was applied to identify functional LCOs clustering patterns (network solutions) within and between LCOs (r =>0.99, Fruchterman–Reingold Force-directed plots) during impulse formation.

2.4.6. Functional data analysis (FDA) was applied to illustrate the nonlinear dynamic of the energy transfer in the Ca2+ signal during impulse formation.

2.4.7.Embedded phase-plane analysis was applied to study network solutions in SAN global and regional Ca2+ signals by assessing the deviation from the limited cycle and the presence of chaos during each Ca2+ impulse (2, 3).

2.4.8. *Manifold reconstruction of the original signal in 3D*

The process involved reconstructing the manifold of four color-coded ROIs to analyze and forecast the characteristics of the initial time series in specific conditions. This was achieved by examining the interactions in a three-dimensional phase space between the original signals and the reconstructed signals. Takens' theorem (4), time dependence, nearest neighbors, Cao's method(5), and mutual information were utilized to evaluate and embed the original data in an M-dimensional manifold where all possible states could be determined from a set of initial conditions. The average mutual Information (AMI) of the four color-coded clusters was used to calculate optimal time delay (τ), the time lag where the AMI declined and compared with the first local zero-crossing of the autocorrelation function (ACF) to choose a shortest embedding $\boldsymbol{\tau}$. Gao's method to estimate the embedding dimension (d) from a time series using 2 functions, the E1(d) and the E2(d)

functions. E1(d)=1, determines the optimal embedding dimension; E2(d) is a check of nonlinearity in time series (E2(d) $\neq$1).

2.4.9. Principal component (PCA) analysis was used to determine the direction of the maximum variances within SAN Ca2+ signals of the four color-coded regions during three critical phases of the global Ca2+ impulse (CaT) formation. The following markers were used as reference points for PCA in the regional clusters: the ignition phase (where the second derivative of the global CaT, d^2Ca/dt^2, transitions from zero to its maximum), the fast phase (where d^2Ca/dt^2 reaches its peak and progresses to the CaT maximum), and the decay phase (where the CaT returns to baseline). Four principal components were extracted, where PC1 and PC2 accounted for the most variances in the Ca2+ dynamics.

2.4.10. Lorenz attractor analysis was applied to quantify the degree of chaos in the system via estimation of the Lyapunov exponent of deterministic chaos ($\lambda = 0.146$), a non-chaotic system ($\lambda \approx 0.0001$). Instead of a butterfly's height, we are tracking the amplitude of the Ca2+ signal. Plotting the current amplitude value against its previous values reveals the patterns of Ca2+ signals change over time that are not usually obvious from the original time series.

To estimate λ in the Ca2+ signal, we employed a two-dimensional phase space reconstruction technique with lag = 1, minimum time separation = 4, tau = 1, and minimum neighbors = 10. The unit lag and tau ensured high temporal resolution, allowing analysis of the system's state at consecutive time points without skipping any data. The minimum time separation of four helped mitigate the effects of short-term correlations (by ensuring that, we compare points that are at least fourtime steps apart). The criterion of 10 minimum neighbors for divergence calculations enhanced the statistical reliability of our Lyapunov exponent estimation by ensuring sufficient data points for analysis. These settings helped to optimize dynamics while maintaining statistical robustness with two-dimensional embedding.

2.4.11. Fixed points stability analysis

An understanding of fixed points is to determine the behaviors of dynamic systems because these points represent the solution where the system could come to equilibrium. First, the fixed points of LCO of different ROIs were marked on 1st derivative curves (when $f(x^*) = 0$, velocity is not changing over time). Next, to assess stability, we evaluate the behavior of the system in the

vicinity of the fixed points via linearization of the infinite polynomial function near a fixed point (Taylor series expansion).

$f(x) = f(x*) + f'(x*)[x-x^*] + \frac{1}{2}f''(x^*)[x-x^*]^2 + \ldots$ (1)

$f(x) \approx f'(x*)[x-x^*]$ (2)

$\frac{dx}{dt} = f'(x*)[x-x^*]$ (3)

Integration of some steps of equation 3, generates equation 4, which represents the equation of motion near fixed points.

$x - x^* = Ae^{f'(x^*)t}$ (4)

The sign of the 1st derivative in the vicinity of fixed points, informs on a behavior of the system. A fixed point is stable (a 'sink') if perturbations lead the system back towards it, while it is unstable (a 'source') if perturbations push the system away. Therefore, if dCa/dt > 0, the solutions of the system will be unstable at this fixed point because the distance from the fixed point will exponentially increase; if dCa/dt < 0, it is a stable fixed point since the distance from the fixed point decays to zero. The sensitivity of the system can be significantly increased during the transition in the phase plane, where curves are near unstable fixed points.

2.4.12.Empirical Mode Decomposition (EMD)

The 2.7-second time series recording of Ca2+ signals was analyzed using Empirical Mode Decomposition (EMD) (6). EMD is an adaptive decomposition technique used to extract frequencies from nonstationary signals. Compared to Fourier transform, EMD takes into account the non-linearity of the signal by iteratively sifting the original signal to extract oscillatory components known as Intrinsic Mode Functions (IMFs). The residual after the sift represents a non-oscillatory trend component. IMFs are characterized by several features, including local symmetry around zero and containing the same number of extrema as zero-crossings (or differing by no more than 1).

2.4.13. Hilbert-Huang (HHT) transform analysis that does not require signal stationarity was applied to compute the instantaneous phase, frequency, and amplitude of each IMF and quantify the power within a signal distributed across frequencies (7).

2.4.14. Modified modified Short-Time Fourier Transform (STFT-FD). In contrast to standard SFFT in which the window size is fixed in the frequency domain, STFT-FD applies a window

that varies in size based on frequency, fixing the window size in the frequency domain (8). This technique provides better resolution at different frequency ranges within the signals, especially when analyzing signals with rapidly changing frequencies.

2.4. 15. A small-world network analysis a powerful tool from network science was applied to investigate Ca2+ dynamic. To enhance the signal quality and separate calcium activity from noise in our raw imaging data series of preprocessing steps was applied. The penalized matrix decomposition (PMD) method was first applied, which decomposes the data into low-rank signal and noise components. Specifically, the patch-wise PMD (TV,TF) algorithm was used, applying total variation (TV) regularization spatially and trend filtering (TF) temporally. This step effectively denoised and compressed the data, improving the signal-to-noise ratio. Following the PMD, we applied a simple threshold to the data to further isolate signal from noise. We then used a median filter to smooth the thresholded data, which helped eliminate any remaining salt-and-pepper noise that might have persisted after the PMD and thresholding steps. The combination of PMD, thresholding, and median filtering significantly enhanced the visibility of calcium activity patterns and cellular structures, as evident in the improved clarity and contrast of the processed images in Supplementary Method Fig. 1 and Movie S2.

For each time window, weighted graphs based on mutual information matrices were constructed; edges with top values above 2.0 were thresholded; and clustering coefficients and path lengths metrics were computed. These metrics were then compared to random graph models to derive the small-worldness metric σ. By calculating small-worldness (σ) over sliding windows throughout the cardiac cycle, network topology was constructed.

Our analysis combined mutual information calculations and theoretical graph measures to analyze the functional connectivity and network property of the integrated (global) Ca2+ signal in the SAN (Fig. Method S1A). For each rolling time window during the 2.7 sec time series of SAN Ca2+ recording, weighted graphs based on mutual information matrices (Fig. S1B) were constructed (edges with top values above 2.0 were thresholded; and finally clustering coefficients and path lengths metrics were computed (Fig. S1A,C). These metrics were then compared to random graph models to derive the small-worldness metric σ, is the ratio of the average clustering coefficient and average shortest path length. For each time window, weighted graphs based on mutual information matrices were constructed; edges with top values above 2.0 were thresholded; and clustering coefficients and path lengths metrics were computed. These metrics were then

compared to random graph models to derive the small-worldness metric σ. By calculating small-worldness (σ) over sliding windows throughout the cardiac cycle, network topology was constructed. Our analysis combined mutual information calculations and theoretical graph measures to analyze the functional connectivity and network property of the integrated (global) Ca2+ signal in the SAN (Fig. Method S1A). For each rolling time window during the 2.7 sec time series of SAN Ca2+ recording, weighted graphs based on mutual information matrices (Fig. S1B) were constructed (edges with top values above 2.0 were thresholded; and finally clustering coefficients and path lengths metrics were computed (Fig. S1A, C). These metrics were then compared to random graph models to derive the small-worldness metric σ, is the ratio of the average clustering coefficient and average shortest path length.

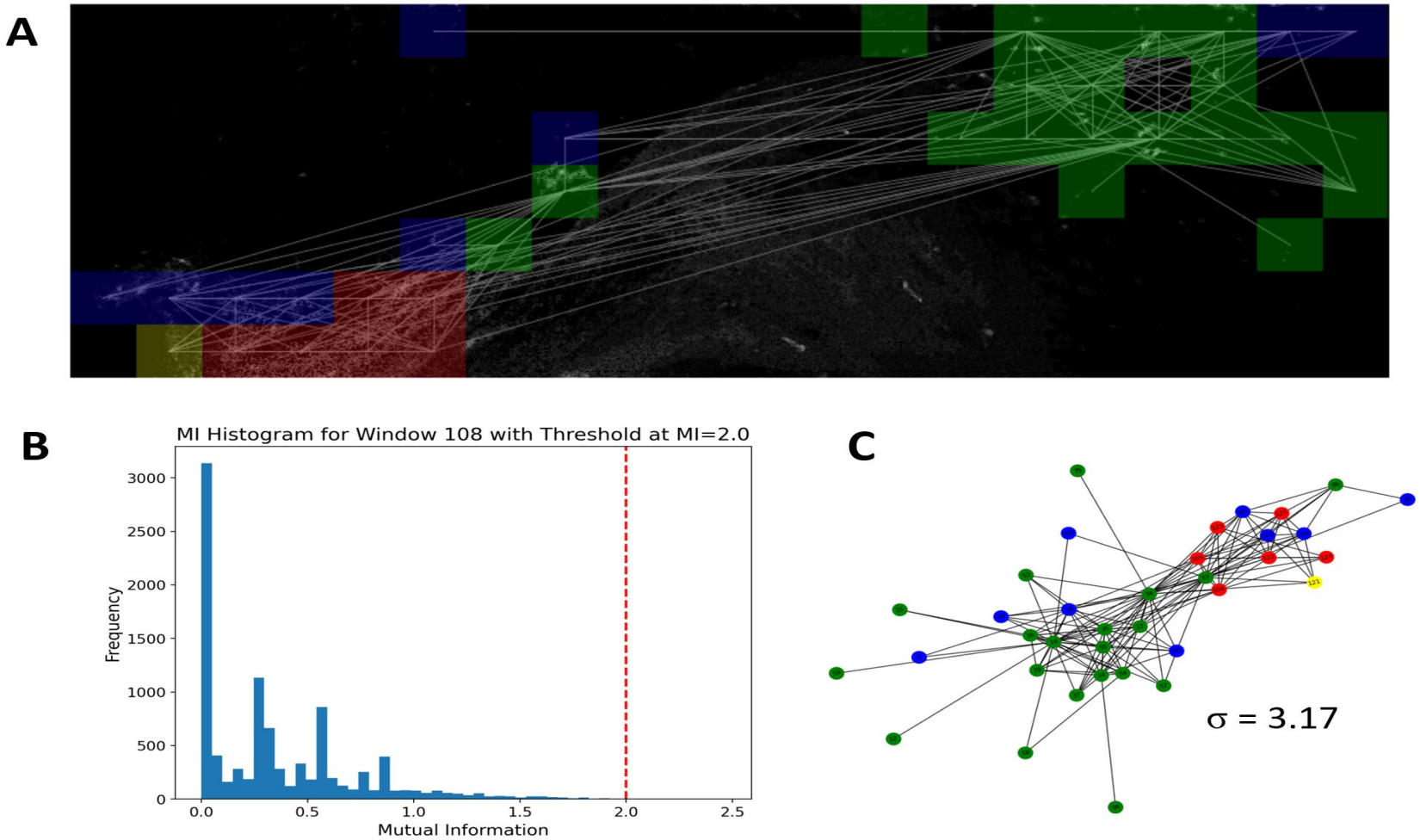

Supplementary Method Fig. 1: Small-world network analysis of the integrated (global) SAN Ca2+ signal. (A) Spatial representation of functional connectivity in the SAN, with colored regions indicating different functional clusters and white lines representing connections above the mutual information threshold. (B) Histogram of mutual information (MI) values for a representative time window, with the red dashed line indicating the threshold (MI=2.0) used for network construction. (C) Example of a small-world network graph derived from thresholded MI values, with nodes colored according to their functional cluster and σ indicating the small-worldness metric for this particular network configuration.

Atrial cell action potential

Because action potential (AP) characteristics differ in the SAN pacemaker cells among regions of the SAN (1), to deduce the timing of SAN action potential (AP), we placed reference electrode in atria near the crista terminalis (CT). To record the transmembrane potential (AP), we used sharp microelectrodes (40–100MΩ) fabricated from aluminosilicate glass capillaries (1.5mm OD 0.86mm ID) with a horizontal pipette puller (Sutter Instruments, CA, USA), and back-filled with 3M KCl. Each microelectrode was inserted from the endocardial side of the tissue, and APs were recorded with a high-impedance amplifier (A-M Systems, USA) with a virtual bridge circuit for current injection. The electrical signal was digitized with Digidata 1440 and analyzed with PCLAMP10 software (both from Molecular Dynamics, USA).

Supplementary Movies:

Supplementary Movie S1. From Bychkov et al., JACC: Clinical Electrophysiology (2020) with permission. Movie S1.pptx

Supplementary Movie S2. A novel filtering process of Ca2+ events, included trend filter denoising (based on spatially-localized-penalized matrix decomposition used on 2D neuronal dendrite activity), thresholding and median filter were applied to raw Ca images to enhance the signal quality and separate Ca2+ activity from noise in small-world analyses. Movie S2.pptx

Supplementary Movie S3. 3D diagrams of the global CaT (F/F0) acceleration, velocity, and time across 19 impulses as shown in supplementary Fig. 5 panel C. Movie S3.pptx

Supplementary Figures:

Supplementary Figure 1: Principal component analysis (PCA) of the normalized Ca2+ amplitude rate of change across four distinct color-coded clusters throughout the entire time series comprising 19 impulses. (A) Principal Component 1 (PC1) and Principal Component 2 (PC2) representing 19 impulses of the four color-coded clusters are superimposed during the ignition phase of the global calcium transient (CaT), defined at the point where the second derivative of the CaT, d^2Ca/dt^2, shifts from zero to its maximum. (B) PC1 and PC2 for the 19 impulses of the four color-coded clusters superimposed during the rapid phase of the global CaT, corresponding to the period when d^2Ca/dt^2 reaches its peak and advances toward the maximum CaT, annotated as phase 2 in panel B. (C) PC1 and PC2 of the 19 impulses of the four color-coded clusters are depicted during the decay phase of the global CaT, which is characterized by the return of the CaT to baseline levels.

Supplementary Fig. 2: Displays the frequency spectrum of the averaged Ca^{2+} signals for the red (A), yellow (B), green (C), and blue (D) clusters analyzed over 2.7-second intervals. The

data were processed using Empirical Mode Decomposition (EMD) and Hilbert-Huang transform techniques.

Supplementary Fig. 3: A Pearson correlation analysis was conducted using a continuous window rolling approach (~15 ms) on the normalized LCO amplitude across 50 regions of interest (ROIs, colored traces) during the initial impulse formation phase. Each 15 ms segment is labeled numerically (0-7) along the vertical axis in panel A. The global Ca2+ signal waveform is depicted in black.

Supplementary Fig. 4: Pearson correlation analysis as a function of continuous window rolling (~15ms) was applied to the normalized LCO of 50 ROIs (colored traces) during the second cycle (marked as 2 in A). Each 15ms segment is labeled with numerical numbers (0-7) indicated by the vertical axis in panel A. The global Ca2+ signal waveform is shown in black.

Figure 5. Functional data analysis (FDA) of energy transfer from Ca2+ dynamics during impulse formation. (A) Global Ca2+ signal waveform(CaT, upper panel) and its 1st (middle panel) and 2nd (lower panel) derivatives over 350 ms. (B) Phase-plane diagrams of acceleration (2nd derivative) vs. velocity (1st derivative) for the first impulse, labeled with respective time. (C) Superimposed phase-plane diagrams of CaT across 19 cycles, showing cycle-to-cycle variations in velocity and acceleration (red lines and arrows). The circular-like trajectories vary in size, indicating differing energy transfer rates and an overall lack of equilibrium in Ca2+ dynamics throughout the 2.7 seconds, as evidenced by the absence of 0: 0 crossings. See also supplementary Movie S3

Supplementary Fig. 6 Orbit plots show the normalized Ca2+ signaling within selected ROIs from each of the four distinct color-coded clusters identified during the 2.7-second time-series recording **(A-D)**. The plots depict both unlagged and lagged (7 ms) representations of the Ca2+ signal amplitude across each cluster. Insets compare variation within and between RPIs.

Supplementary Fig. 7 Panel A illustrates the global SAN Ca2+ transient (CaT) and deduced SAN AP. Note the relationship of the slow foot of Ca2+ dynamic to the slow foot of the deduced SAN AP during the AP ignition phase (AP arrows). Panel B illustrators the relationship of the SAN deduced AP to the AP recorded in the right atrium with the sharp microelectrode. Nore the lack of the slow foot in atrial AP during SAN AP ignition.

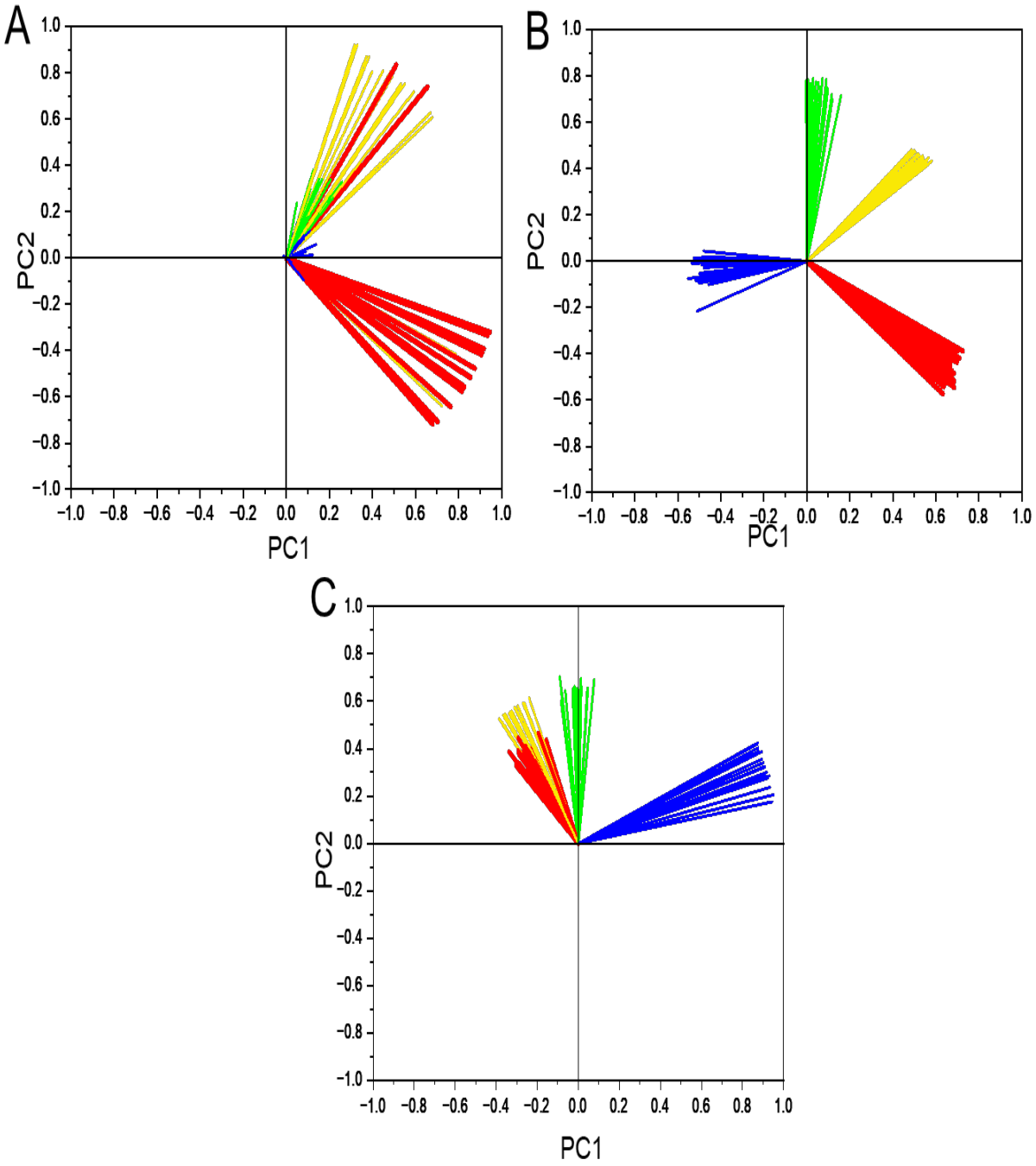

Fig.S1.

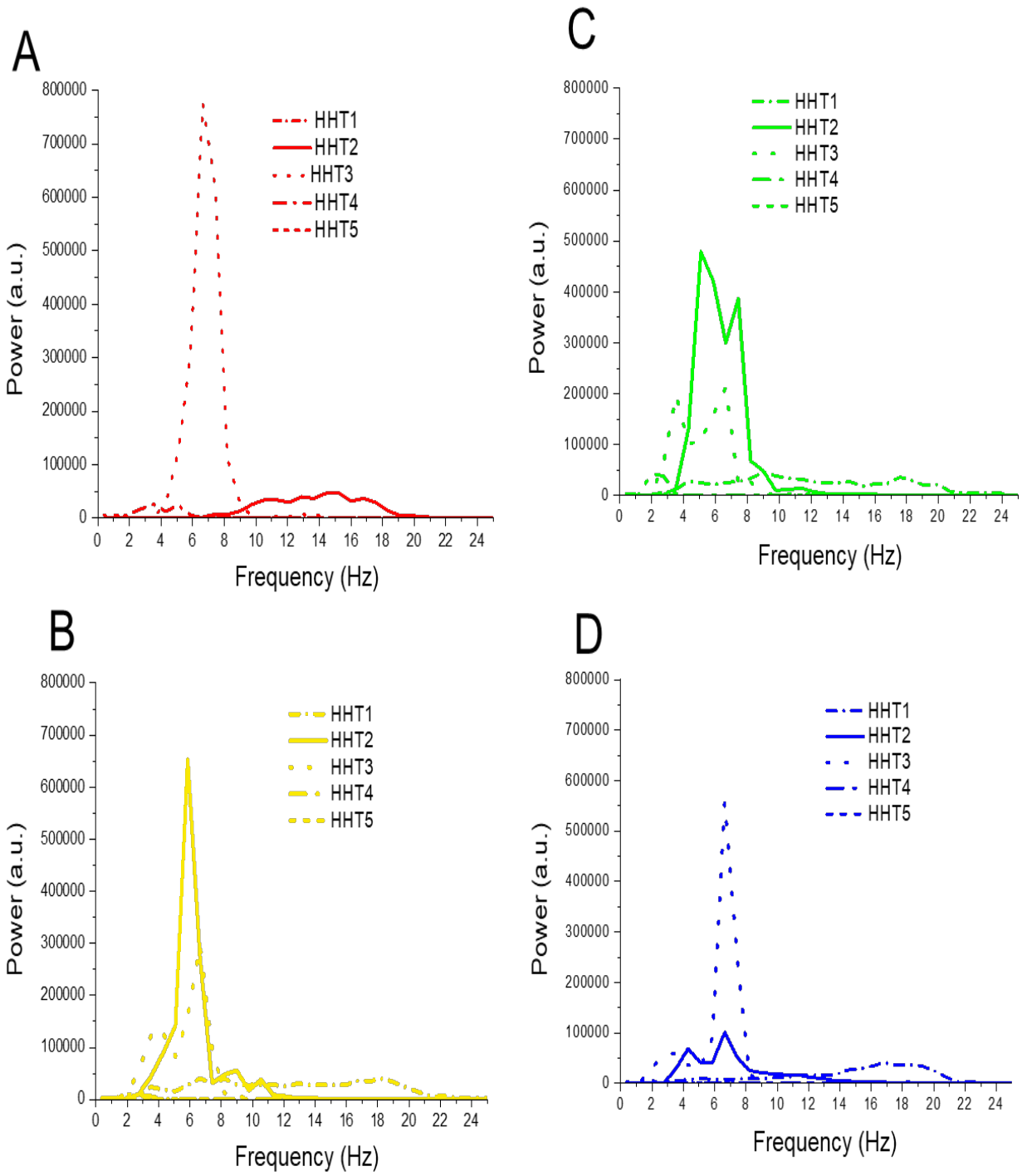
A
B
C
D
HHT1
HHT2
HHT3
HHT4
HHT5
Power (a.u.)
Frequency (Hz)
0
100000
200000
300000
400000
500000
600000
700000
800000
0 2 4 6 8 10 12 14 16 18 20 22 24

Fig.S2

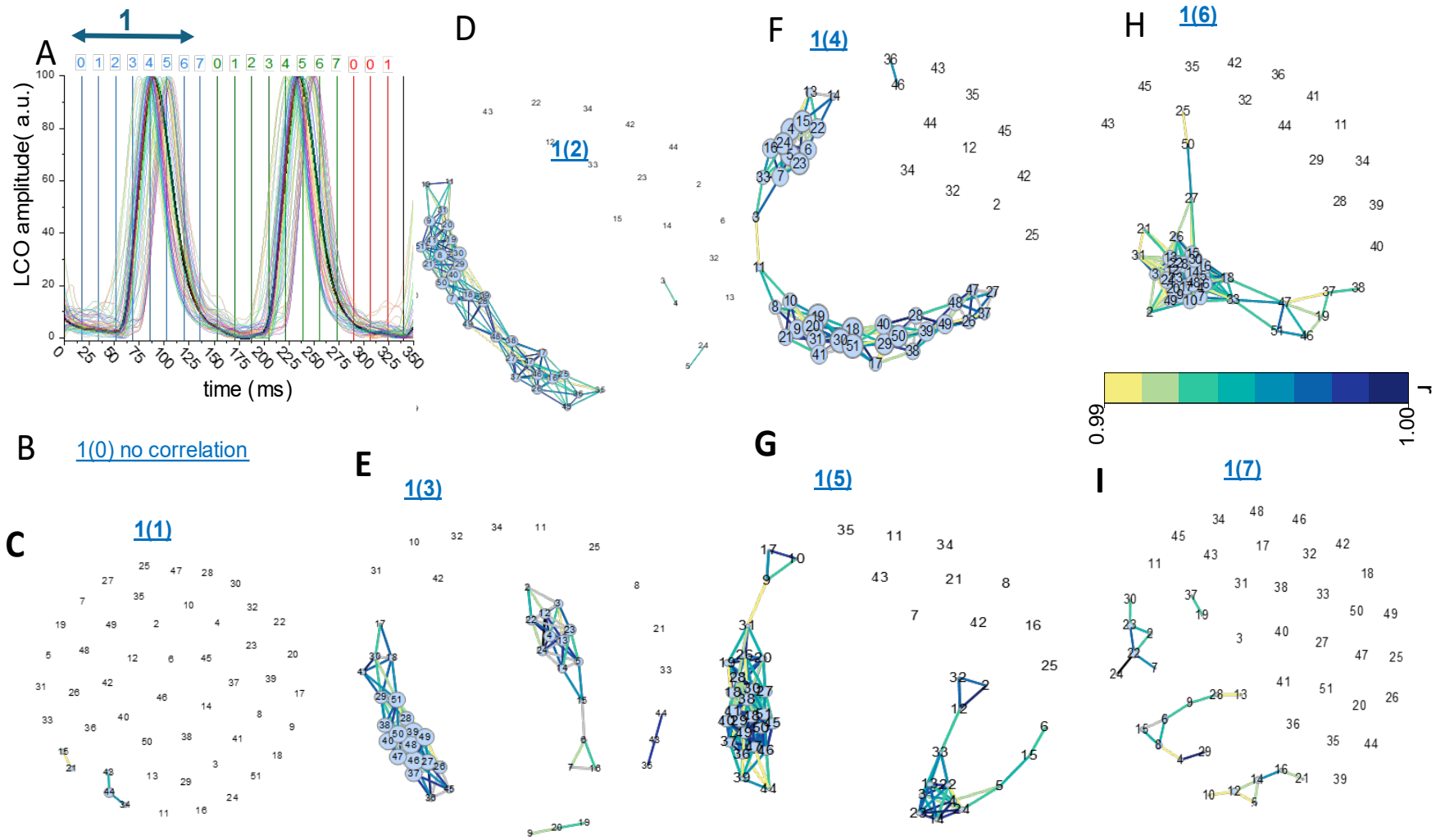
A
1
0 1 2 3 4 5 6 7 0 1 2 3 4 5 6 7 0 0 1
LCO amplitude(a.u.)
time (ms)
B
1(0) no correlation
C
1(1)
D
1(2)
E
1(3)
F
1(4)
G
1(5)
H
1(6)
I
1(7)
0.99
1.00
r

Fig.S3.

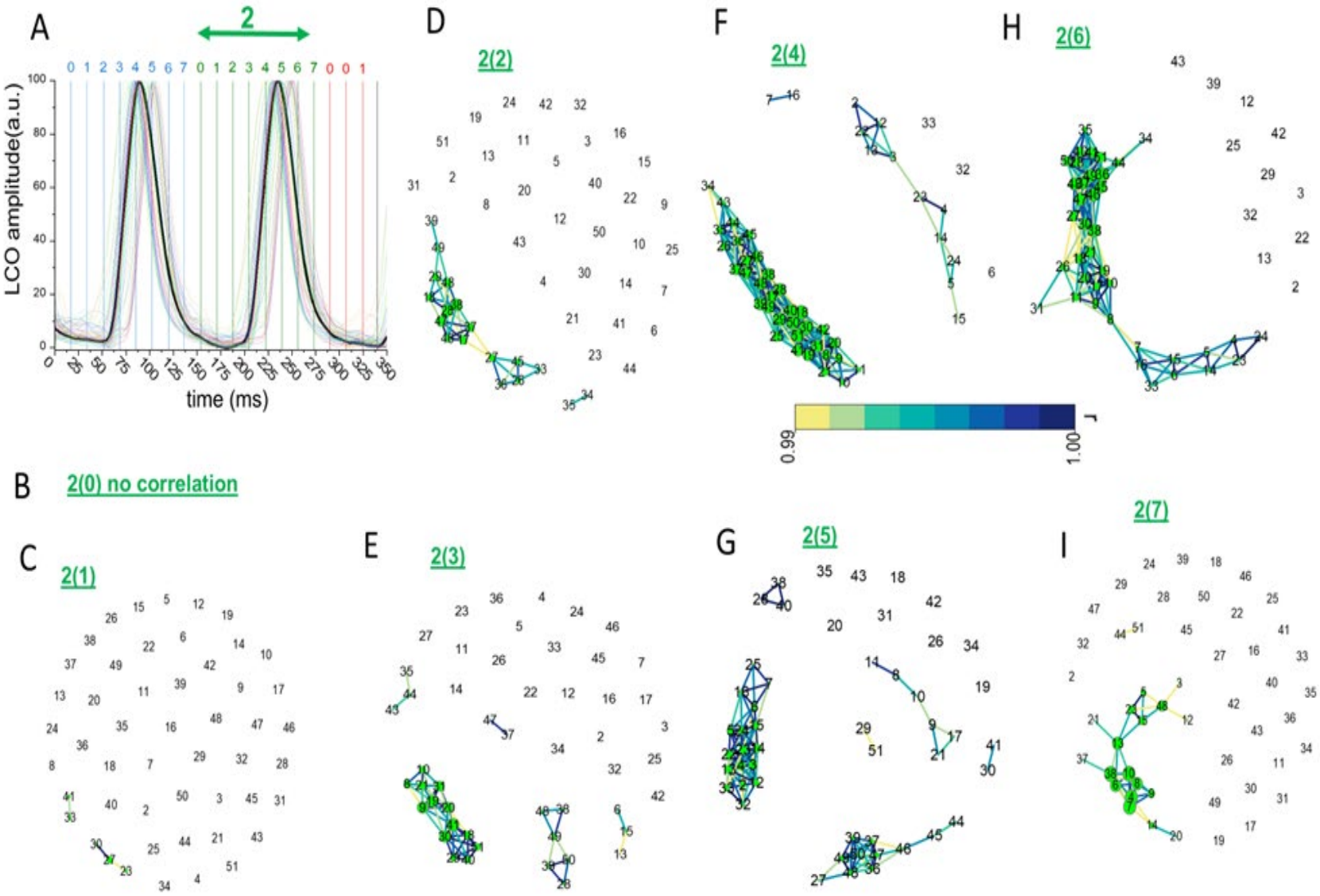
A
2
0 1 2 3 4 5 6 7 0 1 2 3 4 5 6 7 0 0 1
LCO amplitude(a.u.)
time (ms)
B
2(0) no correlation
C
2(1)
D
2(2)
E
2(3)
F
2(4)
G
2(5)
H
2(6)
I
2(7)
0.99
1.00
r

Fig.S4.

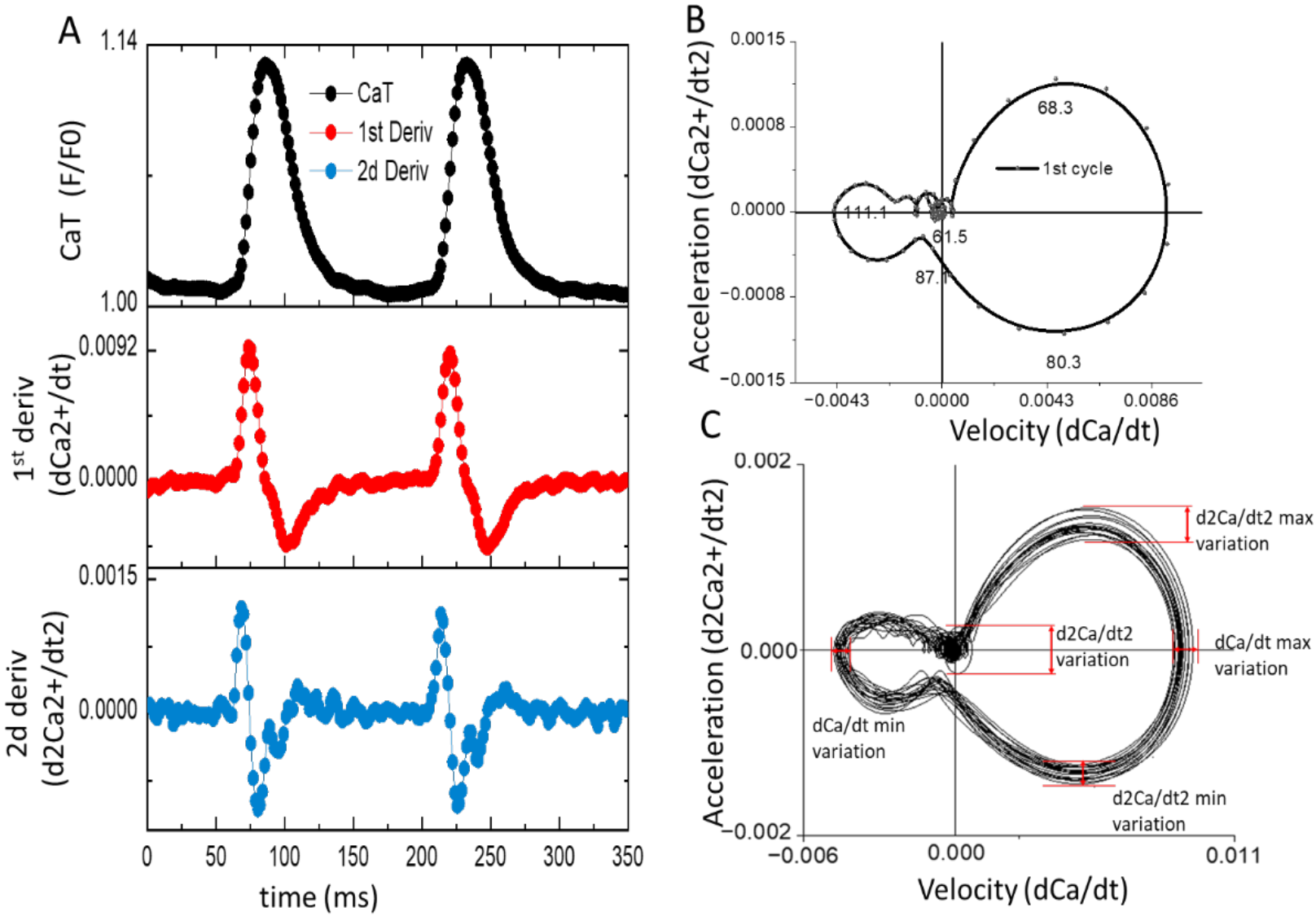
A
1.14
1.00
CaT (F/F0)
CaT
1st Deriv
2d Deriv
0.0092
0.0000
1st deriv (dCa2+/dt)
0.0015
0.0000
2d deriv (d2Ca2+/dt2)
0
50
100
150
200
250
300
350
time (ms)
B
0.0015
0.0008
0.0000
−0.0008
−0.0015
Acceleration (dCa2+/dt2)
68.3
1st cycle
111.1
61.5
87.1
80.3
−0.0043
0.0000
0.0043
0.0086
Velocity (dCa/dt)
C
0.002
0.000
−0.002
Acceleration (d2Ca2+/dt2)
d2Ca/dt2 max variation
d2Ca/dt2 variation
dCa/dt max variation
dCa/dt min variation
d2Ca/dt2 min variation
−0.006
0.000
0.011
Velocity (dCa/dt)

Fig. S5

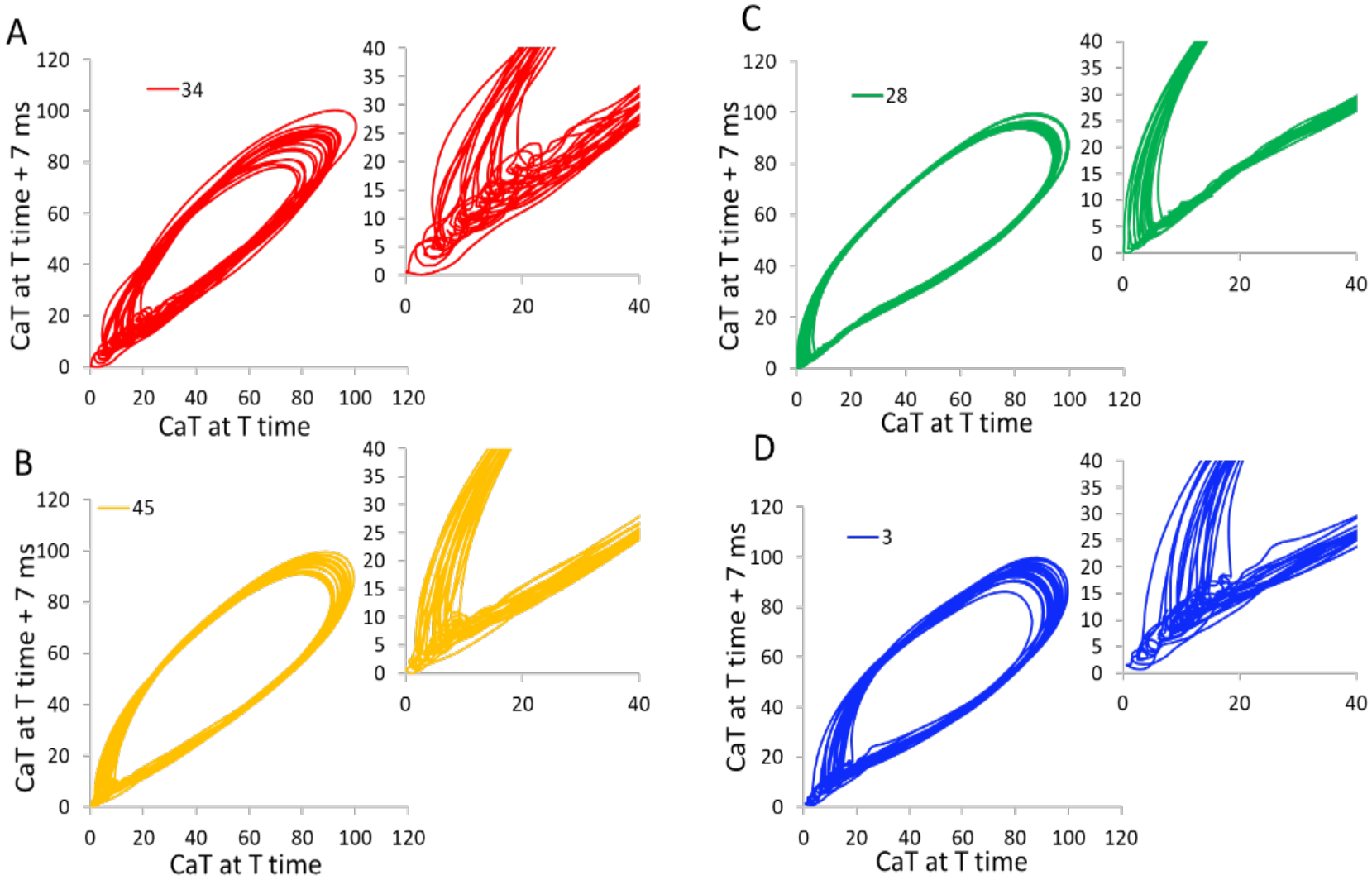
A
34
CaT at T time + 7 ms
CaT at T time
B
45
CaT at T time + 7 ms
CaT at T time
C
28
CaT at T time + 7 ms
CaT at T time
D
3
CaT at T time + 7 ms
CaT at T time

Fig. S6

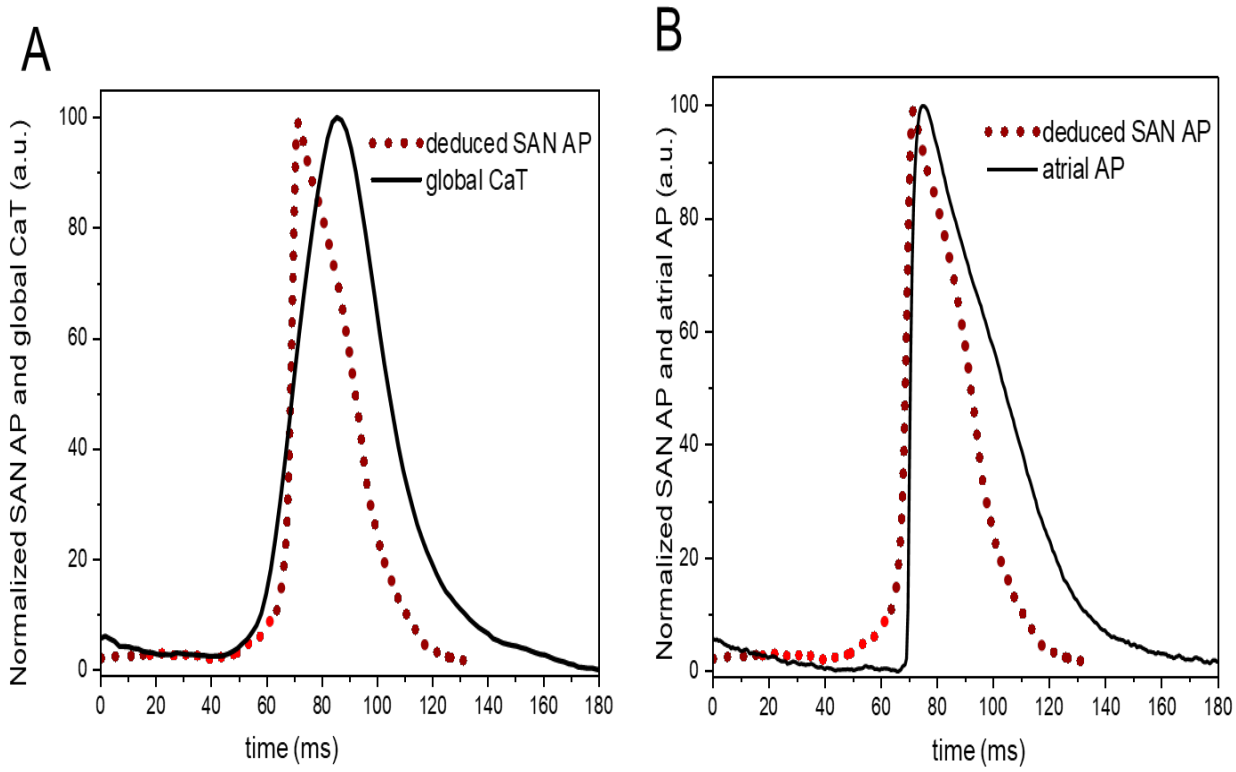

Fig. S7.

References

1. Bychkov R, Juhaszova M, Tsutsui K, Coletta C, Stern MD, Maltsev VA, et al. Synchronized Cardiac Impulses Emerge From Heterogeneous Local Calcium Signals Within and Among Cells of Pacemaker Tissue. Jacc-Clin Electrophy. 2020;6(8):907-31.
2. Bergé P, 1934- , Pomeau Y, Vidal CC. Order within chaos : towards a deterministic approach to turbulence: New York : Wiley ; Paris : Herman; 1986.
3. Packard NH, Crutchfield JP, Farmer JD, Shaw RS. Geometry from a Time-Series. Phys Rev Lett. 1980;45(9):712-6.
4. Takens F. Detecting Strange Attractors in Turbulence.: Springer, Berlin, Heidelberg.; 1981.
5. Cao LY. Practical method for determining the minimum embedding dimension of a scalar time series. Physica D. 1997;110(1-2):43-50.
6. Abreu T, Silva PA, Sancho F, Temperville A. Analytical approximate wave form for asymmetric waves. Coast Eng. 2010;57(7):656-67.
7. Huang NE. Introduction to the Hilbert-Huang Transform and Its Related Mathematical Problems. Interd Math Sci. 2005;5:1-26.
8. Mateo C, Talavera JA. Short-time Fourier transform with the window size fixed in the frequency domain. Digital Signal Processing. 2018;77:13-21.